

# Plasma processes for novel detector fabrication

William Reilly Cunningham



UNIVERSITY  
*of*  
GLASGOW

October 2003

A Thesis submitted for the degree of Doctor of Philosophy of the University  
of Glasgow

©William Reilly Cunningham 2003

## **Abstract**

Plasmas have a wide range of uses from fluorescent light tubes to high technology semiconductor fabrication. In this work I will attempt to discuss a number of plasma processes which have been developed for standard semiconductor fabrication over recent years and apply them to producing detectors in a novel fashion. This will encompass the alteration of older existing processes used on silicon (Si) for use with a new detector material, silicon carbide (SiC). The other application which will be investigated is the use of processes to fabricate devices in indium tin oxide (ITO) which is a transparent conductive semiconductor used in making screens for laptop computers for a new application. ITO will be used to produce a range of microelectrode arrays which can be used in neurophysiology studies using retinal tissue.

## Acknowledgements

This is the point where people normally thank those that they feel assisted them in any way during the course of their research and far be it from me to balk at tradition. I would like to thank my supervisor Mahfuzur Rahman for frequent and regular meetings and assistance, also for being able to decipher my sometimes rambling style of writing. I would like to acknowledge the help of all the staff in the USSL lab, the Dry etch lab, and the Level 6 cleanroom in the Electrical and Electronic Engineering Department at Glasgow for assistance, help, and the use of all the facilities without which this project could never have happened. The technicians in the Detector lab past and present specifically Meg Horn and John Melone for cutting/ polishing and bonding work respectively, and Drew Meikle, Steven Bryce and Pamela Thornton before them, again without them this work could never have taken place. I would like to thank my industrial supervisor Mike Cooke at Oxford Plasma Technology and all of the Development engineers, Ross, Andy, and Chris, for an enjoyable time working there and a lot of assistance with the equipment.

More thanks for much help, and understanding exactly what I wanted to know/do/say goes to Keith, Val, Richy, and Ken. They helped me understand some of the more obscure and not so obscure results that appeared from my work. Keith in particular has been the driving force behind progress in the retinal project. Other people who need thanked are John M, Meg, and Fred in the Detector lab, and John K for being bloody clever all over the place. Tatjana, Dave, Andy, Franky, Chris A, and Vic for not complaining too much about my whingeing on about how hard this writing business is

and Julien for for not rubbing it in too much for finishing months before me. Additional thanks to all of the above, plus any others who I forgot to mention you know who you are, for much non-physics related time spent in the pub discussing much more pleasant things.

That brings me to Henrik Larsson, Martin O'Neill, and the rest of the players at Celtic Football Club for giving us so many pleasant alternative things to discuss, although their UEFA cup run nearly killed me. Finally thanks to Lisa for helping me stay sane (?), attempting to look interested when I told her what I do, and for not being too bitter about the fact that her thesis has to be at least a hundred pages longer than mine, it's her own fault for being a biologist. Also cheers to my parents for not being embarrassed to tell people their son finished school at 27.

## Declaration

I declare that except where explicit reference is made to the work of others, this dissertation is the result of my own work. This work has not been submitted for any other degree at the University of Glasgow or any other institution.

William Reilly Cunningham

# Contents

<b>1</b>	<b>Introduction</b>	<b>1</b>
1.1	Industrial plasma processes . . . . .	1
1.2	Novel material applications . . . . .	2
1.3	Novel device applications . . . . .	4
<b>2</b>	<b>Sample fabrication techniques</b>	<b>7</b>
2.1	Introduction . . . . .	7
2.2	Lithography . . . . .	7
2.2.1	Photolithography . . . . .	8
2.2.2	Electron-beam lithography . . . . .	13
2.2.3	Resist types . . . . .	19
2.3	Lift off and contact definition . . . . .	24
2.3.1	The lift off process: Photolithography . . . . .	24
2.3.2	The lift off process: Electron beam lithography . . . . .	25
2.3.3	Advantages and disadvantages of lift off . . . . .	26
<b>3</b>	<b>Introduction to plasma theory and reactor types</b>	<b>28</b>
3.1	Introduction . . . . .	28
3.2	Basic plasma theory . . . . .	29
3.3	DC glow discharge . . . . .	32

3.3.1	Regions of a normal glow discharge . . . . .	33
3.3.2	Theory of glow discharges . . . . .	36
3.3.3	Capacitively coupled RF glow discharge . . . . .	40
3.3.4	Plasma enhanced chemical vapour deposition (PECVD) of $\text{Si}_3\text{N}_4$ . . . . .	44
3.3.5	Reactive ion etching (RIE) . . . . .	46
3.4	Inductively coupled RF plasma generation . . . . .	47
3.4.1	Inductively coupled plasma reactors . . . . .	50
<b>4</b>	<b>Development of plasma processes</b>	<b>53</b>
4.1	Introduction . . . . .	53
4.2	Plasma etching of SiC . . . . .	53
4.2.1	Properties of SiC . . . . .	53
4.2.2	Etch parameters . . . . .	54
4.2.3	Metal-semiconductor contacts . . . . .	58
4.2.4	SiC I-V characterisation . . . . .	66
4.2.5	Etch damage comparison . . . . .	70
4.3	Plasma etching of ITO . . . . .	71
4.3.1	Introduction . . . . .	71
4.3.2	Etch parameters for ITO . . . . .	72
4.3.3	Masking properties . . . . .	72
4.3.4	I-V characterisation of etched ITO . . . . .	74
4.3.5	Etching of ITO using resist/Ti mask . . . . .	76
4.4	Plasma deposition of $\text{Si}_3\text{N}_4$ . . . . .	78
4.4.1	Etching deposited $\text{Si}_3\text{N}_4$ layers . . . . .	78
4.4.2	Reduction of pinhole density and adhesion promotion . . . . .	79

4.5	Plasma etching of Ti . . . . .	81
<b>5</b>	<b>SiC radiation detectors</b>	<b>83</b>
5.1	Introduction . . . . .	83
5.2	Detector fabrication . . . . .	84
5.2.1	Diode design . . . . .	84
5.2.2	Diode fabrication . . . . .	85
5.3	Detector theory . . . . .	86
5.3.1	Ionising radiation interactions . . . . .	86
5.3.2	Charge collection . . . . .	94
5.3.3	Energy calibration . . . . .	96
5.3.4	CCE measurements . . . . .	97
5.4	Results for SiC detectors . . . . .	98
5.4.1	Un-irradiated diodes . . . . .	98
5.4.2	Trap measurements and spectra . . . . .	103
5.4.3	Irradiated SiC diodes . . . . .	109
5.4.4	Summary of SiC data and future work . . . . .	114
<b>6</b>	<b>Retinal readout system</b>	<b>116</b>
6.1	Introduction . . . . .	116
6.2	Retinal physiology . . . . .	118
6.2.1	Layers of the retina . . . . .	118
6.2.2	Functionality of retina . . . . .	121
6.3	Fabrication of retinal readout arrays . . . . .	123
6.3.1	Development of processes for fabrication: 61 electrode arrays . . . . .	124

6.3.2	Development of processes for fabrication: 519 electrode arrays . . . . .	126
6.3.3	Metallisation of electrodes and contacts . . . . .	131
6.4	Details of retinal readout project . . . . .	133
6.4.1	Experimental setup . . . . .	134
6.4.2	Signal types . . . . .	136
6.4.3	Experimental results . . . . .	138
6.5	Future work and further developments . . . . .	140
<b>7</b>	<b>Conclusions</b>	<b>142</b>

# List of Figures

1.1	Can you guess what it is? . . . . .	5
2.1	The two most common types of photolithography processes are shown here: <i>left</i> contact printing and <i>right</i> projection printing [16]. . . . .	8
2.2	The photolithography process. Exposure of the resist and development of the pattern. . . . .	11
2.3	The feature spreading caused by light diffraction as it passes through the mask and resist [16]. . . . .	12
2.4	This is a schematic for an e-beam lithography system showing the major components used for controlling the beam [14]. . . .	14
2.5	The interface window for CATS, one of the e-beam conversion programs. . . . .	15
2.6	The interface window for BELLE, one of the e-beam conversion programs. . . . .	16
2.7	Structure of DQ (diaz-quinone) [15]. . . . .	19
2.8	The chemical changes in DQ after exposure to UV radiation [15]. . . . .	21
2.9	The breakdown of the alkaline resistant PAC during exposure to UV light [16]. . . . .	22

2.10	The process of lift off definition of metals [14]. . . . .	25
2.11	The effect of different solvent soaks on the resist profile for lift off processing. <i>a</i> no soak, <i>b</i> chlorobenzene soak, and <i>c</i> fluorobenzene soak [15]. . . . .	26
2.12	Bi-layer of e-beam resist used to create overhanging profile for lift off. . . . .	27
3.1	The different regimes through which a DC discharge progresses as the ion current increases [22]. . . . .	30
3.2	Structure of DC glow discharge and variations of light intensity, plasma potential, electric field, and net charge density along the discharge tube.[22] . . . . .	33
3.3	A schematic of a parallel plate reactor showing variables required to calculate the power input into a normal unmagnetised DC glow discharge [22]. . . . .	38
3.4	A schematic of a parallel plate reactor showing variables required to calculate the power input into a normal unmagnetised RF glow discharge [22]. . . . .	41
3.5	A schematic of a parallel plate reactor with a single driven cathode and earthed anode showing the potential distribution typical in this type of reactor [22]. . . . .	44
3.6	A schematic of inductively coupled RF plasma generation. [22]	48
3.7	The variation in skin depth with different values of the ratio $\nu_c/\omega$ for a range of electron number densities [22]. . . . .	50
3.8	Schematic of industrial ICP reactor showing the two chambers used to separate ion production from the sample. . . . .	51

4.1	Plotted are the etch rates against applied RF bias power for a constant ICP power of 1250 W (left hand axis). The right hand vertical axis shows the DC self bias at the different values of the RF bias power. Etch selectivity for NiCr: SiC was greater than 10 : 1 even for the highest etch rate, while selectivity of photoresist : SiC was approx. 1 : 1. . . . .	56
4.2	Shown are the etch rates against applied ICP power for a constant RF bias power of 200W. The right hand vertical axis shows the DC self bias at the different ICP powers. Etch selectivity for the 70 nm NiCr mask was $\sim 20$ : 1 even for the highest etch rate. . . . .	57
4.3	Shown is the etch rate obtained for different fractions of O <sub>2</sub> added to the SF <sub>6</sub> . . . . .	58
4.4	The development of the band structure at a metal-semiconductor interface [35]. . . . .	59
4.5	Energy band diagrams for n- and p-type material for various bias conditions [14]. . . . .	61
4.6	Energy band diagram for a metal-vacuum interface, the lowering is due to a combination of the electric field and the image force [35]. . . . .	63
4.7	Energy band diagram for a metal-vacuum interface, showing the Schottky effect for n-type semiconductors. $q\phi_{BO}$ is the intrinsic barrier height, $q\phi_{Bn}$ is at thermal equilibrium [35]. . .	64
4.8	Energy band diagram for a metal/vacuum interface, showing the Schottky effect for n-type semiconductors. $q\phi_{BO}$ is the intrinsic barrier height, $q\phi_{Bn}$ is at thermal equilibrium [35]. . .	65

4.9	<i>left</i> Leakage current and <i>right</i> Schottky barrier height as a function of incident ion energy in RIE discharge. . . . .	67
4.10	<i>left</i> Leakage current and <i>right</i> Schottky barrier height as a function of O <sub>2</sub> content in ICP plasma. . . . .	69
4.11	Wires similar to those etched into the ITO layer, 600 $\mu$ m by several mm. . . . .	75
4.12	I-V characterisation for CH <sub>4</sub> /H <sub>2</sub> etched ITO plates. . . . .	76
4.13	I-V characterisation for ITO plates after SF <sub>6</sub> cleaning of UVIII/Ti mask structure. . . . .	77
5.1	Mask design for SiC test samples. . . . .	85
5.2	The energy deposition Bragg curve for a 5.48 MeV $\alpha$ particle in SiC. . . . .	89
5.3	Compton scattering for photon incident on an electron [46]. . . . .	91
5.4	Change in importance of the different photon interactions with energy [46]. . . . .	93
5.5	Field distribution through a semiconductor detector for various bias voltages. $V_d$ is the depletion voltage of the device [46]. . . . .	95
5.6	Reverse current plots for 500um pad from 0- -100V for different humidity levels. . . . .	99
5.7	Current density against voltage for a Schottky barrier diode fabricated on S.I. 4H-SiC. . . . .	100
5.8	Capacitance against voltage for an unirradiated SiC detector. . . . .	101
5.9	Am <sup>241</sup> spectra taken at increasing bias voltages. Note the low energy tail on the higher bias voltage spectra. . . . .	102

5.10	Peak positions as a function of the increasing bias voltage. . .	103
5.11	Discharge currents measured from diode after biasing for varying lengths of time plotted against $\log(t)$ from the point of bias turn off. . . . .	105
5.12	Arrhenius plot of TSC measurements taken of SiC diode. The behaviour observed is complex suggesting a number of different defects. . . . .	107
5.13	<i>top</i> The effect of varying the V density on the electron pulse height. <i>bottom</i> The effect of varying the V density on the maximum possible CCE. . . . .	109
5.14	Comparison of post irradiation currents with pre-irradiation current. . . . .	111
5.15	$\text{Am}^{241}$ spectra taken at increasing bias voltages for irradiated diodes. <i>top</i> $10^{12} \text{ } \pi\text{cm}^{-2}$ and <i>bottom</i> $10^{13} \text{ } \pi\text{cm}^{-2}$ . . . . .	113
6.1	Vertical slice through human retina taken near the fovea [85]. .	119
6.2	Schematic of retinal tissue showing all of the major cell types. <i>R</i> are receptors, <i>H</i> horizontal cell, <i>B</i> bipolar cell, <i>A</i> amacrine cell, <i>G</i> ganglion cell, <i>I</i> interplexiform cell, <i>M</i> Müller (glial) cell [85]. . . . .	120
6.3	Variations in response from illuminated and nearby photoreceptors [85]. . . . .	122
6.4	<i>left</i> Design for 61-electrode array. <i>right</i> Close up of central section showing the wire ends, where the electrodes were formed, with $60 \text{ } \mu\text{m}$ spacing. . . . .	124

6.5	Sections of completed 61 electrode array. <i>left</i> Middle section of wires showing large wires with small spaces between. <i>right</i> shows an etched version of Fig. 6.4 <i>right</i> . . . . .	126
6.6	Design for 519 electrode array. Close up of central section on right shows square electrodes on wire ends with 60 $\mu\text{m}$ spacing.	127
6.7	Modified design for 519 electrode array for combination photo- and e-beam lithography process with blank central section on the main wires mask. . . . .	128
6.8	519 array written by electron-beam. The grid like lines visible are where the pattern has been improperly stitched together. This is caused by the height recognition laser interferometer being unable to find the ITO surface. . . . .	129
6.9	Central area of 519 electrode array with the etched wires clearly visible. Also shown is a close up to the densely packed centre of the array. . . . .	130
6.10	Wires which have been overexposed due to the proximity effect. <i>left</i> A broken wire. <i>right</i> A wire which has been drastically thinned. . . . .	131
6.11	Platinised electrodes from an array showing the granular structure of the electrode surface. . . . .	132
6.12	Process for production of 519-electrode arrays. . . . .	134
6.13	Schematics of experimental setup showing the setup for retinal neurophysiology experiments using electrode arrays [87] . . . .	135
6.14	Schematics for on chip electronics connected to each electrode in the array [12]. . . . .	136
6.15	Spikes recorded with a 61 electrode array fabricated in Glasgow[88].	138

6.16 Short test measurements for completed 519 electrode array.  
Shorted channels are numbered. . . . . 140

# List of Tables

1.1	Some material and electrical properties of 4-H SiC compared to Si and GaAs . . . . .	3
2.1	Process steps for photolithography . . . . .	10
2.2	Process steps for e-beam lithography for standard PMMA resist	18
2.3	Process steps for e-beam lithography using UVIII CAR resist.	24
3.1	The different current-voltage regimes of a DC electrical discharge. . . . .	29
3.2	Parameters for deposition of hydrogenated amorphous a-SiN <sub>x</sub> : H . . . . .	45
4.1	Some important material and electrical properties of SiC . . . . .	54
4.2	Constant parameters for the series of etching tests . . . . .	55
4.3	Parameters for SF <sub>6</sub> RIE surface treatment of SiC . . . . .	67
4.4	Parameters for SF <sub>6</sub> /O <sub>2</sub> ICP etching of SiC . . . . .	69
4.5	Etch parameters for CH <sub>4</sub> /H <sub>2</sub> etching of ITO . . . . .	72
4.6	Solvent cleaning processes tried for various photoresist post bake times for etching of ITO using CH <sub>4</sub> /H <sub>2</sub> . . . . .	74
4.7	Etch parameters for SF <sub>6</sub> plasma clean of ITO substrate. . . . .	77
4.8	Process parameters for SF <sub>6</sub> etching of Si <sub>3</sub> N <sub>4</sub> . . . . .	78

4.9	Process parameters for oxygen plasma surface treatment . . .	80
4.10	Table shows change in density of defects in $\text{Si}_3\text{N}_4$ layer for different ash times. . . . .	80
4.11	Etch parameters for $\text{SiCl}_4$ etching of Ti . . . . .	81
5.1	Breakdown of four main categories of ionising radiation . . . .	87
5.2	Temperature, activation energy and possible attribution of peaks in TSC spectra. . . . .	107
5.3	Variation in measured barrier height, resistivity, and carrier concentration with increasing fluence. . . . .	111

# Chapter 1

## Introduction

In this thesis I will discuss the techniques and processes used to fabricate novel semiconductor detectors with novel applications. The use of semiconductors is changing, with new materials being tested for use over the more traditional silicon. Also, the areas within which semiconductor technology is being applied is expanding. To facilitate this, change in materials and use of new processes are necessary that take into account the changes in role and material. The main areas to be investigated are the role of plasma processes for fabricating new devices, and for fabricating so called traditional devices with new materials.

### 1.1 Industrial plasma processes

Plasma is the fourth state of matter. In this work the word plasma is used to mean a relatively cool ionised gas rather than the more traditional image of a plasma as a roiling nuclear fireball like the sun. Indeed, the most common use of plasma is in lighting tubes, as they give off relatively intense light without the heat losses associated with traditional tungsten filament lamps. This enables great financial savings. However, plasmas have a number of

different applications within industry. One of the more common of these is in processing semiconductors.

The nature of an ionised gas means that it can interact with its surroundings in a number of ways depending on the chemistry of the gas. By choosing an appropriate gas it is possible to modify the surface properties of a material. For semiconductor processing it is possible to transfer patterns to the surface by using the plasma to remove material from the bulk of the sample; this process is known as plasma or dry etching. Alternatively it is possible to use a plasma to deposit material onto a surface. This can be used to deposit dielectric layers like silicon dioxide ( $\text{SiO}_2$ ) or silicon nitride ( $\text{Si}_3\text{N}_4$ ) for semiconductor processing and is known as plasma deposition. The uses of these two types of processes in semiconductor fabrication has increased dramatically in recent years as the pace of development of new technologies has increased. In this work a brief description of the governing equations for plasma generation will be given along with details of some of the more common plasma tools available and how they can be applied for use in two novel applications.

## 1.2 Novel material applications

Silicon carbide ( $\text{SiC}$ ) is a compound semiconductor which is formed at very high temperature and pressures. Some of its more important properties are given in Table 1.1. As well as these,  $\text{SiC}$  is also very chemically inert. Many applications are possible for the material especially for those areas where Si is impractical or simply unusable, such as at high temperature, high power operation and/or high radiation environments. Possible applications include improved high-voltage switching [1]-[4]. A future possibility for  $\text{SiC}$  in this

Table 1.1: Some material and electrical properties of 4-H SiC compared to Si and GaAs

Material	SiC	Si	GaAs
Crystal Structure	Wurtzitic	Diamond	Zincblende
Lattice constant (Å)	a : 3.08 c: 9.92	5.43	3.19 5.19
Density ( $\text{gcm}^{-3}$ )	3.2	2.328	5.32
Mobilities ( $\text{cm}^2\text{V}^{-1}\text{s}^{-1}$ ) $\mu_n$	900	1500	8500
$\mu_p$	20	450	400
Band gap ( $\phi_b$ (eV))	3.3	1.12	1.4
Electron/hole pair production energy (eV)	8.4	3.55	4.27
Thermal conductivity (W/cmK)	4.9	1.5	0.46

area is to be able to operate at voltage levels that would prove fatal to similar devices in Si. Changing to SiC in this area could give increases in efficiency and consequently great monetary savings in public energy distribution and electric motors. Another possible application for SiC switching devices lies in high power microwave electronics for communications [5]-[7]. In particular manufacture of FETs mean that SiC devices could operate with very much higher temperatures and voltages than Si, but have only a fraction of the die size [8].

Applications to high radiation environments could be envisaged in space or inside nuclear reactors. The flux of high energy particles and extremely high electromagnetic radiation levels involved leads to the destruction of semiconductor devices. By switching to SiC with its higher band gap and bond strength the rate of induced damage from radiation is expected to be significantly lower. One possible area where reduced radiation damage rates would introduce great cost savings is in the inner semiconductor tracker re-

gions of large high energy particle detectors like that at the Large Hadron Collider (LHC) being built at CERN. This will have protons colliding with a centre of mass energy of 14 TeV with an expected luminosity of  $1 \times 10^{34} \text{ cm}^{-2}\text{s}^{-1}$ , which will rise to  $1 \times 10^{35} \text{ cm}^{-2}\text{s}^{-1}$  after the proposed upgrade in 2012. The saving to be had from producing detectors from a material which will last for a significantly longer lifetime in the detector while giving reasonable results would be immense. To this end much work has been carried out using SiC as a semiconductor radiation detector.

Since the 1970's semiconductor devices fabricated on Si substrates have been used as radiation detectors [9]. But it was in 1980 that the planar geometry that now dominates the field came into play [10]. However, SiC is a relatively new material for this application. This means that problems still exist with the growth techniques and new fabrication processes need to be developed. Within this work I will discuss the performance of planar radiation detectors fabricated on SiC substrates. Details will be given of the plasma processes used to produce the devices which were then tested for detection of radiation, specifically  $\text{Am}^{241}$   $\alpha$  particles. Good performance of diodes irradiated to high fluences,  $10^{14}$  pions/cm<sup>2</sup>, with high energies, 300 MeV, has also been observed.

### 1.3 Novel device applications

As mentioned above the use of planar technology for making semiconductor detectors is well established. However, in recent years many of the fabrication techniques that have been developed for use in electronics are being used for very different applications. One of the largest collaborative multi-disciplinary areas is in bio-physics and bio-engineering. This uses technology like that

outlined already but for exploitation in a new range of life sciences applications. The applications range from high definition solid state detectors to replace photographic film in X-rays, to producing new types of detectors for specific biological applications. The Retinal Readout Project is one such collaborative effort. This exploits technology and expertise in semiconductor detectors and data acquisition in experiments at CERN and uses them to make detectors to study the retina.



Figure 1.1: Can you guess what it is?

Vision is one of the most important of the senses for all creatures that have it. The human eye is a remarkable piece of detector engineering. It allows vision over a vast range of light intensities from bright midday sunshine to dim candle light. However, it is not the simple act of producing an electrical impulse from a number of cells in the retina which is the most remarkable thing about human vision. The retina itself has approximately 100 million photoreceptors which are connected in a complex way to 1 million neurons for transmission to the visual cortex of the brain. It is only here that the truly remarkable aspects of the visual system comes into play. The way that

the visual cortex interprets, stores, and then accesses information is such that it is possible to recognise a familiar face even after years of separation and physical change. This process is so hideously complicated that millions of pounds have been spent to produce systems which are as complex and unreliable as they are expensive. Fig. 1.1 gives an example of the type of processing that the human visual system is capable of. There is very little information in the picture but many people can instinctively guess what it is (if you can't guess the answer is here <sup>1</sup>). Obviously there is something very complicated going on here.

For the Retinal Readout Project the University of Glasgow is collaborating with the Salk Institute for Biological Studies, San Diego California, and the Santa Cruz Institute for Particle Physics (SCIPP) at the University of California Santa Cruz. The project aims to allow the simultaneous detection of signals from hundreds of output cells in live retinal tissue as a visual image is focused on the input cells. The signals detected can be correlated with the input images and much information about the way in which groups of cells interact can be gleaned. This work covers details of the development of plasma processes, etching and deposition, to produce a range of high density electrode arrays for use in this effort. Two designs are covered here, the first is a 61 electrode array which has been commonly used for many years. The second design is a high density array with 519 electrodes which is relatively new. Experimental data taken using 61 electrode arrays are shown here along with initial test data from a 519 electrode array.

---

<sup>1</sup>It's an elephant

# Chapter 2

## Sample fabrication techniques

### 2.1 Introduction

This section will cover the techniques used to produce samples for testing, including photolithography, electron-beam lithography, and metal lift off for definition of contacts and alignment marks. The most commonly used techniques were photolithography and lift-off. The information here is referenced mostly from two books, ‘Semiconductor Devices: Physics and Technology’ by S.M. Sze [14] and ‘The science and technology of microelectronic fabrication’ by S.A. Campbell [15]. Additional illustrational figures were taken from course notes by Prof C. D. W. Wilkinson [16].

### 2.2 Lithography

Lithography is defined by the Cambridge dictionary as ‘producing a picture printed using a stone or metal block on which an image has been drawn with a thick oily substance that attracts ink’. In the present work the word is used to define a process for transferring a pattern to a piece of semiconductor via an intermediate compound called a resist. Resist is a polymer compound which is sensitive to patterning using different radiation sources. The different

techniques used and the differences between different types of resist will be discussed in detail below.

### 2.2.1 Photolithography

Photolithography was chosen as the main process step due to the simplicity and reproducibility of the techniques employed. Photolithography uses UV (ultra-violet) light as the radiation source to transfer the pattern to an intermediate compound called a photo-resist or simply a resist. Two processes are possible, contact printing and projection printing, as illustrated in Fig. 2.1

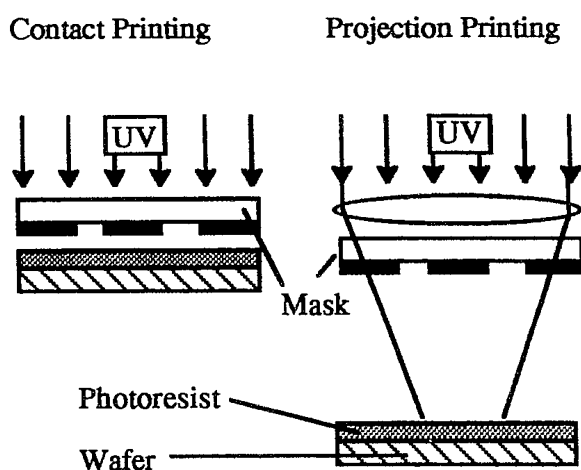


Figure 2.1: The two most common types of photolithography processes are shown here: *left* contact printing and *right* projection printing [16].

Fig. 2.1 shows the main difference between contact and projection printing. The difference lies in the position of the mask plate. In contact printing the mask is in contact with the sample and for projection printing a lens system is used to focus the UV light through the mask onto the substrate. They

both have certain advantages and disadvantages. Contact printing has good resolution without the need for complicated optics or scaling of the mask features. The positioning in projection printing means that the features are not directly translated but undergo a change in scale. However projection printing means that the mask gets less contamination and produces more consistent resolution and alignment as the projection system does not have to take into account the effect of uneven layers of resist.

As mentioned previously the optics for a projection printing system are more complex than those for a contact printer and the mask needs to be scaled very precisely to take into account the effects of projection. This can increase the complexity of the design process. Projection printing is used mainly in industry where the setup is needed to produce thousands of wafers, so contamination handling is important. The photolithographic processing discussed in this thesis was carried out using a Karl-Suss contact printing mask aligner. Registration size, which governs how accurately two subsequent layers of lithography can be aligned, is  $\sim 5 \mu\text{m}$  with a resolution of  $\sim 1 \mu\text{m}$ .

The incident UV radiation causes the resist compound to break down so that it can dissolve in a solution known as developer. The unexposed resist is resistant to the developer solution. This leads to the removal of the exposed areas. Thus the pattern from the mask is transferred to the resist layer. The various steps to producing a pattern are given in Table 2.1 for a standard photoresist like that used here, Shipley 1818 (S1818). This is the standard process for producing a pattern in S1818 photoresist. The post treatment step is added if required to reduce the sensitivity of the resist to damage depending on which type of process it is going to be used for.

Table 2.1: Process steps for photolithography

Step	Parameters
Surface clean	Sequential solvent cleans in acetone, methanol, and IPA (isopropyl alcohol) followed by rinse in RO (reverse osmosis) water.
Spin resist	Resist is applied to the surface using a syringe with a 0.1 $\mu\text{m}$ filter spun at 4000 rpm for 60s.
Soft bake	90 °C for at least 30 minutes to remove solvent from resist solution.
Expose pattern	Using mask aligner, exposure time is dependent on the resist used and the feature size, S1818 resist is exposed for $\sim 11$ s.
Develop pattern	S1818 resist developed in 1: 1 solution of H <sub>2</sub> O: Microposit developer solution at room temp for 75 s.
Post treatment	120 °C for approx. 30 min if required

Fig. 2.2 shows the idealised photolithography process. The exposed areas are removed after development leaving nice sharp clean edges to the features. However, in a real environment a number of other things also happen.

Diffraction caused as the light travels through the mask to the resist and also through the resist layer can cause broadening of the features as shown in Fig. 2.3. For large features this effect has minimal impact but for small or densely packed features it may become significant. This can lead to what is known as the proximity effect. If a number of features are exposed in a densely packed pattern then the slight spreading of light from each individual feature can cause the resist between the features to be sufficiently exposed that it will be removed in the development process.

The other problem is exactly the opposite. A certain dose of light is needed to completely expose the resist. For very small features the dose

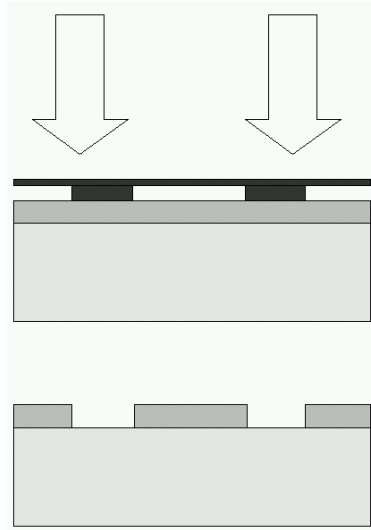


Figure 2.2: The photolithography process. Exposure of the resist and development of the pattern.

of radiation falling on the exposed area over the exposure time may not be sufficiently high. This results in incomplete resist removal after development. This is also fatal to device production as there will still be a layer of resist on the semiconductor stopping further processes being effective.

### **Mask production for photolithography**

The masks used for photolithography were produced using electron beam lithography. In order to make a mask of the required design a design file is first created. This was done in a semiconductor layout design package called Wavemaker (Wam). Hierarchical layout files are produced made up of a number of different individual cells. Individual cells can be combined to create a complete design which then forms a separate cell. All cells are saved within a single file. These can then be transferred to be written by electron beam lithography onto a mask plate. The process of design transfer will be

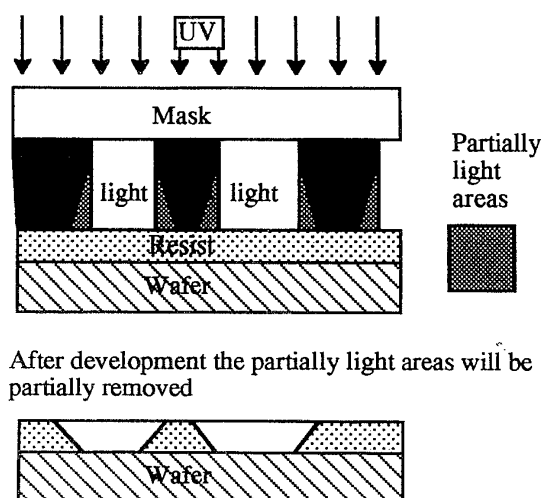


Figure 2.3: The feature spreading caused by light diffraction as it passes through the mask and resist [16].

discussed later in this chapter.

The masks are made from glass plates in a variety of sizes. For example 2.5, 4, and 5 inch plates are available, coated in  $0.1 \mu\text{m}$  Cr (chromium). This allows only 0.1 % transmission of the UV light through those areas that are still covered. The mask plates can also be copied onto a ferric oxide covered plate. This has the advantage of allowing partial transmission of light allowing for more accurate registration of the samples. The mask copying process introduces a slight loss of resolution but this is not important for large features, only having an effect as the registration limits are approached.

### **Advantages and disadvantages of photolithography**

The main advantage of photolithography is that the process is reproducible and relatively quick. From the first clean of a sample it can take as little as a few hours to complete a layer of lithography. This has great benefits when

working with a large number of samples as the longest processes, i.e. the soft baking of the resist, can be done at the same time for all samples. This reduces the overall turnaround time. Also photoresist is a relatively robust compound which is suitable for a number of other fabrication steps as will be discussed later in this thesis.

Disadvantages to photolithography primarily come from the relatively poor registration size. The minimum critical distance for the optical lithography system which was used is  $\sim 5 \mu\text{m}$ . Also the limits to the feature sizes caused by the proximity effect and incomplete exposure of small features means that photolithography is of limited use when processing manually.

## 2.2.2 Electron-beam lithography

### Physical parts of electron-beam lithography machine

Electron beam (e-beam) lithography is the other method that was used for substrate patterning. In this case an electron beam is used to transfer a pattern into an e-beam resist. This is similar to a photoresist but sensitive to electrons rather than electromagnetic radiation. The equipment is very similar to a scanning electron microscope except rather than simply scanning back and forward it has a sophisticated computer control system in place.

E-beam lithography was done on an EBPG5 HR 100 made by Leica. Fig. 2.4 shows a schematic of the equipment. Here can be seen the physical parts of the machine from the electron gun at the top through to the condenser lenses and the substrate. The lenses themselves are formed from electromagnets. The first is used to focus the beam onto the blanking plate, which controls the direction of the beam electrostatically and can direct it to a beam stop when required.

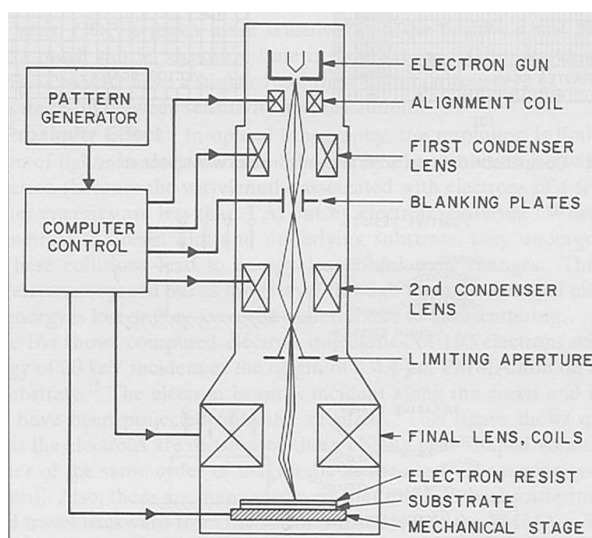


Figure 2.4: This is a schematic for an e-beam lithography system showing the major components used for controlling the beam [14].

The second condenser lens is used to focus the beam onto the limiting aperture, the latter is variable in size to allow for different spot sizes. The change in spot size allows many different sized areas to be written as efficiently as possible. Large areas are best written with a large spot and small areas with a small spot, with spot sizes ranging between 12nm and 400 nm. This allows a wide range of feature sizes to be covered with a minimum of time wasted.

The final beam coils are used to move the beam around relative to the pattern required. However the deflection available while still remaining a focused beam is relatively small. To cope with larger patterns the whole substrate can be moved on the mechanical stage to allow different parts of a large design to be stitched together to produce the final pattern. The stitching distance is 800  $\mu\text{m}$ . This can sometimes cause problems, known as stitching errors, whereby the next section is written a short distance away

leaving an unexposed area between the pattern blocks. All of these functions have to be very precise, so the whole process is computer controlled, as shown.

### Computer control of electron beam lithography

As has been mentioned, for e-beam lithography a design file is created in the Wam layout design package. This is then converted to a format which can be understood by the control system of the lithography machine. A number of different files are produced at different stages for each design to ensure that all of the required data is available. The first step is to convert

```

Format:5HR50      Function:VOID      Resolution:0.05
Units:MICRON      Justify:CENTER    Height:800 [16000]
Compact:NO        Reverse:NO        Width:800 [16000]
Pregrid:NO       Overlaps:NO       Grow:0
Precut:YES       Produce:CFLT      Rule:SQUARE      Border:OUTSIDE
Join:YES         Select:NO         Twosided:YES     Tag:
                  Keep:NO

      Input:($TED/transcript_db.clib)
      Structure:
      Layers:
      Limits:

      Sizing:0
      Scale:1
      Orientation:0
      Output:($TED/lmctranscri_db.cflt)
CATS 10:19:01 SunOS 5.7 RELEASE
Copyright 1986-2000 Transcription Enterprises Limited, Los Gatos, CA
$TEC/start_up.cinc setting PREGRID to NO
Command: █

```

Figure 2.5: The interface window for CATS, one of the e-beam conversion programs.

the format of design file, which is a *.gds* file. This is converted to a *.clib* file format, where *clib* stands for CATS library. CATS is the name of the program which carries out the first stage of the conversion process. Fig. 2.5 shows the interface screen for CATS. CATS takes the input *.clib* file and allows selection of a single cell from the library, which is called a structure.

Information about different layers within the structure is given along with the spatial size. These can be changed to allow part of a structure to be written, i.e. a single layer or selected area of a layer.

The resolution and required beam energy is also entered at this stage. Resolution affects the edge definition of the pattern to be written while the beam energy has an effect on the minimum feature size that it is possible to write. Another important piece of information at this point is whether the design is to be reversed. Normally the shapes in the pattern are written. However, a reversed image will write the area around the shapes. This is one method to produce isolated features; others will be discussed later. CATS outputs a *.cftt* file which automatically generates a number of file types *.dat*, *.cinc*, *.log*, and *.log\_long*. The next stage in the conversion process uses

```

USERNAME: L.CUNNINGHAM [M.RAHMAN]      GROUP: Physics      CALIB: cell
SUBSTRATE: 9.2,9.2                      KVOLTS: 50         Job Time: 1.30 hours
OUTFILE: wrc0003.com                    JOB_TYPE: registration MATRIX: 1

PATTERN: 1mctrails3_00                  RESOLUTION: 0.10000
POSITION: 9.69600,13.05900              DOSE: 300.0        SPOT_SIZE: 80 <6.93>
STEP_SIZE: 2.3700,2.3700                COMPLEX: NO
REPEATS: 2,3                             IDENTIFIER:
CENTRE: -1.34000,-1.34000              FIRSTMARK: 0,0     MARK_TYPE: RECT
CROSS: 7.326,9.504                      MARK_SIZE: 40.0,40.0 MARK_CONT: POSITIVE

belle version 4.00
Command: exec wrc0003
Command: █

```

Figure 2.6: The interface window for BELLE, one of the e-beam conversion programs.

a program called BELLE. This takes files created in CATS and produces the final output file. BELLE is where the information about the pattern is

entered. The *spot size* and *dose* commands affect the physical size of the beam and how long the beam remains in one location. These can have a dramatic effect on the write time of the job. A small spot size with a high dose will have much longer write time than a larger spot size or lower dose. BELLE allows arrays of the same pattern to be written, using the *Repeats* command, with a spacing given by the *step\_size*. The size of the substrate and the position of the pattern on the substrate are also entered here.

A number of different job types are available which affects the information required. Shown in Fig. 2.6 is a registration job. This is used when the pattern being written is to be aligned to previous lithography steps. The information is entered here to allow the pattern recognition software in the beam writer to find a given reference on the sample called an *alignment mark*. The distance from the alignment marks to the position where the pattern will be written is also entered. This allows very accurate alignment to previous layers of lithography depending on the chosen resolution. Other job types available are *simple*, which is used to write patterns where no alignment is required, and *exposure test* which is used to write a number of patterns at a range of doses to find which gives the best results depending on feature size and spacing.

### **E-beam patterning**

Standard e-beam processing is very similar in outline to photolithography. The resist is spun onto the sample face and soft baked to remove the solvent. However in e-beam there is a large range for each of the processes parameters. A large number of different resist thicknesses are available depending on the size and density of features to be written. This in turn affects the dose to be

used when writing the pattern. The variation in thicknesses lends itself to a range of development procedures. Development of a standard e-beam resist such as PMMA (polymethyl methacrylate) uses a solution of MIBK (methyl isobutyl ketone): IPA. The concentration of the solution is dependent on the feature size, the resist thickness and the density of the features. The process steps for e-beam patterning are shown Table 2.2 for a standard e-beam resist such as PMMA.

Table 2.2: Process steps for e-beam lithography for standard PMMA resist

Step	Parameters
Surface clean	Sequential solvent cleans in acetone, methanol, and IPA (isopropyl alcohol) followed by rinse in RO (reverse osmosis) water.
Spin resist	Resist is applied to the surface using a pipette with a spin at 5000 rpm for 60s.
Soft bake	180 °C for at least 30 minutes to remove solvent from resist solution.
Write pattern	Using EBPG5 HR 100 beam writer. Dose and write time etc. is dependent on the resist thickness, the size, and the density of features
Develop pattern	Pattern developed in solution of MIBK: IPA at 23 °C for 60 s.
Post treatment	180 °C for approx. 30 min if required

### Advantages and disadvantages of e-beam lithography

The advantage of e-beam over photolithography is the extremely accurate registration distance and the small feature size that can be written. Aligning patterns with a critical dimension of less than  $\sim 5 \mu\text{m}$  is very difficult in manual photolithography while e-beam has a registration size which can be measured in nanometres. Also because of the method of writing the

patterns it is possible to produce much more densely packed features than in photolithography. The individual spots written in e-beam diverge due to scattering in the resist but this is insignificant compared to photolithography.

Electron beam lithography has one major disadvantage, it is a linear process not a printing type process. Each section of the pattern is written sequentially in small sections. This is considerably slower than the whole pattern printing process of photolithography. Other problems arise from the fact that e-beam resists are generally much thinner than photoresist making them less suitable for some types of processing. Also, e-beam has a slow turn around. Jobs to be written are loaded into the beam writer and run overnight so the minimum time to find out if a pattern has written successfully is 24 hours compared to 1- 2 hours for photolithography.

### 2.2.3 Resist types

#### Photoresist

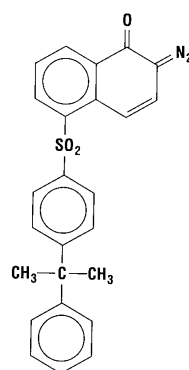


Figure 2.7: Structure of DQ (diazotriphenylmethane sulfone) [15].

Photoresist is a compound made of an inhibitor which is photo-sensitive and a resin base. The resin itself is soluble in an alkaline solution but the inhibitor halts this process. The photo-sensitive inhibitor breaks down when exposed to UV (ultra-violet) radiation allowing the resin to dissolve. The most common photoresists are DQN resists. These are named after the two components in the resist. DQ (diaz-quinone) is the photo-active inhibitor, while N (novolac) is the resin. The novolac resin is a long chain molecule which dissolves in an alkaline aqueous solution. Addition of the DQ inhibitor changes the chemistry so that the resist is no longer soluble in alkaline solutions. The resin itself is resistant to acids and its long chain molecule means that it is suitable for many plasma processes.

DQ (diaz-quinone) is sensitive to UV radiation, Fig. 2.7 shows the structure of the compound [15]. The structure from SO<sub>2</sub> down is specific to different manufacturers. The top section contains one benzene aromatic ring with a second double bonded benzene ring which has a weakly bonded nitrogen (N<sub>2</sub>) atom and a covalently bonded oxygen (O) atom. Fig. 2.8 shows how the chemical structure changes after exposure to UV radiation. The weakly bonded nitrogen is freed leaving a reactive carbon site. This is stabilised by a carbon atom moving outside the ring, called a Wolff rearrangement. The final stage is the absorption of water during the development phase which causes a conversion to carboxylic acid. Carboxylic acid readily reacts with and dissolves in alkaline solutions while the freed N<sub>2</sub> causes a foaming effect aiding removal.

The exposure to UV and subsequent decay of the inhibitor allows the removal of photoresist in specific areas determined by the pattern of the mask. The length of the exposure is determined by the thickness of the

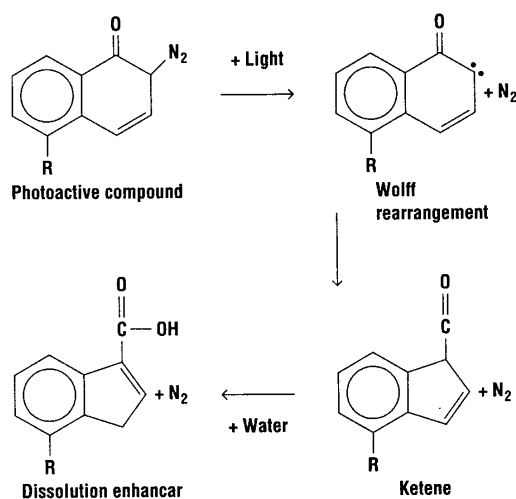


Figure 2.8: The chemical changes in DQ after exposure to UV radiation [15].

resist layer. Fig. 2.9 shows the sequential nature of the breakdown of the inhibitor. It is easy to see why the exposure time can vary significantly for different types and thicknesses of resist. Another factor which affects the exposure time is the size of the features and how densely packed they are. Small densely packed features will quickly become over exposed by the proximity effect as shown in Fig. 2.3 meaning great care has to be taken in deciding upon the exposure time for different patterns

### Negative resist

The previous description was of a positive tone resist. Another type of resist called a negative resist works in the opposite fashion. Instead of the exposure to UV radiation causing dissolution of the photoactive inhibitor agent, as in a positive resist, the UV causes cross-linking of the polymers in the resist. Crosslinking is the process by which several of the resist's long chain polymers becoming attached to each other changing the chemical properties.

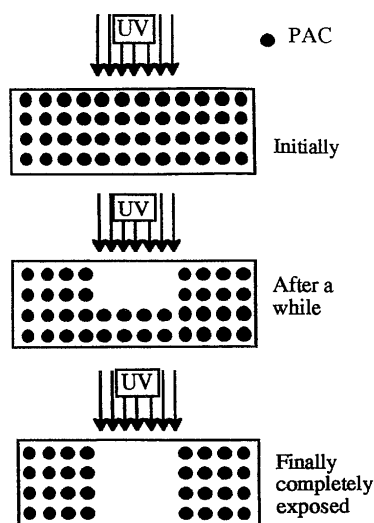


Figure 2.9: The breakdown of the alkaline resistant PAC during exposure to UV light [16].

Crosslinking renders the exposed areas more resistant to the developer solution causing preferential removal of unexposed areas. This type of resist is developed in an organic solvent rather than an aqueous solution. Problems occur during the development with the absorption of solvent into the remaining resist which can cause swelling and distortion of patterns.

### **E-beam resist**

For e-beam lithography the most common resist is PMMA (polymethyl methacrylate). PMMA is a long chain polymer compound which is acid and alkaline resistant. The compound is also resistant to most organic solvents except acetone. E-beam resists are different from photoresists as when the resist compound is exposed to the electron beam a number of reactions take place unlike photoresists which are designed so that only the desired reaction takes place. These reactions include cross-linking as well as disruption. Cross-

linking renders the compound resistant to the developing solvent and so is unwelcome in a positive resist. The design of the resist has to maximise the required reaction, i.e. disruption for a positive resist. In PMMA the rate of dissolution is much higher than that of cross-linking while for a negative resist such as HRN cross-linking is the more common result.

When the resist is exposed to the electron beam it causes the polymer chains to break up in those areas. The polymer fragments are typically 100Å in length. This changes the chemical properties of the exposed compound, making exposed areas soluble in the organic solvent MIBK (methyl isobutyl ketone). Development of the resist occurs in a solution of MIBK: IPA (isopropyl alcohol).

Another type of e-beam resist is UVIII. UVIII is a chemically amplified resist (CAR) from Shipley which is sensitive to e-beam patterning while still being optically sensitive. CARs have an added photoacid generator (PAG) which causes the release of an acid that attacks the base when it is exposed to radiation. This makes it very quick to expose optically. It also requires a very low dose when being patterned using e-beam. The main advantage of this is the reduction in the write time due the decreased exposure required. The process for applying UVIII is slightly different from that for PMMA, Table 2.3 shows the process steps required to produce a pattern in UVIII. The table shows that the process here varies from the PMMA process with the application of the adhesion promoting primer and the need for two bake cycles. The PEB is the more critical step as it activates the chemical amplification for dissolution of the inhibitor agent in the latent exposed image. This is visible to the eye during processing. UVIII is more resistant to plasma processes than does PMMA. Additionally the exposure dose required is reduced

Table 2.3: Process steps for e-beam lithography using UVIII CAR resist.

Step	Parameters
Surface clean	Sequential solvent cleans in acetone, methanol, and IPA (isopropyl alcohol) followed by rinse in RO (reverse osmosis) water.
Spin on primer	hexamethyl disilazane (HMDS) adhesion promoter 4000 rpm 30 s
Bake primer	90 °C 15 minutes
Spin resist	Resist is applied to the surface using a pipette with a spin at 4000 rpm for 60s.
Post-application bake (PAB)	135 °C for 1 minute to remove solvent from resist solution.
Write pattern	Using EBPG5 HR 100 beam writer. Dose and write time etc. is dependent on the resist thickness, the size, and the density of features
Post-exposure bake (PEB)	130 °C for 1 minute to activate the PAG in the latent exposed image
Develop pattern	Pattern developed in CD26 developer at room temperature for 60 s.

by a factor of 10 or more from more standard PMMA resists.

## 2.3 Lift off and contact definition

Lithography is the process of transferring the pattern to a resist compound. A common next step is the application of metals to the surface. This is important for a variety of reasons which will be discussed later in this thesis.

### 2.3.1 The lift off process: Photolithography

For lift off, the resist is patterned by either photo- or e-beam lithography. Next the the whole surface of the sample is covered with a layer of metal or multiple layers of metal. Immersion in solvent removes the remaining

resist along with the metal covering it. This leaves only the areas which were exposed during the lithography with metal, as shown in Fig. 2.10

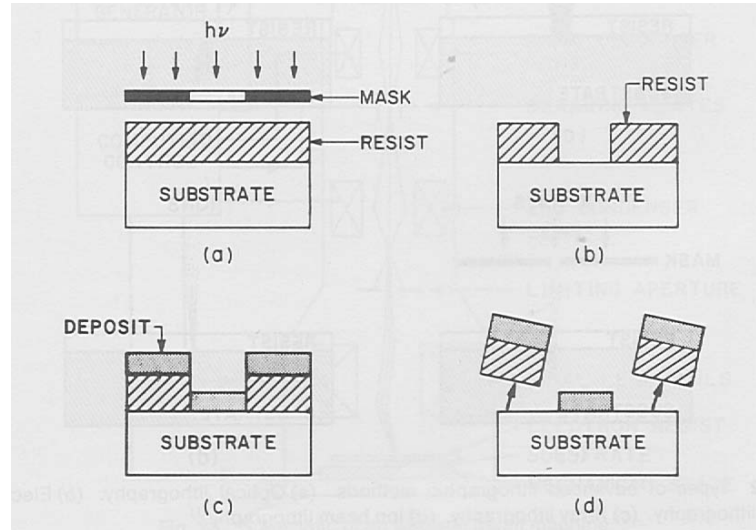


Figure 2.10: The process of lift off definition of metals [14].

The process of lift off is very dependent on the resist profile after the pattern has been developed. Features with a low aspect ratio or rounded resist profile will lift off poorly if at all. Fig. 2.11 shows a number of suitable profiles for lift off. Evaporated metal travels perpendicularly to the surface producing very little horizontal spread so even for the sloped sidewalls of Fig. 2.11 *a* a break in the film should occur provided the metal is sufficiently thinner than the resist. Fig. 2.11 *b*, and *c* show how the resist profile can be changed by the use of a solvent soak prior to the exposure of the resist. These techniques are particularly useful for small features.

### 2.3.2 The lift off process: Electron beam lithography

The method to improve resist profile for lift off is different in e-beam lithography than in photolithography. Surface solvent soaks are not an option. To

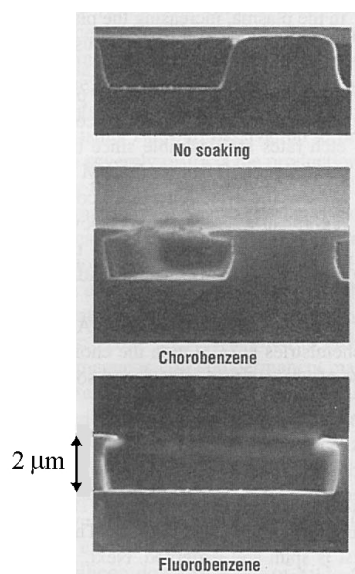


Figure 2.11: The effect of different solvent soaks on the resist profile for lift off processing. *a* no soak, *b* chlorobenzene soak, and *c* fluorobenzene soak [15].

improve the resist profile a bi-layer or more infrequently a tri-layer of resist can be used. This employs resist solutions of different molecular weight to produce an overhanging profile. This method also produces a thicker resist layer for lifting off thicker layers of metal. This greatly improves the likelihood of successful lift off. By layering high molecular weight resist on top of a lower molecular resist the profile shown in Fig. 2.12 can be achieved

### 2.3.3 Advantages and disadvantages of lift off

Lift off is a standard process used to produce metal features on the semiconductor substrate. The advantage is that the process does not use any caustic substances so it is suitable for use with all substrate types. Also, it allows patterning of non-reactive metals such as gold or platinum. The resolution achievable using lift off is limited by the type of lithography used to produce

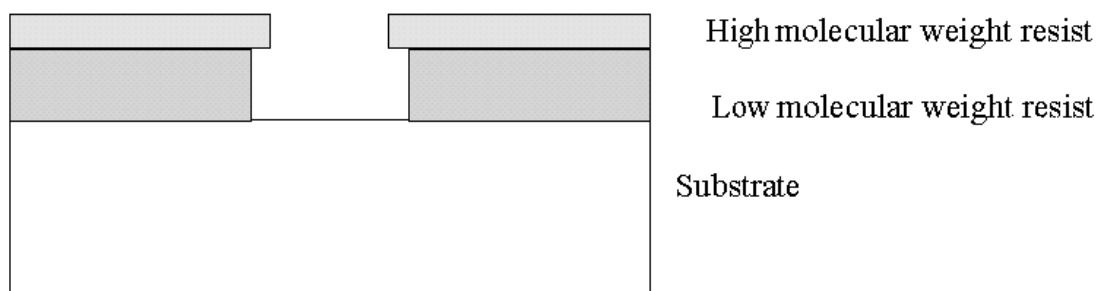


Figure 2.12: Bi-layer of e-beam resist used to create overhanging profile for lift off.

the pattern so that when an e-beam produced pattern is lifted off it can produce very fine densely packed features.

The biggest disadvantage of lift off is that the unwanted metal can resettle elsewhere on the substrate. This can render a given device or structure useless. The other main problem with this technique is that the entire layer of metal can come off. This is usually caused by a poor resist profile and can generally be avoided by using one of the profile improvement techniques methods discussed previously.

# Chapter 3

## Introduction to plasma theory and reactor types

### 3.1 Introduction

The word *plasma* comes from the ancient Greek word *plásma* meaning ‘something formed or moulded’. It was introduced to describe ionised gases by Tonks and Langmuir [17]. A plasma consists of a gas of charged particles, in which the potential energy of a typical particle due to its nearest neighbour is much less than its kinetic energy.

Plasmas are used in many applications, from lighting tubes to commercial ozone producing equipment. One of the fastest growing areas for the development of plasma equipment is in electronics [18]-[21] where the ever increasing drive to reduce the critical feature size of microchips has led to a drive in the technology development for plasma processing reactors. Here I will describe the basics of the theory governing plasma generation and a number of processes using two of the main commercially available pieces of equipment, a reactive ion etch (RIE) tool and an inductively coupled plasma (ICP) etch tool.

Table 3.1: The different current-voltage regimes of a DC electrical discharge.

A	<b>Dark discharge</b> Background ionisation Saturation regime Townsend regime
B	<b>Glow discharges</b> Normal glow discharge Abnormal glow discharge
C	<b>Arc discharges</b> Glow to arc transition Nonthermal arcs Thermal arcs

## 3.2 Basic plasma theory

Plasma theory is a very large and complicated area of physics. Presented here is an overview of the fundamentals as related to the application of plasma etching and deposition. For a more complete treatment ‘Industrial plasma engineering’ volumes 1 and 2 by J Reece Roth [22, 23] covers all aspects of the generation, development, and evolution of plasma discharges. Additional information was taken from ‘The science and technology of microelectronic fabrication’ by S.A. Campbell [15] on some of the industrial specific applications for plasma processing.

Classical plasma experiments use a vacuum sealed cylinder with an electrode at either end containing a pressurised gas. Plasma can be generated by applying a DC bias between the electrodes. A low pressure DC electrical discharge undergoes a number of current-voltage regimes, which are listed in Table 3.1.

The variation of the current as bias voltage is increased is shown in Fig.

3.1. The region of interest for the processes which are to be considered later in this chapter is the glow discharge regime. However, a brief description of the other regions will be included for completeness.

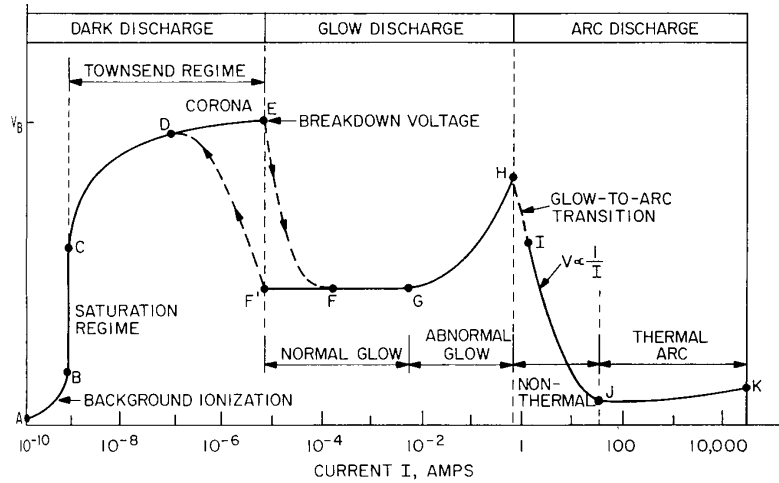


Figure 3.1: The different regimes through which a DC discharge progresses as the ion current increases [22].

### A: Dark discharge

The dark discharge region is so called because it gives off no light except for some of the more energetic corona discharges. This is the section of the current-voltage curve below the glow region. As the applied voltage is increased the current measured in the discharge tube changes through a number of stages. These are:

#### Background ionisation

Ionisation caused by cosmic rays etc. means that there will always be a finite amount of free charge within a gas. Applying a low potential begins to slowly sweep this charge toward the anode and cathode for electrons/ ions respectively. The current,  $I$ , generated in this region increases with applied

bias as the acceleration of charges increases.

### **Saturation regime**

In the saturation region all of the available background radiation produced ions/ electrons have been collected causing a steady current. The electric field is not high enough to produce any new ionisation. The voltage can increase without changing the current. In this region the current  $I_s$ , the saturation current, is independent of voltage but linearly dependent on the level of background ionisation. This is similar to the operation of a Geiger-Müller tube.

### **Townsend discharge**

Processes of industrial importance begin to occur in the Townsend regime, including corona discharges and electrical breakdown gases. The increase in current has a number of causes. The most important of these are the production of secondary electrons within the gas caused by collisions and emission of secondary electrons from ions impacting on the cathode. This leads to an exponential increase in the current up to the breakdown point. Here the discharge switches into the glow discharge regime signified by a drop in the potential required to maintain a current in the gas.

### **B: Glow discharge region**

This is the section of interest for industrial applications and will be discussed in more detail later.

### **C: Arc Discharges**

On the other side of the glow discharge region lies the arc discharge region. When a glow discharge has entered the high current section it is difficult to

tell the difference between a glow and an arc. The defining characteristics of an arc are its high luminosity, large current, and low cathode fall voltage. The different types of arc discharge are detailed briefly below.

#### **Glow to arc transition**

When the current in a glow discharge gets very high the cathode temperature increases. When the cathode becomes hot enough to become a source of electrons the glow to arc transition takes place. During this transition the current increases, luminosity increases, and the voltage required to maintain the current decreases.

#### **Non thermal arc discharges**

The first stage that a discharge reaches after the glow to arc transition is the *non-thermal arc* also known as a *low intensity arc*. Other names for the same arc are the *thermionic* or *low pressure arcs*. This type of arc is distinguished by having a high current with a gradually lowering voltage. The luminosity is much greater than the glow discharge. Other features are high electron density and temperature.

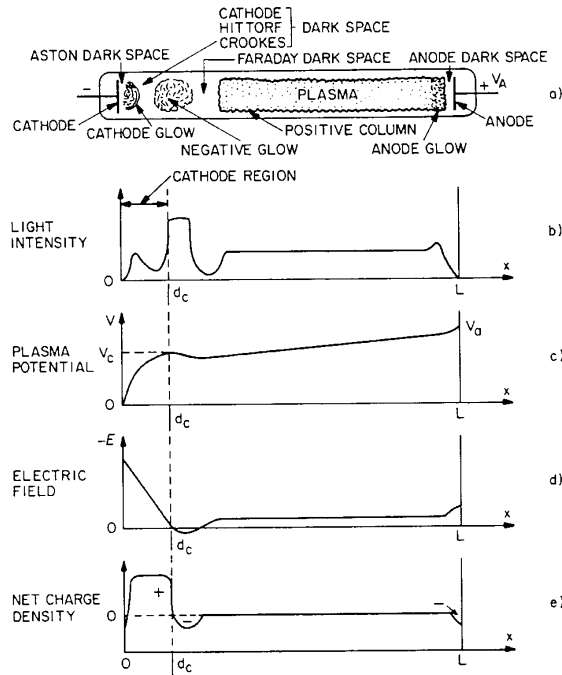
#### **Thermal arc discharges**

Increasing currents in the discharge eventually moves the discharge to a thermal arc. In this case the currents are very high, up to 10 kA, and very high electron temperatures and densities are found. The luminosity for thermal arcs is even higher than the non-thermal arc with the discharge becoming opaque.

### **3.3 DC glow discharge**

The region of interest in the DC discharge regime is the glow discharge. The name arises from the luminosity of the plasma, which is caused by excitation

collisions of sufficiently high energy to give off visible light. Fig. 3.3 shows the structure of a glow discharge for a standard low pressure discharge tube. Also shown are the luminosity, plasma potential, electric field, and net charge density variations along the length of the discharge tube. The individual



d) Figure 3.2: Structure of DC glow discharge and variations of light intensity, plasma potential, electric field, and net charge density along the discharge tube.[22]

sections are observed over a large range of operational characteristics and are generally named after the first person to observe or investigate them.

### 3.3.1 Regions of a normal glow discharge

Beginning from the cathode at the left in Fig. 3.3 the regions of the DC glow discharge plasma are as follows:

#### Aston dark space

This is a thin region immediately to the right of the cathode. It has a high electric field and a negative space charge. This contains slow electrons which are accelerated from the cathode. Electrons here are of too low an energy/

density to glow so it appears dark.

### **Cathode glow**

The cathode glow has a relatively high ion density. The glow is caused by incoming positive ions or ions sputtered from the surface of the cathode. This cathode glow can sometimes obscure the Aston dark space.

### **Cathode dark space**

This region is variously called the Crookes or Hittorf dark space after the British and German researchers who investigated it. It has a moderate electric field, a positive space charge, and a relatively high ion density.

### **Cathode region**

The cathode region, between the cathode and the boundary between the cathode dark space and the negative glow, is where most of the tube's voltage drop occurs. The width of the cathode region is  $d_c$  and the potential across it is the *cathode fall voltage*  $V_c$ . Most of the power dissipated in a glow discharge occurs in the cathode region. In this region electrons are accelerated to produce avalanching and ionisation in the negative glow and regions to the right.

A low pressure glow discharge will adjust the length of the cathode region to match the relation:

$$d_c p = (dp)_{min} \quad (3.1)$$

This product is called the *Paschen minimum* where  $d_c$  is the cathode distance,  $p$  the pressure, and  $dp$  is the minimum pressure/ distance coefficient. At the Paschen minimum, the discharge maintains itself under the minimum cathode fall voltage and power dissipation. In a normal discharge the current density remains reasonably constant as the increasing current causes a larger area of the cathode to be used.

**Negative glow**

Immediately to the right of the cathode dark space is the *negative glow*, this is the brightest region in the discharge. The negative glow has a relatively small electric field. Electrons which have been accelerated from the cathode produce ionisation and intense excitation here. Electron densities are typically  $10^{16}$  electrons/m<sup>3</sup>.

**Faraday dark space**

This region is found after the negative glow. Because of the high rates of ionisation and excitation in the negative glow, electron energies are low. The net space charge is very low and the axial electric field is weak.

**Positive column**

This is the region which is closest to the classical description of a plasma. In the positive column the electric field is low, just large enough to maintain the required amount of ionisation at the cathode end. The electron density is in the region  $10^{15} - 10^{16}$  electrons/m<sup>3</sup> with an electron temperature of 1- 2 eV. In the positive column the numbers of electrons and ions are approximately the same giving a net charge of zero. Lengthening the discharge tube at a constant pressure ( $pd_c = \text{constant}$ ) causes a similar lengthening in the positive column while the cathode region stays the same size.

**Anode glow**

This is a slightly brighter region at the anode end of the positive column, which is not always present. It is the boundary of the anode sheath.

**Anode dark space**

The anode dark space between the positive column and the anode is also called the anode sheath. This has a negative space charge due to electrons travelling from the positive column to the anode, and a higher electric field

than the positive column.

Other configurations of glow discharge are possible in the glow discharge region. *Striated discharges* have a number of moving or standing striations, which are moving or standing perturbations in the electron number density. Striations have an undesired effect on glow discharge especially for industrial processes where parameters may be critical.

An *abnormal glow discharge* is one where the voltage has to be increased to increase the current density any further as the plasma has covered the whole surface of the cathode. The abnormal discharge looks similar to the normal discharge except the structures close to the cathode can blend into one another to provide a constant glow from cathode to anode.

*Obstructed discharges* occur when the length of the discharge is less than  $d_c$  the Paschen minimum distance the cathode fall voltage then has to rise above the Paschen minimum value  $V_{c,min}$ . This is desirable in many applications as the increased potential causes greater acceleration of ions and electrons.

### 3.3.2 Theory of glow discharges

Here I will discuss some of the equations and relations which can be used to model the behaviour of a plasma. To a good approximation the properties of a normal glow discharge adjust themselves so that the Paschen minimum is achieved i.e.  $pd_c \approx (pd)_{min}$ . The cathode fall voltage is given by  $V_c = V_{b,min}$  where  $V_{b,min}$  is the minimum breakdown voltage. The minimum breakdown voltage is a property of the gas used in the plasma and depends on the value of  $pd_c$ .

### The Townsend theory of the cathode region

Early investigations of the cathode region by F. W. Aston [24] reported that the electric field in the cathode region is approximately linear:

$$E = C(d_c - x). \quad (3.2)$$

$C$  is a constant and  $d_c$  is the cathode distance. Integrating this gives the cathode voltage at a position  $x$

$$V = \int_0^x E dx = C \left( x d_c - \frac{x^2}{2} \right). \quad (3.3)$$

By applying boundary conditions at  $x = 0$  and  $x = d_c$

$$V(0) = 0 \text{ and } V(d_c) = V_c.$$

The constant of integration may be written as

$$C = 2V_c/d_c^2$$

which when substituted into Eqn. 3.3 gives

$$V(x) = \frac{V_c x(2d_c - x)}{d_c^2} \quad (3.4)$$

for the potential at a point  $x$  from the cathode within the cathode region.

The electric field within the cathode region is given by differentiating Eqn. 3.4 to give

$$E = \frac{dV}{dx} = \frac{2V_c(d_c - x)}{d_c^2}. \quad (3.5)$$

The net charge density for the cathode region can be determined from Poisson's equation by defining a charge density of

$$\delta n = Zn_i - n_e$$

where  $Z$  is charge of each ion,  $n_i$  is the number density of ions, and  $n_e$  is the number density of electrons.

Poisson's equation for the axial dimension of the normal glow discharge may be written as

$$\frac{d^2V}{dx^2} = -\frac{e\delta n}{\epsilon_0} = -\frac{2V_c}{d_c^2}. \quad (3.6)$$

The second derivative of Eqn. 3.4 may be inserted into the right hand side of Eqn. 3.6. Solving for the net charge density then gives

$$\delta n = \frac{2\epsilon_0 V_c}{ed_c^2} \quad (3.7)$$

which is a constant, positive net ion number in the cathode region.

### Lorentzian plasma equations

In this section a parallel plate configuration, as shown in Fig. 3.3, will be considered for calculation of the power dissipated in the discharge.

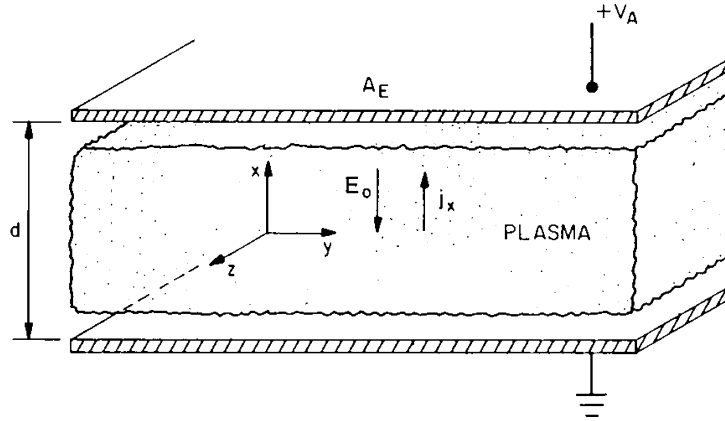


Figure 3.3: A schematic of a parallel plate reactor showing variables required to calculate the power input into a normal unmagnetised DC glow discharge [22].

The Lorentz model describes a plasma where the electrons lose their momentum to collisions with the neutral background gas with collisions of frequency  $\nu_c$ . The equation of motion for individual electrons using the configuration of Fig. 3.3 is

$$\mathbf{F} = m_e \mathbf{a} = m_e \frac{dv}{dt} = -\nu_c m_e v + e \mathbf{E}. \quad (3.8)$$

$\mathbf{F}$  is the force on an electron,  $m_e$  is the mass of an electron,  $\mathbf{a}$  is the acceleration on the electron,  $\nu_c$  is the collision frequency,  $V$  is the velocity of the electron, and  $\mathbf{E}$  is the electric field.

In a DC field Eqn. 3.8 becomes

$$\frac{dv}{dt} + \nu_c m_e v - \frac{e \mathbf{E}_0}{m_e} = 0 \quad (3.9)$$

Assuming an initial condition of  $v(t) = v_0$  at  $t = 0$  it is possible to calculate from Eqn. 3.9 a drift velocity

$$v_d = \frac{e E_0}{\nu_c m_e} = \mu_e E_0, \quad (3.10)$$

where  $\mu_e$  is the electron mobility.

The power absorbed by an electron is given by

$$p = \frac{dW}{dt} = e E_0 \frac{dx}{dt} = e E_0 v_d \quad (\text{W/electron}). \quad (3.11)$$

Substituting Eqn. 3.10 and assuming an electron number density of  $n_e$  the total power absorbed in the gas is

$$P = n_e p = \frac{n_e e^2 E_0^2}{\nu_c m_e} \quad (\text{W/m}^3). \quad (3.12)$$

The power dissipation in the plasma can be defined in terms of the energy of the electric field  $U$  and the electron plasma frequency  $\omega_{pe}$ , where

$$U = \frac{1}{2} \varepsilon_0 E_0^2 \quad \text{and} \quad \omega_{pe}^2 = \frac{n_e e^2}{\varepsilon_0 m_e}$$

$\varepsilon_0$  is the permittivity of free space, such that

$$P = U_{max}\nu_*. \quad (\text{W/m}^3). \quad (3.13)$$

$U_{max}$  is the maximum energy of the electric field and  $\nu_*$  is the energy transfer frequency defined as

$$\nu_* = \frac{2\omega_{pe}^2}{\nu_c} \quad (\text{Hz}) \quad (3.14)$$

This frequency is fundamental to the transfer of energy into the plasma and is a function of the electron number density, electron kinetic temperature, the gas, and the neutral background gas pressure.

This section has outlined the phenomenology of the DC glow discharge and some of the equations which can be used to model the plasma behaviour. Equations have been given to model the ion density in the cathode region, the cathode fall voltage and the power dissipated in the plasma. These are important for some of the plasma processes which will be discussed later in this chapter because the common configuration for an industrial plasma reactor has the samples for processing sitting on the cathode interacting with the large ion population that exists here. The cathode fall voltage  $V_c$  also governs how quickly the ions are accelerated towards the cathode surface.

### 3.3.3 Capacitively coupled RF glow discharge

Semiconductor plasma processes do not use DC discharges because of the danger of damaging the substrate. Instead for most applications a radio frequency (RF) discharge is used. This is governed by the same Lorentz equations as the DC discharge with the introduction of a varying electric field. The frequency of most industrial applications is 13.56 MHz which is well below the electron plasma frequency. This means that each electron

reacts individually to the electric field. One common configuration is the parallel plate geometry as shown in Fig. 3.4.

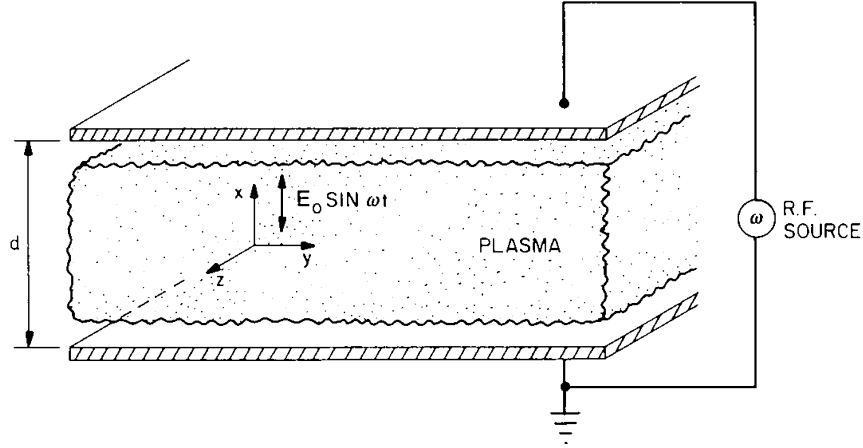


Figure 3.4: A schematic of a parallel plate reactor showing variables required to calculate the power input into a normal unmagnetised RF glow discharge [22].

For an RF power source the component of the electric field in the  $x$  direction is given by

$$\mathbf{E} = (E_0 \sin \omega t, 0, 0)$$

The force exerted on an individual electron is given by

$$\mathbf{F} = m\mathbf{a} = m\nu_c \mathbf{v} - e\mathbf{E} \quad (3.15)$$

where  $\nu_c$  is the frequency of collisions with neutrals. Because the electric field only has an  $x$  component the drift velocities in the  $y$  and  $z$  directions are not considered; any initial velocity in these directions are assumed to decay to zero very quickly. The  $x$  component of Eqn 3.15 is given by

$$m \frac{d^2 x}{dt^2} + m\nu_c \frac{dx}{dt} = eE_0 \sin \omega t \quad (3.16)$$

By integrating Eqn. 3.16 for  $x$  we can work out the constants of integration such that

$$v_x = \omega(C_1 \cos\omega t - C_2 \sin\omega t) \quad (3.17)$$

is the time dependent velocity in the  $x$  direction for electrons in the plasma.

From the calculation,  $C_1$  and  $C_2$  are given by

$$C_1 = -\frac{eE_0}{m} \frac{1}{\omega^2 + \nu_c^2} \quad (3.18)$$

and

$$C_2 = -\frac{\nu_c e E_0}{\omega m} \frac{1}{\omega^2 + \nu_c^2} \quad (3.19)$$

To calculate the power dissipated in the plasma we use the same method as for the DC discharge substituting  $E_0$  for  $E_0 \sin\omega t$  in Eqn. 3.11 and integrating over one period of the oscillation. The mean power absorbed per electron is found to be

$$\bar{p} = -\frac{eE_0\omega C_2}{2}. \quad (3.20)$$

Substituting for  $C_2$  from Eqn. 3.19 gives

$$\bar{p} = \frac{e^2 E_0^2}{2m} \frac{\nu_c}{(\omega^2 + \nu_c^2)} \quad (3.21)$$

Again as before the total power absorbed by the plasma can be given by assuming an electron number density  $n_e$  such that

$$\bar{P} = n_e \bar{p} = \frac{n_e e^2 E_0^2}{2m} \frac{\nu_c}{(\omega^2 + \nu_c^2)} \quad (3.22)$$

It is also possible to write the power absorbed in terms of the electrostatic

energy and the energy transfer frequency as in Eqn. 3.13. In this case we have  $\bar{U}$  the energy over an oscillation period so that

$$\bar{P} = \bar{U}\nu_* \quad (3.23)$$

and in this case  $\nu_*$  is defined as

$$\nu_* = \frac{2\omega_{pe}^2\nu_c}{(\omega^2 + \nu_c^2)}. \quad (3.24)$$

From the total power dissipated in the plasma the number density of ions can be calculated. The plasma has a net charge of zero so ion/ electron number densities are equal. Because of the cyclical nature of the RF power supplied to the reactor an ion current will flow in both directions. The potential drop between the plasma and each electrode is related by the ratio of the areas of the respective electrodes. For a parallel plate reactor the potential drops are related by

$$\frac{V_1}{V_2} = \left(\frac{A_2}{A_1}\right)^q \quad (3.25)$$

where  $V_1$ , and  $A_1$  refer to the powered electrode and  $V_2$ , and  $A_2$  refer to the grounded electrode. The exponent  $q$  varies over the range  $1 \leq q \leq 2.5$  For a system with a single powered electrode,  $q$  is calculated to be 2.

For industrial processes utilising an RF plasma reactor, such as RIE (reactive ion etching), the most common configuration is a parallel plate reactor with one driven electrode which is smaller than the grounded electrode. If running as a DC discharge, the reactor would be said to be an obstructed abnormal discharge with the plasma covering the entire cathode. The use of a smaller cathode and a single driven electrode means that the potential drop to the cathode is larger than to the grounded electrode. This ensures a



Table 3.2: Parameters for deposition of hydrogenated amorphous a-SiN<sub>x</sub>: H

Gas flows (sccm)	SiH <sub>4</sub> 10.5 NH <sub>3</sub> 44 N <sub>2</sub> (:He (85 % He) stress controlled) 171
Power (W)	30-40
Pressure (mTorr)	1000
Temperature (°C)	300
Deposition rate (nm/min)	15 (10 stress controlled)

trically isolating devices both from each other and from the atmosphere. The addition of a Si<sub>3</sub>N<sub>4</sub> layer also reduces surface leakage currents in semiconductor devices. Details of the applications for these layers are provided in later chapters.

There are a number of ways to produce dielectric coatings on surfaces but non-plasma processes involve high temperatures, > 700-800° C. The very high temperatures are essential to create active species in the gas by thermal excitation. However, these high temperatures can damage semiconductor devices. PECVD uses a low temperature deposition, at around 300° C. This is low enough that metals and deposited layers will not be affected. To avoid the high temperatures an RF discharge is used to create active species within the flow gas by ionisation. A reactor of the type shown in Fig. 3.5, however for PECVD the sample sits on the grounded electrode. This produces a much lower potential drop between the plasma and the sample ensuring that deposition takes place rather than etching. For PECVD of Si<sub>3</sub>N<sub>4</sub>, silane (SiH<sub>4</sub>) and ammonia (NH<sub>3</sub>) are used in a nitrogen ambient. For stress controlled Si<sub>3</sub>N<sub>4</sub>, the nitrogen ambient has He added to the gas mixture. Both of these produce amorphous hydrogenated Si<sub>3</sub>N<sub>4</sub>, a-SiN<sub>x</sub>: H. Table 3.3.4 gives the deposition parameters for stress controlled a-SiN<sub>x</sub>: H

The power is low for this application so as to reduce the potential drop between the plasma and the sample which in turn reduces the velocity at which ions arrive. High velocity ions can cause sputtering, physical removal of material from the sample surface through collisions. The transport of ions to the sample surface results in chemical reactions between different active species created in the plasma. The primary active species created from silane is *silylene*,  $\text{SiH}_2$ . This adsorbs on to the surface and the raised temperature causes the evaporation of the hydrogen leaving just Si on the surface. Ammonia produces a number of active species such as  $\text{NH}_2$  and  $\text{NH}$ . These react on the surface to leave nitrogen. The elevated temperature causes movement of ions on the surface. This leads to reactions on the surface between the Si and the N, producing  $\text{Si}_3\text{N}_4$ .

### 3.3.5 Reactive ion etching (RIE)

A parallel plate reactor of the type shown in Fig. 3.5 is one of the types most commonly used for RIE (reactive ion etching) with the sample sitting on the smaller powered electrode. RIE uses the flow of ions to the surface of the sample to remove material in a very controlled fashion. For modern semiconductor processing the feature sizes and densities are such that wet etching is not a viable option. Additionally for some of the more chemically inert semiconductors no viable wet etch exists. Wet etching is isotropic, etching in all directions at once. This causes sideways expansion of features and can cause adjacent features to come into contact. Because material removal in RIE is caused by ions accelerating towards the sample surface the etching produced is very anisotropic giving good verticality and no sideways expansion of feature dimensions.

Similar to PECVD the plasma in the chamber creates a number of active species from the working gas. Ions incident on the substrate surface remove material in two ways, by sputtering and by chemical reactions. Sputtering is the process of removing material by purely physical means. Collisions between the ions and the sample can expel material from the surface. Etch processes are designed to minimise the physical component of removal. As these can damage the surfaces left behind as well as introducing lattice defects into the top layers of the material. The preferred method of removal is chemical. When ions are incident on the surface of the sample, depending on the gas chosen, the reactions that take place can cause the formation of volatile compounds. These are then removed from the surface and transported away in the gas flow. This leads to minimal damage to the semiconductor surface and lattice although it cannot be completely removed.

RIE is generally done with the substrate held at about room temperature but a variety of processes are available which use higher or lower temperatures depending on the exact specifications. The exact processes used can encompass a large range of pressure, gas flow, plasma power and from that the bias potential between the plasma and the driven electrode. More details of the processes possible can be found in the next chapter where a number of different RIE processes are developed.

### **3.4 Inductively coupled RF plasma generation**

The previous section discussed the generation of a plasma by a capacitively coupled RF discharge in a parallel plate type reactor. Another configuration which is used for RF plasma generation is the inductively coupled discharge. A schematic for inductively coupled plasma generation is shown in Fig. 3.4

The power is transferred into the working gas using electromagnetic waves

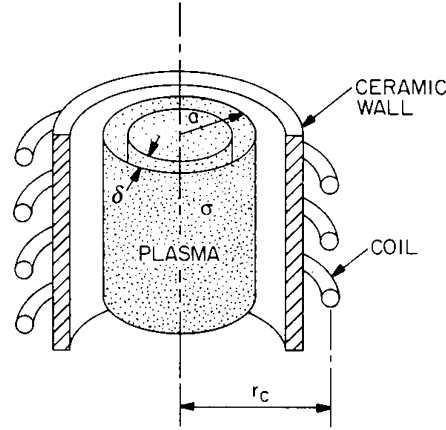


Figure 3.6: A schematic of inductively coupled RF plasma generation. [22]

from the RF current applied to the coil around the gas cylinder. An inductively coupled plasma is neutral with no net charge density, similar to a capacitive discharge. However, there are no DC fields within the plasma, unlike the capacitive discharge. The frequency most commonly used is 13.56 MHz. This is below the electron plasma frequency. Because of this each electron can react individually to the changes in the field direction. For an inductively coupled regime this means the interactions take place near the surface of the gas. This is known as the plasma skin. The electromagnetic wave is absorbed in the skin rather than propagating through the gas as it would have if the frequency had been above the electron plasma frequency.

The electric field,  $E$  of the incident wave is given by

$$E = E_0 \exp[i(Kz - \omega t)] \quad (3.26)$$

where  $E_0$  is the maximum field,  $z$  is the distance into the plasma,  $\omega$  is the frequency of the oscillation, and the propagation constant  $K$  is given by

$$K = \alpha + i/\delta. \quad (3.27)$$

The real part of  $K$ ,  $\alpha$ , represents the oscillating electromagnetic field while the imaginary part accounts for the absorption of the wave in the surface layer  $\delta$ . Both of the terms in  $K$  are related to the driving frequency of the RF generator and the properties of the working gas.

For industrial plasmas the following relation generally holds true,

$$\frac{\omega \varepsilon_0}{\sigma} = \frac{2\omega}{\nu_{*,0}} \ll 1 \quad (3.28)$$

where  $\omega$  is the driving frequency,  $\varepsilon_0$  is the permittivity of free space,  $\nu_{*,0}$  is the energy transfer frequency, and  $\sigma$  is the conductivity of the plasma. In this case if the conductivity is given by

$$\sigma = \frac{e^2 n_e}{m_e \nu_c} = \frac{\varepsilon_0 \omega_{pe}^2}{\nu_c}$$

then

$$\alpha \approx \sqrt{\frac{\sigma \mu_0 \omega}{2}} \quad (3.29)$$

and

$$\delta \approx \sqrt{\frac{2}{\sigma \mu_0 \omega}} \quad (3.30)$$

Substituting for  $\sigma$  and working through the constants leaves

$$\delta = 7.516 \times 10^6 \sqrt{\frac{\nu_c}{n_e \omega}} \quad (3.31)$$

This implies that the skin depth can be considered as the depth into a medium that the electromagnetic wave travels during one period of the electron plasma frequency. Because of this the ionisation all occurs within the skin. For industrial processes a uniform plasma is desirable. To produce a plasma with a uniform density of electrons, and therefore ions, the skin would need to extend to the centre of the column of gas. The frequency of the wave i.e. the frequency of the RF discharge is not subject to variation.

To ensure that the generated plasma is uniform throughout the volume of the working gas the pressure can be adjusted. Depending upon the exact value of the pressure the skin depth can be in the range 3- 30 cm. Fig. 3.7 shows how the skin depth changes for several values of the ratio  $\nu_c/\omega$  and the electron number density.

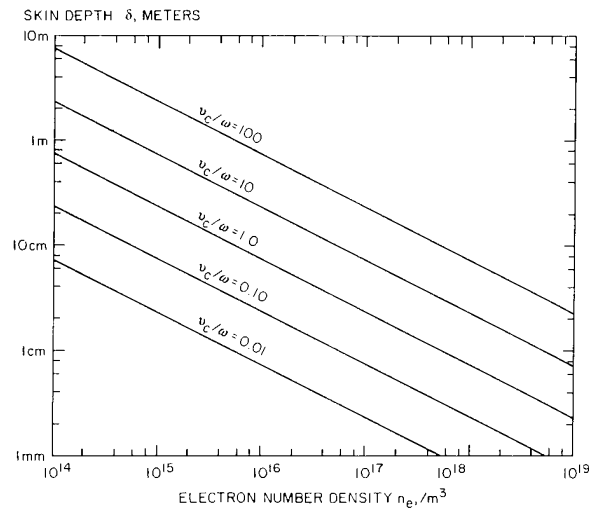


Figure 3.7: The variation in skin depth with different values of the ratio  $\nu_c/\omega$  for a range of electron number densities [22].

### 3.4.1 Inductively coupled plasma reactors

An industrial ICP (inductively coupled plasma) etching tool is used to produce a very dense plasma without having a very energetic ion flux to the surface of the sample. This is important for etching wide bandgap semiconductors which have a high bond strength, or for etching very deep features which would require very long etch times using a conventional RIE set up. The most common configuration for ICP reactors used for etching semiconductors uses a two chamber system, as shown in Fig 3.8

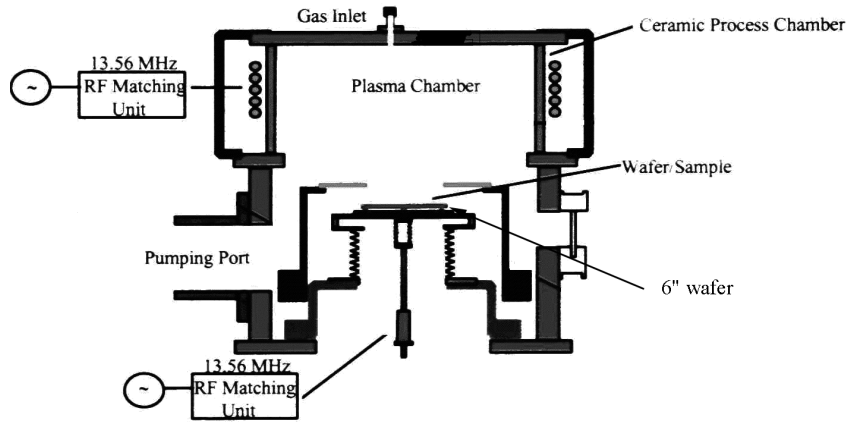


Figure 3.8: Schematic of industrial ICP reactor showing the two chambers used to separate ion production from the sample.

This type of reactor uses an ICP discharge to produce a dense plasma in a column held above the sample chamber. Because of the neutrality of the ICP plasma and the lack of DC currents, ions have no acceleration towards the sample surface. This allows a large RF power to be used, creating a much denser plasma than could be produced using RIE without damaging the sample. This is because RIE discharges have a single power source which is used to create the plasma and provide the dc bias to the substrate sitting on the powered electrode. So in order to create a denser plasma more power is needed which increases the dc bias by a corresponding amount which can cause lots problems.

The use of a second chamber allows ions to be drawn from the plasma and accelerated at a controlled rate towards the sample surface. A second RF power supply is then used to power the table which holds the sample. This sets up a capacitive discharge similar to an RIE discharge between the sample table held at a raised potential and the neutral plasma. This then

causes a stream of ions from the plasma to travel towards the sample at a rate which is controlled by the power applied to the table which is completely separate from the power applied to generate the plasma.

ICP etching is a faster process than RIE etching due to the larger ion densities that can be achieved. This makes it particularly important for developments in processing wideband semiconductors, which will be discussed in the next chapter. ICP is also used in experimentation with through wafer etching which has many possible applications for future developments in very small feature size electrical devices.

# Chapter 4

## Development of plasma processes

### 4.1 Introduction

This section will describe plasma processes that were developed during the course of the project. The previous chapter has discussed the different types of reactors and their main uses. The characteristics of the material to be processed determines which type of reactor needs to be used and also the chemistry that is necessary depending on the result required. For etches it is essential to have chemistries that react with the material, producing volatile compounds. On the other hand for a plasma clean such as an oxygen ash it is imperative that the plasma does not interact with the material, only with possible contaminants on the surface.

### 4.2 Plasma etching of SiC

#### 4.2.1 Properties of SiC

SiC is a compound semiconductor which has many possible applications one of which will be discussed further in Chapter 5. Table 4.1 has some of the more important physical and electrical properties of SiC.

Another aspect of the material's properties is that no viable wet etch

Table 4.1: Some important material and electrical properties of SiC

Crystal Structure	Hexagonal
Lattice constant (Å)	a : 3.08 c: 9.92
Atomic number	6/14
Atomic mass	12.01/ 28.08
Density ( $\text{gcm}^{-3}$ )	3.2
Radiation length ( $\text{gcm}^{-2}$ )	28.9
Mobilities ( $\text{cm}^2\text{V}^{-1}\text{s}^{-1}$ ) $\mu_n$ $\mu_p$	e: 900 h: 20
Band gap ( $E_g$ (eV)at 300 K)	3.3
Work function ( $\phi_s$ (eV))	4.85
Electron affinity ( $\chi_m$ (eV))	3.2
Displacement energy averaged value (eV)	Si: 35 C: 20
Dielectric constant	9.7
Electron/hole pair production energy (eV)	8.4
Thermal conductivity (W/cmK)	4.9
Melting point ( $^{\circ}\text{C}$ )	( sublimes ) > 1800

exists. Device processing in this case relies on dry etching using a plasma. Much work has been carried out on SiC to look for a process which combines high etch rate with clean features and low electrical damage [25]-[34].

## 4.2.2 Etch parameters

### Initial Conditions

SiC was etched using  $\text{SF}_6$  and  $\text{O}_2$  in an Inductively Coupled Plasma (ICP) reactor. The ICP reactor was used in this case to produce a high density plasma  $> 10^{11}$  ions/ $\text{cm}^3$  with a controllable D.C. bias to the sample. These are essential to produce a high rate etch process. Standard RIE processes produce etch rates in the range of 10's of nm/min. However, deep etching

requires etch rates at least an order of magnitude higher. Faster etching is also essential to reduce potential damage caused by the dry etch process. Processes were investigated using  $\text{SF}_6$  and  $\text{SF}_6/\text{O}_2$  chemistries. The base conditions used are shown in Table 4.2. Process variations included the

Table 4.2: Constant parameters for the series of etching tests

Gas	- $\text{SF}_6$
Flow rate	- 15 sccm
Etch pressure	- 10 mTorr
Etch temp	- $25^\circ\text{C}$
Time	- 1min

effect of changing the bias powers and the oxygen content. Step heights were measured using a Dektak 3ST surface profiler to allow calculation of the etch rates. The effect of the etch on the electrical properties were found from measurements of the I-V characteristics and calculation of the Schottky barrier height. This will be discussed in the next section.

Two different sets of experiments were carried out. The first used only  $\text{SF}_6$  gas and varied the applied powers. The second series of experiments used constant powers but with the addition of  $\text{O}_2$  to the plasma.

### **Etch rates measured from varying conditions**

The initial series of etch tests used the parameters in Table 4.2 with variations in the applied RF bias and ICP discharge power. Two different mask materials were investigated. Shipley S1818 photoresist, a standard widely used positive photoresist, was patterned using a photolithographic process, as discussed earlier, and hard baked before use. NiCr (nichrome) was also used. A 70 nm thick layer was patterned using the lift-off technique, as

discussed earlier.

The equipment used was an Oxford Plasma Technology System 100 ICP 180 etch tool. This has a 500 W generator for the RF bias power and a 3 kW generator for the ICP discharge. RF bias power was varied over the range 75-400 W and the ICP power was in the 1- 2 kW range. Fig. 4.1 shows

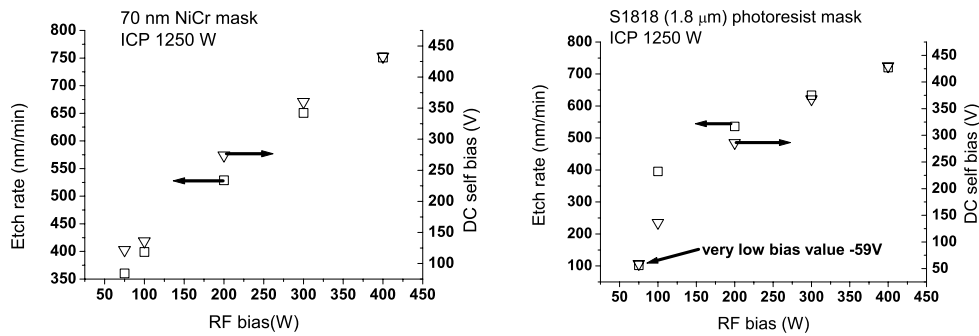


Figure 4.1: Plotted are the etch rates against applied RF bias power for a constant ICP power of 1250 W (left hand axis). The right hand vertical axis shows the DC self bias at the different values of the RF bias power. Etch selectivity for NiCr: SiC was greater than 10 : 1 even for the highest etch rate, while selectivity of photoresist : SiC was approx. 1 : 1.

plots for the etch depth versus applied RF bias for NiCr and photoresist etch masks. The ICP power was kept constant at 1250 W. Also plotted are the DC self bias against the RF bias. The etch depths were measured using a Digital Instruments Nanoscope AFM (atomic force microscope) in contact mode.

Also investigated here was the effect of varying the ICP power with a constant RF power of 200W. Fig. 4.2 shows how the etch rate is affected by these changes in the applied ICP power. It can be observed from this series of figures that increases in either power increases the rate at which the material

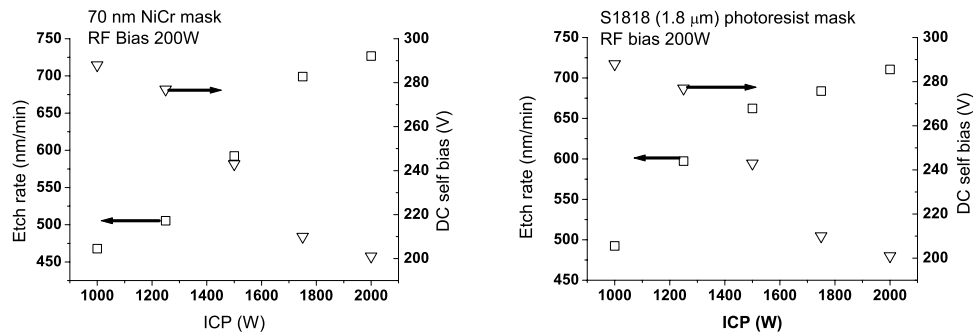


Figure 4.2: Shown are the etch rates against applied ICP power for a constant RF bias power of 200W. The right hand vertical axis shows the DC self bias at the different ICP powers. Etch selectivity for the 70 nm NiCr mask was  $\sim 20 : 1$  even for the highest etch rate.

is removed. This is due to a combination of two factors. For increases in ICP power the plasma generated is denser and with a higher proportion of radicals, allowing greater chemical interaction between the plasma and the substrate. Secondly increasing the RF power changes the d.c. bias of the plasma as can be seen from Fig. 4.1. This increases the incident energy with which ions reach the substrate producing a higher rate of physical sputtering of material. This description is a simplification due to other changes which can take place in the nature of the plasma.

The series of tests was carried out over a very short etch time of 1 minute. Subsequent work has shown that the etch rate for SiC changes due to a build up of surface carbon. This is caused by preferential removal of Si by fluorine ions in the plasma. To overcome this  $O_2$  was added to the chemistry. By the addition of  $O_2$  it was hoped that faster removal of the carbon layers as  $CO_2$  or CO would result. The effect of variations in oxygen concentration is shown in Fig. 4.3. These etches were carried out using a 100nm Ti mask

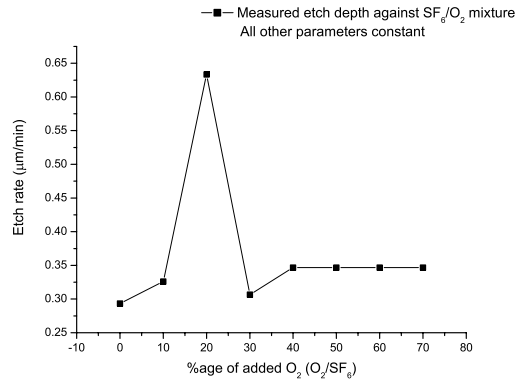


Figure 4.3: Shown is the etch rate obtained for different fractions of O<sub>2</sub> added to the SF<sub>6</sub>.

which was applied using the lift-off process. This series of etches was carried out with an etch time of 15 min. Unfortunately the Ti mask was completely eroded in some cases. To remedy this the etches were repeated using a simple shadow mask.

### 4.2.3 Metal-semiconductor contacts

In order to allow the characterisation of etch damage to the material it is necessary to observe changes in the electrical properties of the material. To observe changes in the semiconductor properties it is necessary to understand how the interface between a metal and a semiconductor develops. It is then possible to compare with the unetched material to quantify the changes.

When metal comes into contact with a semiconductor surface a barrier will be formed. Here I will consider the basic energy band diagrams. This section will also cover the Schottky effect and the dominant current transport processes. The introduction of surface damage or contaminants, e.g. by

etching, can alter the way the barrier is formed and subsequently affect the usefulness of the material. A primary example is lowering of the Schottky barrier height due to surface damage or chemical adsorption during the etching process. This reduces the effectiveness of rectifying contacts produced on the material. This section is in part derived from the metal semiconductor theory that can be found in books such as ‘Semiconductor devices: physics and technology’ and ‘Physics of semiconductor devices’ by S. M. Sze [14, 35] and ‘Metal-semiconductor contacts’ by E. H. Rhoderick [36]

### Energy band relation

For a metal in intimate contact with a semiconductor the Fermi levels in the two materials must be coincident at thermal equilibrium. The limiting cases are shown in Fig. 4.4. At the far left the two materials are not in contact and are not in thermal equilibrium. If a wire is used to connect the two materials so that charge can flow from the semiconductor to the metal and the system is brought into thermal equilibrium, the Fermi levels on both sides line up. The Fermi level in the semiconductor is lowered relative to that in the metal by an amount equal to the difference in the work functions.

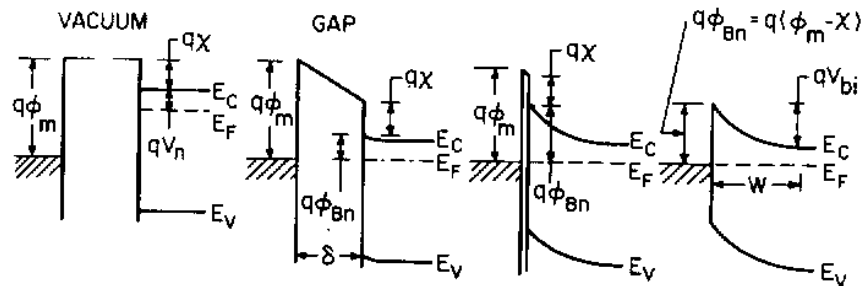


Figure 4.4: The development of the band structure at a metal-semiconductor interface [35].

The work function, denoted by  $q\phi_m$  for the metal, is the difference between the vacuum level and the Fermi level. This is equal to  $q(\chi + V_n)$  in the semiconductor, where  $q\chi$  is the electron affinity measured from the bottom of the conduction band  $E_c$  to the vacuum level and  $qV_n$  is the the difference in energy from  $E_c$  to the Fermi level. The potential difference  $q\phi_m - q(\chi + V_n)$  is called the contact potential. As  $\delta$ , the distance between the metal and the semiconductor decreases an increasing negative charge is built up at the metal surface. Additionally an equal and opposite charge (positive) must exist in the semiconductor. Due to the relatively small carrier concentration the positive charge is built up in a thin barrier layer at the semiconductor surface.

When  $\delta$  is small enough to be transparent to electrons, being equivalent to the interatomic distance, the limiting case as shown to the right of Fig. 4.4 is obtained. In this case  $qV_{bi}$  is the built-in potential at zero bias and  $W$  is the width of the depletion layer. The limiting height of the barrier  $q\phi_{Bn}$  is given by

$$q\phi_{Bn} = q(\phi_m - \chi). \quad (4.1)$$

The barrier height is simply given by the difference between the metal work function and the electron affinity of the semiconductor, for an n-type semiconductor. For a p-type semiconductor the barrier height  $q\phi_{Bp}$  is given by

$$q\phi_{Bp} = E_g - q(\phi_m - \chi). \quad (4.2)$$

For a given semiconductor and any metal the sum of the barrier heights on n- and p-type substrates is equal to the bandgap

$$q(\phi_{Bn} + \phi_{Bp}) = E_g. \quad (4.3)$$

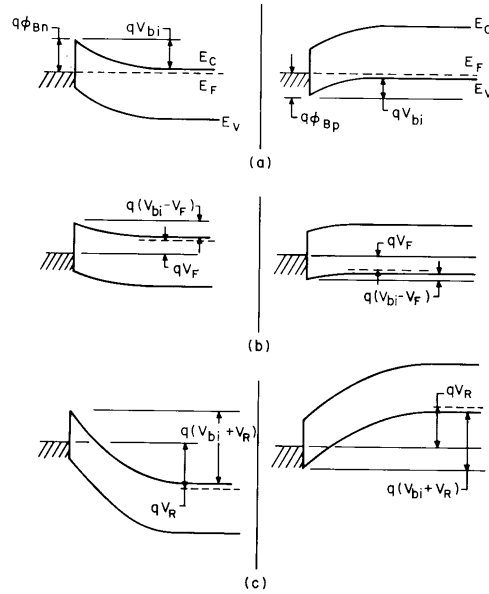


Figure 4.5: Energy band diagrams for n- and p-type material for various bias conditions [14].

Here only the simple single surface state case is considered. For the case of multiple surface states the barrier height may be determined by the surface states rather than the work function.

### Depletion Layer

When the metal/semiconductor interface is completed it is obvious that a definite relation between the conduction and valence bands of the two materials has been established. The variations of the band structure when an external voltage is applied is shown in Fig. 4.5. Assuming a constant doping density such that  $\rho \simeq qN_D$  for  $x \leq W$ , and  $\rho \simeq 0$  and  $dV/dx \simeq 0$  for  $x > W$  we get

$$W \text{ (depletion width)} = \sqrt{\frac{2\epsilon_s}{qN_D}(V_{bi} - V)}, \quad (4.4)$$

where  $W$  is the width of the depletion layer,  $V_{bi}$  is the built in potential and  $V$  is the applied potential.

The capacitance of the depletion region is given by

$$C = \sqrt{\frac{q\epsilon_s N_D}{2(V_{bi} - V)}} = \frac{\epsilon_s}{W}. \quad (4.5)$$

By measuring the capacitance of the depletion region and plotting  $1/C^2$  versus  $V$  the intercept of this line on the x-axis gives  $V_{bi}$ , while the gradient gives  $N_D$ . It is then possible to calculate  $W$  for a given device from Eqn. 4.4. During irradiation it is possible that changes in the doping concentration or damage to the crystal structure could cause changes to the depletion width etc. This is a further method to observe the effects of damage in the material.

### Schottky effect

The Schottky effect is the image force lowering of the potential energy for charge carrier emission when an electric field is applied. First we will consider the metal-vacuum case. For a metal in a vacuum the least amount of energy necessary to liberate an electron, with initial energy at the Fermi level, is defined as  $q\phi_m$ , the work function of the metal, as shown in Fig. 4.6.

An electron at a distance  $x$  from the metal surface will induce a positive charge on the metal surface. The attractive force between the two is equivalent to the force that would exist between the electron and a positive charge at distance  $-x$  in the metal. The positive charge is referred to as the image charge and the attractive force is the image force given by

$$F = \frac{-q}{4\pi(2x)^2\epsilon_0} = \frac{-q}{16\pi\epsilon_0 x^2} \quad (4.6)$$

where  $\epsilon_0$  is the permittivity of free space. The energy of an electron travelling

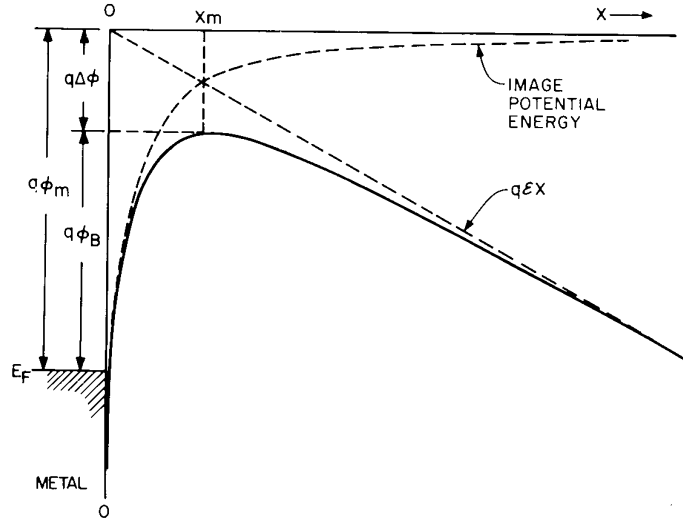


Figure 4.6: Energy band diagram for a metal-vacuum interface, the lowering is due to a combination of the electric field and the image force [35].

from point  $x$  to the surface of the metal is given by

$$E(x) = \int_{\infty}^x F dx = \frac{q}{16\pi\epsilon_0 x^2}. \quad (4.7)$$

This corresponds to the potential energy of an electron at a distance  $x$  from the metal surface, shown in Fig. 4.6, measured down from the  $x$  axis.

By applying an external field  $\mathcal{E}$  the total potential energy, PE, is a function of the distance,

$$PE(x) = \frac{q^2}{16\pi\epsilon_0 x} + q\mathcal{E}x. \quad (4.8)$$

The Schottky barrier lowering  $\Delta\phi$  and the location  $x_m$  are given by the condition  $d[PE(x)]/dx = 0$ . For a semiconductor/vacuum system  $\epsilon_0$ , the permittivity of free space, is replaced by  $\epsilon_s$ , the permittivity of the semiconductor. This gives

$$\Delta\phi = \sqrt{\frac{q\mathcal{E}}{4\pi\epsilon_s}}. \quad (4.9)$$

The location and magnitude of the modified barrier can be seen in Fig. 4.7

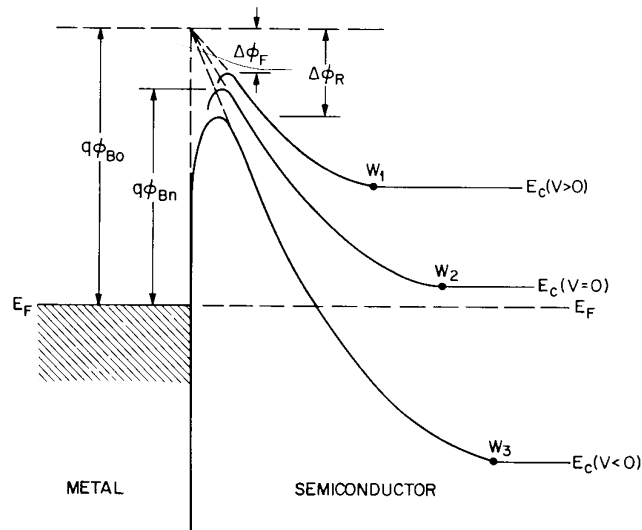


Figure 4.7: Energy band diagram for a metal-vacuum interface, showing the Schottky effect for n-type semiconductors.  $q\phi_{Bo}$  is the intrinsic barrier height,  $q\phi_{Bn}$  is at thermal equilibrium [35].

### Current transport

Here I will discuss the major current transport process within the Schottky barrier diode. This is described using the thermionic emission-diffusion current proposed by Crowell and Sze [35]. This combines the Thermionic emission theory derived by Bloch and the Diffusion theory proposed by Schottky. This approach is derived from the existence of  $v_R$  the thermionic recombination velocity at the semiconductor/metal interface.

The electron potential energy  $q\psi(x)$  is considered versus distance incorporating the Schottky effect, as shown in Fig. 4.8 for a metal semiconductor barrier. The diffusion of carriers is strongly affected by the potential configuration of the region through which it is diffusing. Assuming that the barrier height is large enough that the charge density between the surface and  $x = W$  is essentially that of the ionised donors,  $W$  is the edge of the depletion re-

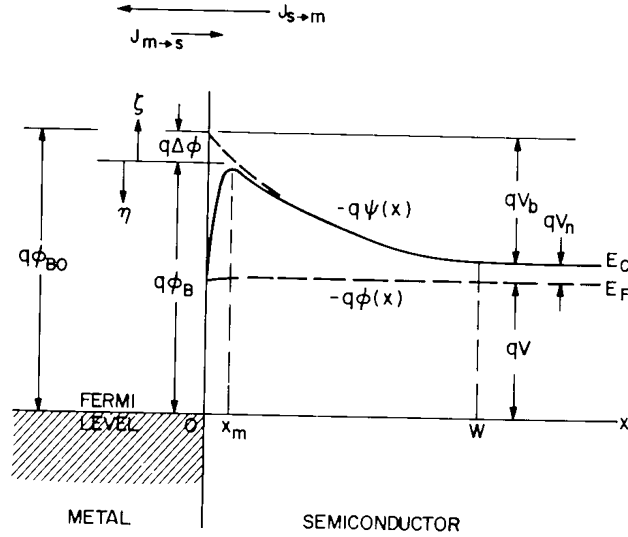


Figure 4.8: Energy band diagram for a metal/vacuum interface, showing the Schottky effect for n-type semiconductors.  $q\phi_{BO}$  is the intrinsic barrier height,  $q\phi_{Bn}$  is at thermal equilibrium [35].

gion. The rounding at the top of the curve is caused by a combination of the electric field associated with the ionized carriers and the attractive potential exerted on electrons as they approach the metal surface. The full expression for current transport by the thermionic emission-diffusion theory is given by

$$J = J_s \left( \exp\left(\frac{qV}{kT}\right) - 1 \right), \quad (4.10)$$

$$J_s = A^{**} T^2 \exp\left(-\frac{q\phi_{Bn}}{kT}\right), \quad (4.11)$$

where  $J$  is the current density ( $\text{Acm}^{-2}$ ),  $J_s$  is the saturation current density,  $A^{**}$  is the effective Richardson constant,  $T$  is the temperature,  $k$  is Boltzmann's constant,  $\phi_{Bn}$  is the barrier height, and  $V$  is the applied bias voltage. From this by the measurement of current voltage characteristics it

was possible to calculate the barrier height from

$$\phi_{Bn} = \frac{kT}{q} \ln\left(\frac{J_s}{A^{**}T^2}\right). \quad (4.12)$$

$J_s$  is the current density extrapolated back to zero.

By measurement of current voltage characteristics and calculation of barrier heights it was possible to observe the effects of irradiation of the materials.

#### 4.2.4 SiC I-V characterisation

In order to carry out current/voltage measurements a series of metallic contacts were deposited on to the SiC substrate. A full face ohmic back contact was applied consisting of 100 nm of Ni which was deposited using a Plassys electron beam evaporator. The ohmic contacts were formed in an N<sub>2</sub> ambient at 1000° C for 30s in a Jetfirst RTA (rapid thermal annealer).

##### **I-V changes after RIE exposure**

RIE of SiC although not a process suitable for etching of deep features i.e. isolation etches or mesa etching etc., is a valid method for looking at surface damage. A number of pieces of n-type 4-H SiC were exposed to a plasma of SF<sub>6</sub> for 5 minutes at varying RF powers. The parameters are given in Table 4.3. To produce the Schottky barrier a contact of 100 nm Ti and 50 nm Au was evaporated onto the front side of the substrate. This was patterned using lift-off to produce circular pad diodes with a single guard ring in diameters of 250, 500, and 750 μm. The I-V measurements were taken using a manual probe station connected to an HP test fixture. This apparatus only has a low voltage threshold. Currents were measured over a range of voltages with comparison plots at -1 V being used to observe changes in the current. The

Table 4.3: Parameters for SF<sub>6</sub> RIE surface treatment of SiC

Gas	SF <sub>6</sub>
Flow rates (sccm)	18
Etch pressure (mTorr)	10
RF power (W)	50- 250
Etch time (min)	5
Etch rate (nm/min)	< 10

low voltage measurements were then used to calculate changes in Schottky barrier height using Eqn. 4.12. Fig. 4.9 has plots of the variation in leakage current and the Schottky barrier height.

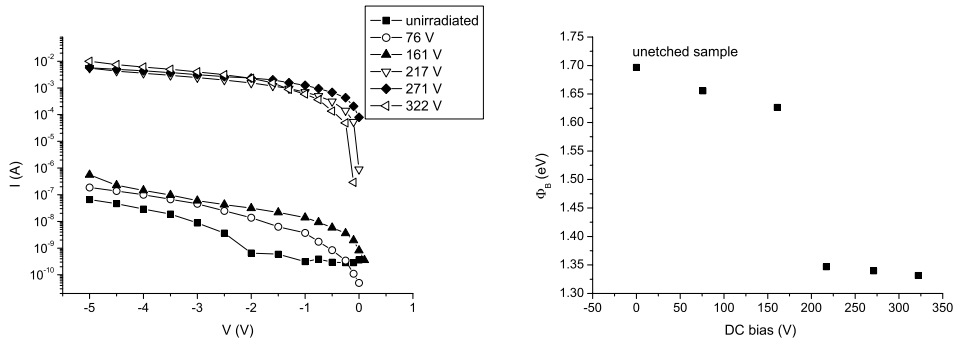


Figure 4.9: *left* Leakage current and *right* Schottky barrier height as a function of incident ion energy in RIE discharge.

The measurements show that the changes in surface properties that are necessary to affect the leakage current and barrier height are very low. Significant change is observed at 100W RF power or -161 V bias, which equates to an average energy of  $\sim 160$  eV per incident ion. The change in leakage current at the highest bias value, 322 V, shows an increase of several orders of magnitude. This suggests that surface damage is a major factor in the behaviour of currents and Schottky barrier height for fabricated devices. In-

creasing the dc bias of the discharge gives each ion in the discharge more energy when it reaches the surface of the sample. A number of things then happen; material is removed by chemical processes, this is the most desirable event; material is removed by physical sputtering, this is less desirable; and finally the ion is adsorbed into the semiconductor surface, this is bad. The last two of these can introduce lattice damage into the surface layers of the semiconductor, adsorption can also introduce a number of electrically active defects into the material. Increasing the dc bias gives incident ions more energy when they reach the surface of the semiconductor which can increase the severity and depth of lattice damage. The increased energy can also allow ions which are adsorbed to travel deeper into the material, again this increases the depth of damage in the semiconductor surface. These two processes have an effect on the formation of a Schottky barrier because it is dependent on the properties of the semiconductor and the quality of the contact between the metal and the semiconductor any variation can have a large effect as has been seen. In the limit of surface damage the barrier height can be limited by the surface states rather than the relation in Eqn. 4.1 [14, 35].

### **I-V changes after ICP exposure**

As discussed earlier in this chapter variations in  $O_2$  concentration were investigated to observe the effects on the etch rate during ICP etching. A number of pieces of 6H-SiC were exposed to an  $SF_6/O_2$  etch in an ICP reactor. These were then electrically characterised to observe if the  $O_2$  in the plasma caused any additional variations in the leakage current and Schottly barrier height. The parameters for the etches are given in Table 4.4

After etching, current voltage measurements were made using a manual

Table 4.4: Parameters for SF<sub>6</sub>/O<sub>2</sub> ICP etching of SiC

Gas	SF <sub>6</sub> / O <sub>2</sub>
Flow rates (sccm)	(SF <sub>6</sub> ) 15 (O <sub>2</sub> ) 0- 9
Etch pressure (mTorr)	10
ICP power (W)	1500
Platen power (W)	200
Etch time (min)	15

probe station connected to a Keithley 237 electrometer controlled by Labview software. The changes in the reverse current are shown in Fig. 4.10.

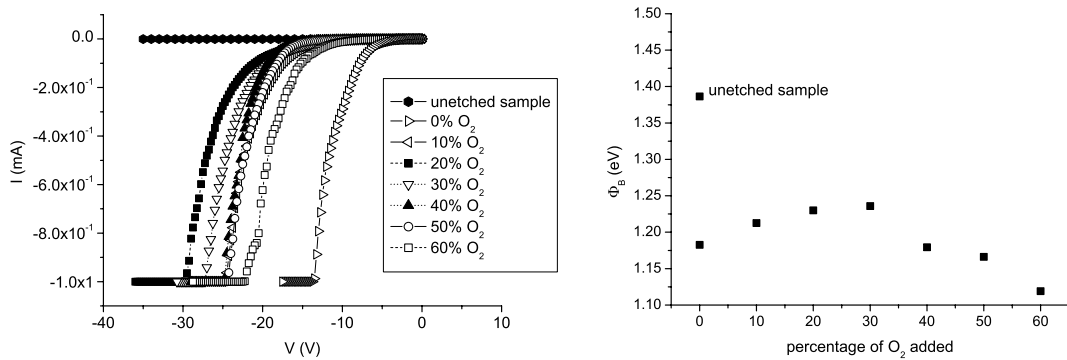


Figure 4.10: *left* Leakage current and *right* Schottky barrier height as a function of O<sub>2</sub> content in ICP plasma.

The changes in the leakage current and the barrier height show that the addition of small amounts of O<sub>2</sub> has a beneficial effect on the reverse current, Schottky barrier height, as well as the etch rate shown earlier in this chapter. There are a number possible reasons for this. The first, and easiest to observe, is that the vastly increased etch rate has left a relatively undamaged surface. This can be supported by the comparison between the highest breakdown voltage and highest etch rate for 20 % added O<sub>2</sub>. However, after this the breakdown voltage decreases again. The final measurement at 60 % added

O<sub>2</sub> is the worst measured after the pure SF<sub>6</sub>. Other possibilities include the adsorption of O<sub>2</sub> into the surface, changing the surface properties. Changes in the Schottky barrier height do not exactly match those observed in the reverse currents; the changes in barrier height lag behind the changes in the current. This could indicate some chemical change in the material.

#### **4.2.5 Etch damage comparison**

Comparison between the damage caused by RIE and ICP exposure do not follow the expected trend. The changes in leakage current and barrier height are much more severe for RIE than ICP contrary to what would be expected from observations of the nature of the plasmas. An ICP discharge produces a plasma which is at least an order of magnitude denser than that produced in an RIE discharge. However, as shown, the changes in leakage are much more severe for the RIE discharge. This can be explained in terms of the etch rate. The ICP has an etch rate which is greater than 10 times that of the RIE. This means that a cleaner surface is left behind on which to form contacts. This is also borne out by the measured changes with the variation in added O<sub>2</sub>. Here as the etch rate increases so the breakdown voltage increases.

Comparisons between the changes in the Schottky barrier height are not so straight forward. The RIE discharge had an increasing RF power, and dc bias. This leads to more energetic bombardment causing more damage to the surface. The changes in the ICP plasma were more complex, being chemical in nature. The addition of O<sub>2</sub> changes the surface chemistry of the sample during etching. The changes caused by increasing the dc bias are straightforward. Increasing the bias decreases the breakdown voltage and the Schottky barrier height. This tells us that the surface roughness is affected

and consequently the metal for the Schottky barrier contacts do not make a perfect interface. However, the changes in the barrier height measured from the ICP samples lag behind the leakage current. This can be caused by a changing of the surface properties. The sample with the highest breakdown voltage does not have the highest Schottky barrier. This implies a change in the sample resistivity rather than in the formation of the Schottky barrier. Additionally the way in which the barrier height changes gives an indication of the changing surface properties.

## **4.3 Plasma etching of ITO**

### **4.3.1 Introduction**

Indium tin oxide (ITO) is a transparent conductive semiconductor. ITO is used to provide a transparent electrode for optoelectronic devices where a more common metal contact would not be suitable. The most popular use for this material is in the production of screens for laptop computers. It is commonly used in a range of other applications such as gas sensors, anti-reflection coatings and solar cells [37, 38]. However, its use for pixelated photodiodes is also in development [39]. It is possible to pattern ITO for these various applications in a variety of ways from lift-off to wet and dry etching. In Chapter 6, I will discuss the application of plasma technology to ITO for the specific application of creating microelectrode arrays using RIE (reactive ion etching) and PECVD (plasma enhanced chemical vapour deposition) as discussed in Chapter 3.

### 4.3.2 Etch parameters for ITO

Etching of ITO can be achieved with a great deal of success in a number of ways. These include wet [40] and dry [40]-[44] etching. The problems associated with the isotropic nature of wet etching makes it unsuitable for a highly reproducible process which is required to produce dense features. We have experimented with using a mixture of methane and hydrogen ( $\text{CH}_4/\text{H}_2$ ) in an ElectroTech 340 RIE etch tool. The etch parameters for the process are shown in Table 4.5.

Table 4.5: Etch parameters for  $\text{CH}_4/\text{H}_2$  etching of ITO

Gases	$\text{CH}_4/\text{H}_2$
Flow rates (sccm)	5:25
Etch pressure (mTorr)	11
RF power (W)	100
Temperature (C)	25
Etch rate (nm/min)	25

This produces good anisotropic etching. Slight polymer build up can discolour glass but this is removable. The use of  $\text{CH}_4/\text{H}_2$  to etch ITO produces certain problems when attempting to find a mask material. Other etch processes which were tested have a simpler masking technology including  $\text{SF}_6$ ,  $\text{SiCl}_4$  and  $\text{CHF}_3$ . However, there was no measurable etching of ITO using any of these processes when used at room temperature, so a new masking technique was required to etch using  $\text{CH}_4/\text{H}_2$ .

### 4.3.3 Masking properties

The use of a simple photoresist mask was very desirable to minimise the number of fabrication steps. Photoresist is normally hard baked before use as

an etch mask, the hard baking normally being done at 120°C for 30 min. This removes all remaining solvent and toughens the resist to enable it to better stand up to the plasma. The hydrocarbon nature of a CH<sub>4</sub>/H<sub>2</sub> plasma means that in many cases a fully hardened photoresist mask is not suitable. This is because the high temperatures and volatile chemistry can cause cross-linking of the resist making mask removal difficult without the use of caustic cleaning processes. The most common of these is Nanostrip, a mixture of sulphuric acid and hydrogen peroxide. This also damages the ITO so is unsuitable for use. Common solvents such as acetone do not suffice to remove the hardened photoresist.

The layer of ITO used is  $\sim 300$  nm thick. This only requires a relatively short etch time of 12 min. An investigation into reducing the time of the resist hard bake was carried out to discover whether it was possible to use the resist as a mask or if an intermediate metal or dielectric layer was necessary. The latter would add an extra step to the process so increasing the complexity and hence the number of potential problems. A number of samples were prepared using S1818 photoresist. A wire pattern was exposed onto each sample. These were then post baked at 120°C for varying lengths of time. The samples were etched and various methods for cleaning the surface were tried.

Table 4.6 details the cleaning processes that were used to remove the photoresist mask after an ITO etch. The etch time for these tests was 14 min. This includes a 2 min overetch of the material to allow for variations in the thickness of the ITO layer. A 5 min post bake was found to be optimal. The resist was suitable for use as a mask and could be removed without the use of any caustic agents.

Table 4.6: Solvent cleaning processes tried for various photoresist post bake times for etching of ITO using CH<sub>4</sub>/H<sub>2</sub>

Post bake time	Cleaning process	Effect
5 min	Acetone (cold)	very little
	Acetone (hot)	some removal near edge of pattern
	Acetone (hot) in ultrasonic bath	removed almost all traces of resist
	Acetone (hot) in ultrasonic bath used cotton bud after	all resist gone
10 min	Acetone (cold)	none
	Acetone (hot)	very little
	Acetone (hot) in ultrasonic bath	some removal near edge of pattern
	Acetone (hot) in ultrasonic bath used cotton bud after	no removal in centre of pattern
15 min	Acetone (cold)	none
	Acetone (hot)	very little
	Acetone (hot) in ultrasonic bath	very little
	Acetone (hot) in ultrasonic bath used cotton bud after	very little

#### 4.3.4 I-V characterisation of etched ITO

Part of the problem of developing the mask technology for ITO etching was to ensure that there was no electrical degradation of the ITO layer. The Van der Pauw method [45] was used to measure the resistivity of the ITO layers before etching was carried out. This was then repeated after etching. The Van der Pauw method uses four probes placed onto the surface of the material in a square. It works by passing current,  $I$ , through the sample between one neighbouring pair of contacts and measuring the voltage,  $V$ , induced in the material with the other pair such that,

$$R_s = \frac{V}{I} \times 4.54. \quad (4.13)$$

Eqn. 4.13 uses Ohms law with a correction factor of 4.54 to measure the resistivity in units of  $\Omega/\square$ . This correction factor is applied in the case when the layer thickness  $W \ll d$ , the sample diameter or in this case the side length. The other condition for this relation to work is that  $d \ll s$  the probe spacing. The measured resistivity was  $11 \Omega/\square$ .

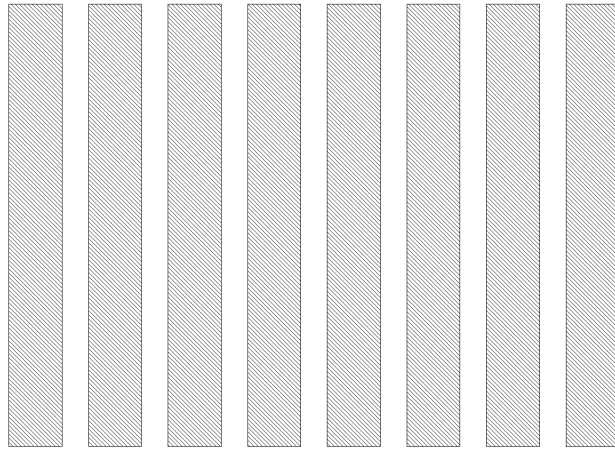


Figure 4.11: Wires similar to those etched into the ITO layer,  $600 \mu\text{m}$  by several mm.

A number of wires,  $600 \mu\text{m}$  wide and several mm long such as those shown in Fig 4.11, were then etched in the ITO layer. After etching in  $\text{CH}_4/\text{H}_2$  with an etch rate of  $\sim 25 \text{ nm}/\text{min}$  the resistivity was found to be essentially unchanged allowing for slight variations in the layer thickness. Fig. 4.12 shows a series of I-V measurements for post etch material i.e. ITO under the photoresist mask. It shows conductance on the wires and zero current in the spaces between, and also between adjacent wires. The zero current between adjacent wires means that the etch has been completely successful in removing all of the un-masked material which is essential for any application.

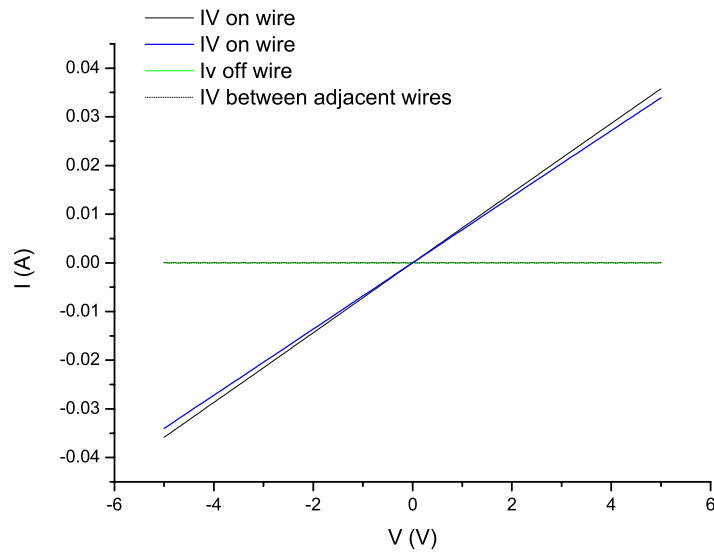


Figure 4.12: I-V characterisation for  $\text{CH}_4/\text{H}_2$  etched ITO plates.

#### 4.3.5 Etching of ITO using resist/Ti mask

The use of electron beam resist to pattern the ITO layer results in the use of a different masking structure. A two layer mask is used consisting of 100 nm of Ti which is in turn patterned using a layer of UVIII e-beam resist. The ITO is etched using  $\text{CH}_4/\text{H}_2$  RIE with the same parameters as previously discussed. However it is now essential to remove the layer of Ti from the surface of the ITO. This has to be achieved using a dry etch process as the wet etch for Ti is a strong  $\text{HCl}/\text{H}_2\text{O}$  solution. This is also the wet etch for ITO but ITO etches at a much higher rate causing problems with under etching of any narrow features. Ti can be etched by RIE using  $\text{SiCl}_4$ ,  $\text{SF}_6$  and a number of other fluorine containing gases. However  $\text{SF}_6$  has the fastest etch rate of these,  $\sim 25$  nm/min, with a very short induction time. This process uses a low pressure  $\text{SF}_6$  plasma in a BP 80 RIE reactor; the parameters are given in

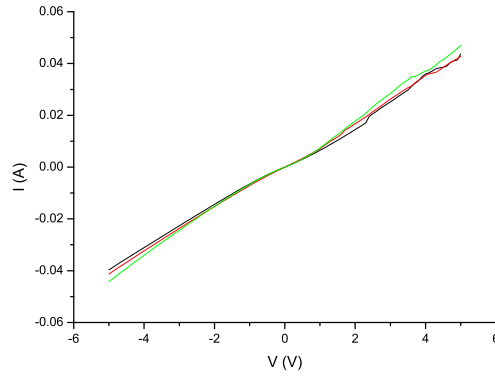


Figure 4.13: I-V characterisation for ITO plates after  $\text{SF}_6$  cleaning of UVIII/Ti mask structure.

Table 4.7. It has already been mentioned that  $\text{SF}_6$  does not etch ITO but it becomes essential that it does not damage the surface by either roughening it or by chemical adsorption. Either of these could affect the conductivity and so reduce the usefulness of any devices fabricated. Fig. 4.13 shows measurements of I-V for an ITO plate before and after the  $\text{SF}_6$  etch. It is clear that the conductivity is essentially unaffected by the exposure.

Table 4.7: Etch parameters for  $\text{SF}_6$  plasma clean of ITO substrate.

Gas	$\text{SF}_6$
Flow rate (sccm)	10
Etch pressure (mTorr)	13
RF power (W)	100
Etch rate (nm/min)	>25

The I-V curves are shown for measurements on three different wires after  $\text{SF}_6$  plasma removal of the Ti masking layer. These curves show very little change in the properties of the material after the etch compared to the pre-

etch measurements shown in Fig. 4.12.

## 4.4 Plasma deposition of $\text{Si}_3\text{N}_4$

### 4.4.1 Etching deposited $\text{Si}_3\text{N}_4$ layers

In the production of electrical and photoelectric devices on ITO and SiC, as with many other semiconductor materials, a surface passivation layer may be added. This is used to protect the device from damage and atmospheric contamination. One of the more common dielectric materials used for surface passivation is  $\text{Si}_3\text{N}_4$ , which is deposited using PECVD (plasma enhanced chemical vapour deposition). Once the passivation layer is deposited it is usually necessary to produce openings in the layer to allow electrical contact. This is done using an  $\text{SF}_6$  plasma in an Oxford Plasma Technology System 100 RIE etch tool. For this etch it is essential to be able to etch through the  $\text{Si}_3\text{N}_4$  layer to the ITO without damaging the conductive surface. The process to achieve this is detailed in Table 4.8.

Table 4.8: Process parameters for  $\text{SF}_6$  etching of  $\text{Si}_3\text{N}_4$

Gas	$\text{SF}_6$
Flow rates (sccm)	10
Etch pressure (mTorr)	2-3(open valve)
RF power (W)	120
Etch rate (nm/min)	$\sim 85$

This etch process gives easily reproducible, well defined features. It is possible to use a single stage photoresist mask without any post bake making it easy to remove.

Problems with the  $\text{Si}_3\text{N}_4$  revolve around getting a film which has no micro-

pores or pinholes. Additional problems were encountered with poor adhesion of the films during subsequent processing. This can cause areas of the  $\text{Si}_3\text{N}_4$  to peel from the surface. The cause of problems with the layers are attributed to dust or other contamination of the surface to be coated. Solvent cleaning is not sufficient to ensure a uniform film without pinholes or micropores and with good adhesion, so other methods were investigated to improve the quality of the passivation layers.

#### 4.4.2 Reduction of pinhole density and adhesion promotion

In order to ensure that the surface was as clean as possible a rigorous solvent clean was applied to each sample before the deposition of the  $\text{Si}_3\text{N}_4$  layer. This involves sequential cleans with acetone, IPA, methanol and RO (reverse osmosis) water. To improve the surface adhesion the deposition process for the  $\text{Si}_3\text{N}_4$  was changed to produce a hydrogenated  $\text{Si}_3\text{N}_4$  layer. The reason for this is to reduce the internal stress in the film. Reduction in film stress helps to reduce the possibility of films lifting off or cracking. This initial step was not successful in reducing pinhole/micropore density, however, film adhesion was greatly enhanced with no peeling or lifting of films. An oxygen plasma ash surface treatment was introduced to combat this. This uses an ElectroTech Barrel asher to produce a high pressure oxygen plasma. The parameters are given below in Table 4.9. The main purpose for this piece of equipment is the removal of organic material. This includes any residue that solvent cleans may leave behind.

To characterise the pinhole density a number of samples were ashed for varying lengths of time, 10, 20, and 30 min. A layer of  $\text{Si}_3\text{N}_4$  was then

Table 4.9: Process parameters for oxygen plasma surface treatment

Flow (l/min)	2
Pressure (mTorr)	130
Power (W)	110

deposited on half of the sample. A wire was attached with silver dag and the sample immersed in a saline solution which contained a second earthed electrode. A current of  $80 \mu\text{A}$  was passed through the ITO for 5 min and the number of pinholes etc. visible was counted across the surface. The number of pinholes was vastly reduced with increased ash time and film adhesion was improved with reduced apparent curling at the edges of the film, as evident from Table 4.10.

Table 4.10: Table shows change in density of defects in  $\text{Si}_3\text{N}_4$  layer for different ash times.

Ash time (min)	Hole density ( $\text{cm}^{-2}$ )
10	2.5
20	1.2
30	0.6

The pinhole density was greatly reduced but there were still some visible. To ensure that no pinholes were present in the passivation layer a bi-layer of  $\text{Si}_3\text{N}_4$  was tested. Two 500 nm thick layers of  $\text{Si}_3\text{N}_4$  were deposited sequentially. Oxygen plasma cleans were used on both the ITO surface and the surface of the initial  $\text{Si}_3\text{N}_4$  layer.  $\text{O}_2$  plasma cleans were used to ensure that no surface contaminants i.e. solvent residues remained on the surfaces. There were no visible pinholes when the bi-layer passivation was used. The use of the oxygen ash and a  $\text{Si}_3\text{N}_4$  bi-layer has now become part of the standard

process for device fabrication.

## 4.5 Plasma etching of Ti

Mention has been made of using electron beam lithography to pattern the ITO plate. As previously discussed in Chapter 2 electron beam lithography uses a computer controlled focussed beam of electrons to write patterns into a resist compound. To focus on the sample surface the e-beam machine uses reflectometry. Once the height of the sample surface is known the electron beam can then be focussed to write the pattern. However, both ITO and the quartz substrate are optically transparent. This means that on many occasions it is impossible for the software to find the sample surface and thus the beam is improperly focussed. The improper focussing leads to a problem with stitching sections of the pattern together. To get around this, a layer of Ti is deposited on the surface. This allows the surface to be easily located. The additional Ti layer as discussed earlier in this Chapter can also then be used to pattern the ITO as the UVIII resist used is not thick enough to survive the  $\text{CH}_4/\text{H}_2$  ITO etch.

Table 4.11: Etch parameters for  $\text{SiCl}_4$  etching of Ti

Gas	$\text{SiCl}_4$
Flow rates (sccm)	18
Etch pressure (mTorr)	9
RF power (W)	250
Etch rate (nm/min)	$\sim 25$

A 100 nm thick layer of Ti is evaporated onto the sample surface before the resist is spun on. After the pattern has been written and developed the

Ti is etched using a  $\text{SiCl}_4$  plasma in an Oxford Plasma Technology System 100 RIE etch tool. A number of other chemistries are available to etch Ti. However most of them are very damaging to resist e.g. the  $\text{SF}_6$  etch, which was discussed earlier in this chapter. The etch parameters are given in Table 4.11. This is a common etch process which is highly reproducible, ensuring consistency for consecutive samples.

# Chapter 5

## SiC radiation detectors

### 5.1 Introduction

In this section I will discuss the fabrication and testing of silicon carbide radiation detectors. The plasma processes developed in Chapter 4 are essential in the fabrication of the devices which are tested here. Semiconductor detectors are used in most of the larger particle physics experiments throughout the world e.g. CERN and Fermilab, as inner tracking detectors. This means that they suffer very high doses of radiation. Long term exposure to these very high doses can lead to significant degradation in the performance of the devices. Eventually they have to be replaced usually at great expense. The use of potentially very radiation hard materials, for example SiC, is being investigated to try to extend the lifetime of the detectors possibly by several years. This would lead to a great financial saving.

Other applications would lie in areas where traditional Si semiconductor detectors do not function well, e.g. at high temperatures or in caustic environments. Here I will discuss the mechanisms for detection of ionising radiation in a semiconductor detector, and how this is converted to an understandable output which can be used to identify unknown radiation sources.

## 5.2 Detector fabrication

### 5.2.1 Diode design

The pattern layout design package called Wavemaker (Wam) was used to produce the design for these tests. The pattern to be written by electron beam lithography to produce a photolithography mask had a series of pad diodes with a single guard ring in a range of sizes 250, 500, and 750  $\mu\text{m}$  diameter, as shown in Fig. 5.1. The pad sizes were kept small to reduce the likelihood of fabricating on a micropipe. Micropipes are defects within the material that can cause catastrophic failure of the diode. More will be said about these later.

The guard ring was included in the design to ensure good field uniformity through the diode. Another reason for the inclusion of a guard ring is surface leakage current. Surface leakage current is caused by a large potential drop between the edge of the Schottky barrier and the side edge of the sample. Including a guard ring (or rings as more than one may be used depending on the application) in the diode design reduces the surface leakage. This is because when the same bias is applied to the Schottky pad and guard ring(s) there is no surface potential drop due to the zero electric fields between them. The potential drop is between the guard ring and the edge of the sample and current is not measured from the guard ring. For multiple guard ring schemes the inner ring is sometimes maintained at the same bias as the Schottky pad, successive rings are biased at regularly decreasing values, or left floating, to produce a soft drop towards the edge.

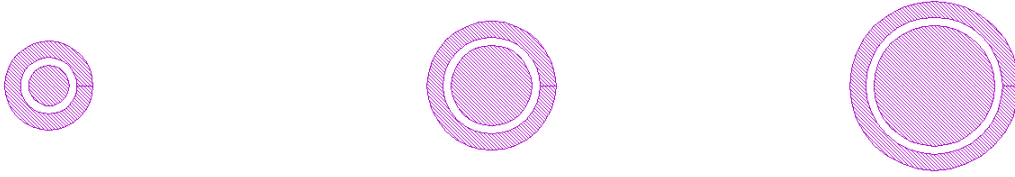


Figure 5.1: Mask design for SiC test samples.

### 5.2.2 Diode fabrication

To produce the detectors to be tested in this section a number of fabrication steps discussed already were used. A full thickness wafer of 4-H semi-insulating (S.I.) SiC was chemically/ mechanically thinned in-house to 100  $\mu\text{m}$  using a Logitech PM4 precision lapping and polishing tool. The thinned material was then cleaned consecutively in Opticlear, a degreasing agent, and then in multiple solvents acetone/ isopropanol/ methanol before a final rinse in RO (reverse osmosis) water.

After solvent cleaning the samples had a further acid clean to remove surface oxide. The  $\text{SiO}_2$  produced on the surface of SiC is not as dense as that of Si due to the presence of C. However it is still enough to create an MIS diode (metal-insulator-semiconductor) not a Schottky barrier. Full face ohmic back contacts of 100 nm Ti were then evaporated onto the back surface using the Plassys electron beam evaporator, as described in Chapter 2. Photolithography was used to define the active areas of the devices on the front face. Schottky contacts of 100 nm Ni were evaporated and patterned using lift off. Both sets of contacts were left un-annealed.

The sample surface was then coated with a 200 nm thick passivation layer of PECVD hydrogenated  $\text{Si}_3\text{N}_4$  as described in Chapter 3. The  $\text{Si}_3\text{N}_4$  layer was applied for a number of reasons. The first was to cut down surface

leakage currents which can reduce the electric field strength within the device and also mask out the signal from the detector if sufficiently large. The other main reason for the inclusion of the passivation layer was related to the effect of humidity upon the I-V characteristics of the devices. This will be discussed later in this chapter. Windows were etched in the passivation layer using an SF<sub>6</sub> RIE process as described earlier, see Table 4.8. Samples to be tested were then attached to PCB holders and the contacts wire bonded out to copper tracks for ease of soldering into test fixtures.

## 5.3 Detector theory

This section will discuss how different types of radiation interact with semiconductor materials. The method for energy calibration and measurement of CCE (charge collection efficiency) will be shown for different semiconductors. Much of the information in this section may be found in a much expanded form in 'Radiation detection and measurement' by Glenn F. Knoll [46]

The simplest explanation for the function of a radiation detector is that radiation of some type interacts with the detector in a particular way to produce an amount of charge which is proportional to the incident energy. This is then collected in some fashion and transferred to readout electronics.

### 5.3.1 Ionising radiation interactions

Ionising radiation is a term used to refer to any type of radiation which causes the generation of electron-hole pairs (e-h pairs) within the body of the detector. The four main types of radiations that are of interest are given in Table 5.1. The charged particles in the left hand column interact in a continuous manner upon entering a medium due to Coulomb forces. This

Table 5.1: Breakdown of four main categories of ionising radiation

<b>Charged radiation</b>		<b>Uncharged radiation</b>
Heavy charged particles characteristic distance $10^{-5}\text{m}$	$\Leftarrow$	Neutrons characteristic distance $10^{-1}\text{m}$
Fast electrons characteristic distance $10^{-3}\text{m}$	$\Leftarrow$	X- and gamma-rays characteristic distance $10^{-1}\text{m}$

produces a characteristic energy deposition curve called the Bragg curve. The uncharged particles on the right do not interact unless they undergo a ‘catastrophic’ event, i.e. a collision. Collisions can be with either a nucleus or with an electron. The arrows in the table show the results for the latter catastrophic events, so that neutron collisions produce heavy charged particles which are then detected, and X- and gamma-rays produce fast electrons.

### Heavy charged particle interactions

Heavy charged particles such as the alpha particle interact within absorbing detector media due to Coulomb interactions between their positive charge and the negative charge of the orbital electrons. Other interactions such as Rutherford scattering do occur but are not significant in detector response.

Upon entering the detector medium every incident particle instantly interacts with a great number of electrons simultaneously. These electrons can react in two ways depending on the proximity of the charged particle. The first is an *excitation* in which the shell electron is raised to a higher shell. The other is an *ionisation*, in which the electron is removed completely from the atom. Due to this constant interaction the velocity of the particle is constantly reduced until the atom is stopped. The rate of energy loss, known more properly as the *linear stopping power*  $S$  or the *specific energy loss*, is

written as

$$S = -\frac{dE}{dx} \quad (5.1)$$

For particles of a given charge state and velocity the energy loss is given by the Bethe-Bloch formula [47],

$$-\frac{dE}{dx} = \frac{4\pi e^4 z^2}{m_0 v^2} NB \quad (5.2)$$

where

$$B = Z \left[ \ln \frac{2m_0 v^2}{I} - \ln \left( 1 - \frac{v^2}{c^2} \right) - \frac{v^2}{c^2} \right].$$

Here  $v$  and  $ze$  are the velocity and charge of the incident particle,  $N$  and  $Z$  are the number density and atomic number of the absorber atoms,  $m_0$  is the electron rest mass, and  $e$  is the charge on an electron.  $I$  represents the average excitation potential and is experimentally determined for each element. For non-relativistic particles only the first term in  $B$  is significant. Thus for a given charged particle the rate  $dE/dx$  varies with  $1/v^2$ . The difference between different absorbers depends primarily on the product  $NZ$ , which represents the electron density of the absorber, and hence the number of electrons which are available to interact with the incident particle.

The specific rate  $-dE/dx$  for a given charged particle in a given absorber produces the Bragg curve shown in Fig 5.2 for a 5.48 MeV  $\text{Am}^{241}$   $\alpha$  particle in SiC. The range was calculated using the SRIM package [48].

Fig 5.2 shows that all of the energy for a 5.48 MeV  $\text{Am}^{241}$   $\alpha$  particle is deposited in  $\sim 18 \mu\text{m}$  of SiC. The depth of penetration is important for the next section, energy calibration, to allow calculation of the amount of energy which has been deposited in a detector by the incident particle. For

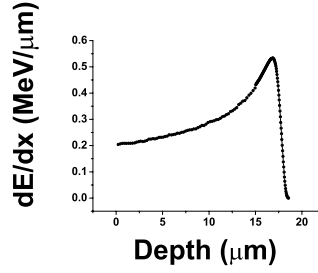


Figure 5.2: The energy deposition Bragg curve for a 5.48 MeV  $\alpha$  particle in SiC.

4-H SiC, the detector material investigated, the energy required to produce one electron/hole (e/h) pair is  $\sim 8.4$  eV. From this we can calculate the total number of e/h pairs produced. For a 5.48 MeV  $\text{Am}^{241}$   $\alpha$  we will get  $\sim 652,000$  e/h pairs, an induced charge of  $\sim 100$  fC. This is easily detectable using a standard charge sensitive pre-amp and amplifier set up.

### Fast electron interactions

Fast electrons, generally referred to as MIPS (minimum ionising particles) interact differently in an absorber than do heavy charged particles. As well as the Coulomb interactions which dominate in heavy particle interaction MIPS can also have collisional interactions with nuclei and radiative processes, *bremstrahlung* or ‘breaking radiation’ caused when an electron is suddenly decelerated releasing X-rays. The variant Bethe-Bloch formula for this MIPS interaction is

$$-\left(\frac{dE}{dx}\right)_c = \frac{2\pi e^4 N Z}{m_0 v^2} \times \left[ \ln \frac{m_0 v^2 E}{2I^2(\beta - \beta^2)} - (\ln 2) \left( 2\sqrt{1 - \beta^2} - 1 + \beta^2 \right) + (1 - \beta^2 + \frac{1}{8} (1 - \sqrt{1 - \beta^2})^2) \right] \quad (5.3)$$

All the symbols have the same meaning as in Eqn. 5.2, and  $\beta$  is  $v/c$ . This

takes into consideration the much larger portion of the total energy which can be transferred to a single orbital electron due to the similar masses. Also included is the near relativistic velocities of these particles.

The formula for radiative energy transfer is given by

$$\left(\frac{dE}{dx}\right)_r = \frac{NEZ(Z+1)e^4}{137m_0^2c^4} \left(4\ln\frac{2E}{m_0c^2} - \frac{4}{3}\right) \quad (5.4)$$

This is included for completeness as radiative energy transfer is relatively insignificant at the energies being investigated, with most generated photons recombining close to the point of generation.

Due to the reduced interaction rates for MIPS it is possible for some particles to travel all the way through the detector with minimal interaction while others will undergo collisions and deposit all of their energy in the material. This reduces drastically the number of e/h pairs produced in the material. Using Eqn. 5.3 a 2.2 MeV Sr<sup>90</sup> beta source produces ~5000 e/h pairs per 100 μm of SiC [49] evenly distributed throughout the material. This is ~1 fC induced charge. In order to detect these particles it is essential to have low noise electronics and a very sensitive amplifier.

### **X- and gamma-ray interactions**

There are three possible methods for photons to interact with the absorbing material of the detector: photoelectric absorption, Compton scattering, and pair production. During photoelectric absorption a photon interacts with an orbital electron in the detector material as a result of which the electron is ejected and the photon completely disappears. The energy of this *photoelectron* is given by

$$E_e = h\nu - E_b \quad (5.5)$$

where  $E_b$  is the binding energy of the photoelectron in its original shell. This is the major energy transfer process for low energy gamma-rays and X-rays. The probability of a photoelectric interaction is enhanced by the  $Z$  number of the absorber. An approximation for the probability is given by

$$\tau \cong \text{constant} \times \frac{Z^n}{E_\gamma^{3.5}} \quad (5.6)$$

where  $n$  varies between 4 and 5 depending on the photon energy. The severe dependance on  $Z$  for photoelectric absorption explains the variation in efficiency between different absorber materials and the development of high  $Z$  materials like CdZnTe for X-ray detection. The relatively low  $Z$  of SiC, 14/6 respectively, means that it is not a particularly efficient X-ray absorber.

Compton scattering interactions partially transfer the energy to an orbital electron, assumed to be initially at rest, which is then known as the *recoil electron*. The energy transferred to the electron can vary from zero to almost all of the initial photon energy. This is because of the wide range of possible scattering angles. The interaction is shown in Fig. 5.3. The relation for the energy of the scattered photon is given in Eqn. 5.7

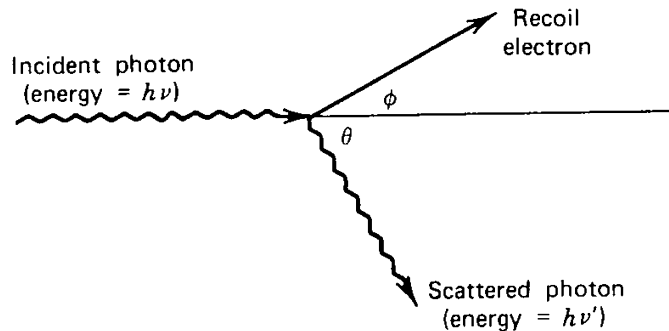


Figure 5.3: Compton scattering for photon incident on an electron [46].

$$h\nu' = \frac{h\nu}{1 + \frac{h\nu}{m_0c^2}(1 - \cos\theta)} \quad (5.7)$$

where  $m_0c^2$  is the rest mass of the electron (0.511 MeV). The probability of Compton scattering increases linearly with increasing Z number.

For gamma-rays of energy greater than twice the rest mass of an electron (1.02 MeV) pair production is energetically possible. In this interaction a photon enters the Coulomb field of a nucleus and disappears to be replaced by an electron-positron pair. Any energy above the 1.02 MeV minimum is translated to kinetic energy for the resultant pair of particles. In practice this interaction has a very low probability until the energy reaches several MeV. Because of this, pair production is predominately confined to very high gamma ray energies and is not covered in great detail here.

The relative importance of each of the three types of interactions discussed is illustrated in Fig. 5.4. The line on the left follows the energy at which the photoelectric effect and Compton scattering are equally likely while the line on the right is where Compton scattering and pair production are equally likely, as a function of the absorber atomic number Z.

### Neutron interactions

Like photons, neutrons are uncharged and so cannot interact by the Coulomb force. Neutrons can also travel for long distances, centimetres, through materials without any interactions and so can appear to be invisible to a standard semiconductor detector. When neutrons do interact it is with the nucleus producing a number of secondary radiations. Like the photon the neutron can either disappear completely, similar to the photoelectric effect, or it can be scattered, similar to Compton scattering. Unlike photons almost all neutron interactions produce a heavy charged particle. Neutron interactions come in

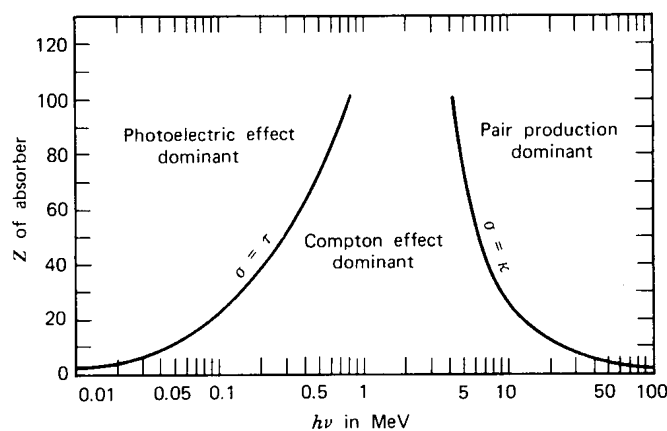


Figure 5.4: Change in importance of the different photon interactions with energy [46].

two main types, slow neutron interactions and fast neutron interactions.

Slow neutrons have a large number of possible outcomes including elastic scattering with absorber nuclei and neutron-induced nuclear reactions. The low kinetic energy of slow neutrons means that energy transferred in elastic scattering is minimal. This is consequently not a suitable reaction for detection. However the rate of elastic scattering is very high bringing many of the neutrons into thermal equilibrium with the absorber. The interactions which make it possible to detect slow neutrons are the neutron induced reactions which create secondary radiations which can then be detected. The most useful of these are the  $(n,\alpha)$ ,  $(n,p)$ ,  $(n,\text{fission})$  all of which cause secondary ionisation and can be reliably detected. The  $(n,\gamma)$  reaction is very common but is not as desirable as the emitted photon is not as easy to detect.

The likelihood of useful neutron interactions drops off very quickly as the energy increases. However for fast neutrons the importance of scattering increases as the amount of energy that can be transferred becomes significant.

The secondary products here are called *recoil nuclei*, which have picked up a detectable amount of energy from the collisions.

If the energy of the neutron is sufficiently high, inelastic scattering can take place. In this case enough energy is transferred to a single nucleus to raise it to a higher energy level. This energy is then re-emitted as an energetic  $\gamma$  with the neutron losing a larger fraction of its initial energy than would otherwise be the case. Inelastic scattering and the related high energy  $\gamma$  are considered to be a problem for detectors which rely on the elastic scattering to detect neutrons.

For neutrons of a fixed energy the likelihood of an interaction is governed by the *cross section*  $\sigma$  per nucleus for each type of interaction. For a general neutron flux these will be energy dependent. This allows a general reaction rate density to be defined as

$$\text{reaction rate density} = \varphi(r) \Sigma_{tot} \quad (5.8)$$

$$\Sigma_{tot} = N\sigma_{scattering} + N\sigma_{rad.capture} + \dots$$

which can be generalised to a non-uniform neutron flux by converting to  $\varphi(r, E)$ , and  $\Sigma(E)$  an energy dependent neutron flux and cross section, giving

$$\text{reaction rate density} = \int_0^{\infty} \varphi(r, E) \Sigma(E) dE \quad (5.9)$$

### 5.3.2 Charge collection

The properties of Schottky barriers were previously discussed as well as the fabrication of a Schottky barrier diode for use as a radiation detector. The application of a negative voltage to the Schottky contact modifies the barrier height by forced lowering due to the Schottky effect, shown in Figs. 4.5 and

4.7. The addition of an external bias increases the width of the depletion region as can be seen from Eqn. 4.4, where  $V$  is the applied voltage. The external applied bias also modifies the electric field within the detector. With all of the applied bias dropping across the widened depletion region, this leads to an electric field distribution as shown in Fig. 5.5.

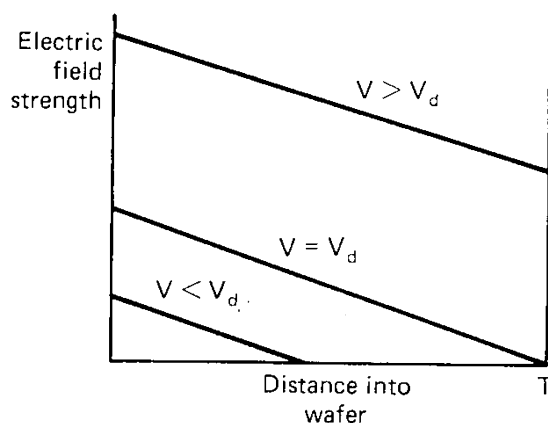


Figure 5.5: Field distribution through a semiconductor detector for various bias voltages.  $V_d$  is the depletion voltage of the device [46].

In a fully depleted detector the applied bias is high enough to make the width of the depletion region  $\geq$  the width of the semiconductor. This field causes all of the free charge to be swept out of the depletion region. At this point the only free charges available within the depleted area of a detector will be those created by the path of the ionising particle. These induced charges are also now swept out by the electric field, that is, accelerated towards the collecting electrodes depending on the polarity of the charge. The charge collected depends on the amount of energy which has been deposited by the radiation in the detector and also the rate of charge recombination and trapping which will be discussed later.

After the collection of charge from the detector it is necessary to transfer it to the readout apparatus. The latter generally consists of a charge sensitive pre-amplifier which converts the generated charge to a current pulse. The current pulse is then fed to a high gain main amplifier to boost the signal to an observable level. This is then connected to an oscilloscope and Maestro 32, a manual threshold data acquisition program which allows binning for different sized current pulses. These can then be converted to energies by use of a known calibration scale.

### 5.3.3 Energy calibration

The energy calibration for a detector is important as it allows a measure of how much energy is deposited within the detector. As has already been said a 5.48 MeV  $\alpha$  particle has a range of  $\sim 18 \mu\text{m}$  in SiC. This means that the total energy of the particle will be deposited in the body of the detector for the 100  $\mu\text{m}$  thick SiC diodes tested. However more energetic particles or those with a lower charge will travel further due to lower interaction rates. This could mean that not all of the energy of the particle is deposited in the depletion region of the detector. This is more important for MIPS and uncharged particles like photons or neutrons.

The readout system is calibrated with respect to known energy sources with a detector assumed to collect 100 % of generated charge. In the case of the readout system for testing SiC diodes, a Si surface barrier diode was used. This was used to take spectra of a number of mono-energetic spectroscopic sources  $\text{Am}^{241}$ ,  $\text{Pu}^{239}$ , and  $\text{Cm}^{244}$ . The energy of each of these particles is well known so a linear plot may be made of energy against the channel number, i.e. bin number, for the data acquisition software. The gradient of

this plot can be used to convert directly from channel number to energy for identification of the incident radiation.

### 5.3.4 CCE measurements

CCE (charge collection efficiency) is a measure of how much of the generated charge has been collected by a given detector. By use of a calibrated readout system the equivalent energy of the detected pulse can be calculated. This is then converted to a CCE by simply dividing by the total energy which was deposited in the body of the detector.

For SiC before a CCE measurement can be made there is an additional correction factor to be taken in to account, the difference in the energy needed to create an electron/hole pair in SiC is  $\sim 2.5$  times that required for Si. This means that for equivalent radiation sources  $\sim 40\%$  of the charge generated in a Si detector will be generated in the SiC detector. If a correction is not made this will give an error that drastically reduces the apparent signal. To correct for the difference in e/h pair creation energies the channel numbers are multiplied by the ratio  $E_{e/h}(\text{semiconductor})/E_{e/h}(\text{Si})$ . The total formula for calculating CCE is thus,

$$CCE(\%) = \frac{(\text{channel } n^2 \times \text{calibration scale}) \times \frac{E_{e/h}(\text{semiconductor})}{E_{e/h}(\text{Si})}}{\text{energy available}} \quad (5.10)$$

This gives the energy detected as a fraction of the total energy deposited in the detector. Comparisons between detectors of various material types are then possible. CCE measurements also allow comparisons between detectors of similar materials to observe performance degradation e.g. from irradiation induced damage.

## 5.4 Results for SiC detectors

A number of detectors were fabricated from 100  $\mu\text{m}$  thick S.I. SiC. These were then tested for I-V characteristics and CCE using an  $\text{Am}^{241}$  source producing 5.48 MeV  $\alpha$  particles. SiC has an electron/hole pair creation energy of 8.4 eV producing  $\sim 652,000$  e/h pairs within 18  $\mu\text{m}$  of the sample surface. CCE was measured for a range of voltages up to break down. A number of samples were irradiated at the Paul Scherrer Institut (PSI) with 300 MeV/c pions. CCE measurements and I-V measurements were taken for these to give an indication of the expected performance of these diodes in a high radiation environment.

### 5.4.1 Un-irradiated diodes

A number of diodes were fabricated in a range of sizes. Three of these were bonded into test fixtures and tested for I-V characteristics. The current voltage measurements from completed devices often differed on repeated measurements. Humidity and temperature measurements were taken to observe the effects of these on the I-V curves. The reverse current is plotted against the humidity as shown in Fig. 5.6. This gives an indication of how the current changes with ambient conditions. These measurements were all made at the same temperature, 25  $^{\circ}\text{C}$ . Investigations of the effect of humidity on SiC were made by Connolly et al [50]. They attempted to make a temperature insensitive humidity detector, observing a large reduction in the resistance of SiC when exposed to high levels of ambient humidity. The effects of humidity on Si have also been noted by Rantjan et al [51]. High humidity causes a build up of negative charges at the surface producing horizontal expansion

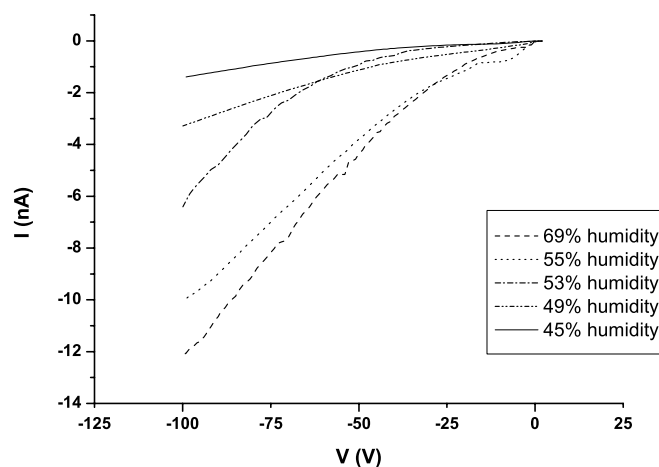


Figure 5.6: Reverse current plots for 500 $\mu$ m pad from 0- -100V for different humidity levels.

of the depletion region and hence order of magnitude changes in the leakage current.

A surface passivation layer of  $\text{Si}_3\text{N}_4$  was deposited onto the surface as discussed at the start of this chapter. A guard ring was included in the diode design to control surface leakage current. However, surface contamination and atmospheric effects, e.g. high humidity, can exacerbate the effects of surface currents. In this case the inclusion of the surface passivation reduces the leakage by isolating the surface from atmospheric contamination. Current-voltage measurements were then taken. The current measured was converted to  $J$ , the current density. This has been done to allow comparison between diodes of different diameters. Also  $J$  is used in the calculation of the Schottky barrier height using Eqn. 4.12.

Fig. 5.7 shows I-V measurements taken for a 500  $\mu$ m diameter pad diode over the range  $\pm 600$  V. The current/voltage characteristics show a Schottky

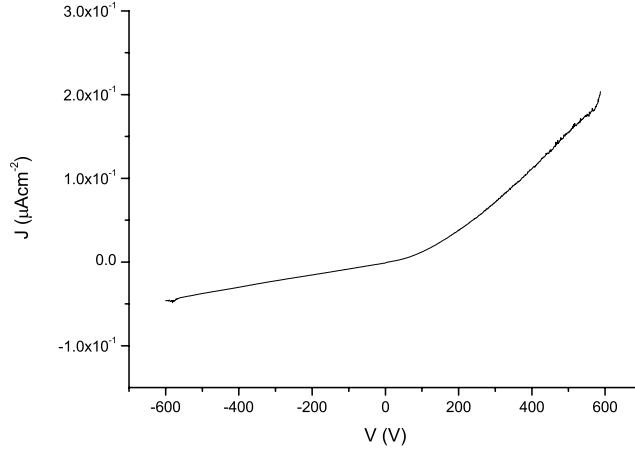


Figure 5.7: Current density against voltage for a Schottky barrier diode fabricated on S.I. 4H-SiC.

barrier type profile in the reverse, negative voltage, direction with a very resistive ohmic behaviour in the forward, positive voltage, direction. Leakage current in the negative current regime are  $\ll 0.1 \mu\text{Acm}^{-2}$  at 600 V. The lack of a good low resistivity ohmic contact is attributed to the V (vanadium) doping concentration which was used to make the material semi-insulating. The V dopant removes free electrons reducing the carrier content to increase the resistivity. This changes the material from being n-type which is nominal for SiC to S.I. material which is almost intrinsic, i.e. with very few free carriers. Using data from this curve the Schottky barrier height was calculated at 1.89 eV with a material resistivity of  $\sim 10^{11}\Omega\text{cm}$ . The theoretical value for the Schottky barrier formed for Ni on S.I SiC is  $\sim 1.95$  eV using Eqn. 4.1 where  $\phi_m = 5.15$  eV, the metal work function for Ni [36] and  $\chi = 3.2$  eV the electron affinity for SiC.

C-V measurements of the devices were also made. Plots of  $1/C^2$  against

applied voltage indicated when a detector had reached full depletion. If the device does not become fully depleted then the depletion width can be calculated from Eqn. 4.5. Fig. 5.8 shows a CV plot for an unirradiated detector. The flat line response over the voltage range indicates that the device is in effect fully depleted, i.e. has very few free carriers.

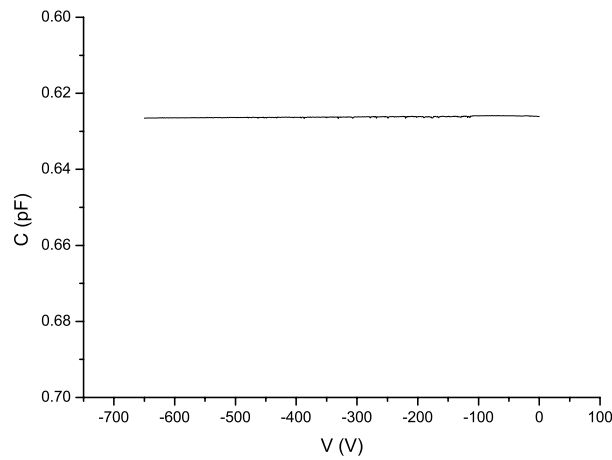


Figure 5.8: Capacitance against voltage for an unirradiated SiC detector.

After current voltage characterisation and C-V measurements, spectra were obtained using a number of diodes. Spectra were taken of an  $\text{Am}^{241}$  source producing 5.48 MeV  $\alpha$  particles. Fig 5.9 shows the development of the spectra with increasing bias voltage. The maximum CCE measured was  $\sim 60\%$ . The change in CCE with voltage can give an indication of how close to its maximum potential a detector is operating.

As the applied bias is increased the position of the peak moves, caused by an increase in the amount of charge being collected. For devices which are operating at their theoretical limit the CCE value will plateau at 100 %.

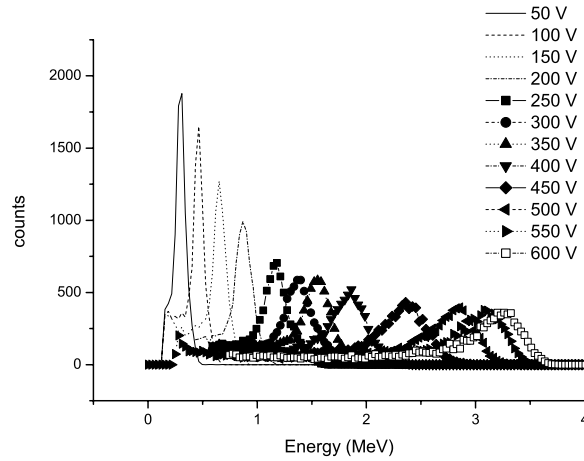


Figure 5.9:  $\text{Am}^{241}$  spectra taken at increasing bias voltages. Note the low energy tail on the higher bias voltage spectra.

However for devices which are operating below optimum the CCE increases approximately linearly with the applied bias. Fig. 5.10 shows the CCE values for the spectra of Fig. 5.9. As can be seen the CCE increases in a linear fashion with no apparent flattening of the line. This suggests that increasing the voltage or increasing the magnitude of the electric field within the device may produce yet higher CCE values than could be observed. The increase in charge collection is generally caused by an increase in the width of the depletion region. However Fig. 5.8 shows that the depletion region is not changing. In this case therefore it may be caused by an increase in the field strength leading greater acceleration of the charges. This means that more charge can be collected before it is recombined within the semiconductor.

The spectra show a pronounced low energy tail in the peak which is a possible reason for the incomplete CCE observed. A number of possible reasons for this tail exist including rising noise with the increase in bias

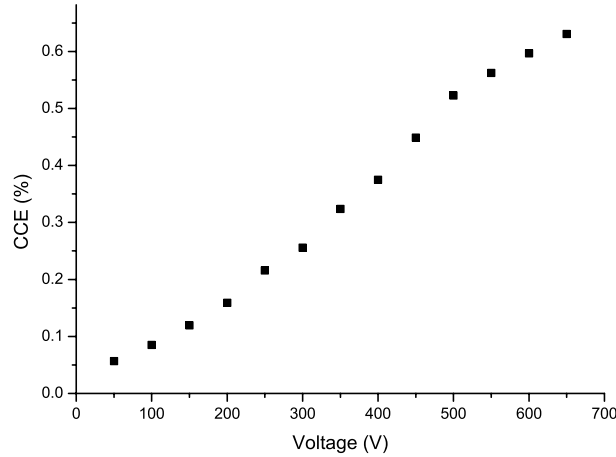


Figure 5.10: Peak positions as a function of the increasing bias voltage.

voltage. However the very low leakage currents observed seem to rule this out. Another reason could be the existence of traps and defects within the material. It is possible for generated charge to become trapped due to defects and later to de-trap. This causes a spread in the time it takes for the charge to be collected, possibly over several amplifier cycles. Spreading the charge collection over several cycles reduces the charge detected in the main pulse, reducing the apparent CCE. It can also produce a number of much smaller pulses over a large time scale causing the low energy tail to be observed. An investigation into the existence of traps and defects with SiC was undertaken to try and understand this reduced CCE.

#### 5.4.2 Trap measurements and spectra

There are a number of defects which are well known in SiC. The most important of these is the micropipe [52]. A micropipe is a hollow core super screw dislocation. That is a screw dislocation with a Burgers vector  $> 2c$ . The

Burgers vector is a measure of how much more than the ideal path length around a lattice point that would have to be travelled because of the dislocation. For a micropipe the dislocation distance is greater than twice the lattice constant. Micropipes have been acknowledged to cause the breakdown voltage of rectifying devices to decrease by over 50 %. Micropipe densities in commercially available materials are in the range  $\sim 10 \text{ cm}^{-2}$ . Other screw dislocations known as elementary screw dislocations have a Burgers vector  $= 1c$  with no hollow core. These are not as detrimental to performance as micropipes with lowering in breakdown voltage in the region 5- 35 % [53]. However these are much more numerous than micropipes with densities 100 times greater i.e.  $1000\text{'s cm}^{-2}$ . The main effect of these defects is to reduce the breakdown voltage of the device. They are not linked with charge trapping.

A number of experiments were undertaken to determine if there were other defects or traps present in the detector material could have produced the long low energy tail which was observed in the spectra. Two distinct experiments were carried out. The first examines the length of time it takes to discharge a detector after running at maximum operational voltage for varying lengths of time. The second uses a process called TSC (thermally stimulated current) to observe the activation energies of any traps within the material.

### **Current decay time measurements**

The first of these experiments investigated post-bias decay currents. When the sample is biased, charge is trapped in defects in the material. To investigate this the sample was biased at -600 V, the maximum operating voltage,

for varying lengths of time, up to an hour. After the voltage was removed the current was measured over several thousand seconds as the trapped charge was released. The measured current was plotted against  $\log(t)$ . Exponential curves were fitted to the data using Microcal's Origin package. Initial fits with one or two exponential decay terms failed to fit the data. However an expression of the form

$$y = y_0 + A_1 e^{-x/t_1} + A_2 e^{-x/t_2} + A_3 e^{-x/t_3}$$

produced a good fit. To test the validity of the curves the fit was forced to use the same exponents, for all data sets seen in Fig. 5.11. The figure shows all of the data sets. The time constants were calculated at  $t_1 = 15$ ,  $t_2 = 125$  and  $t_3 = 4$  s.

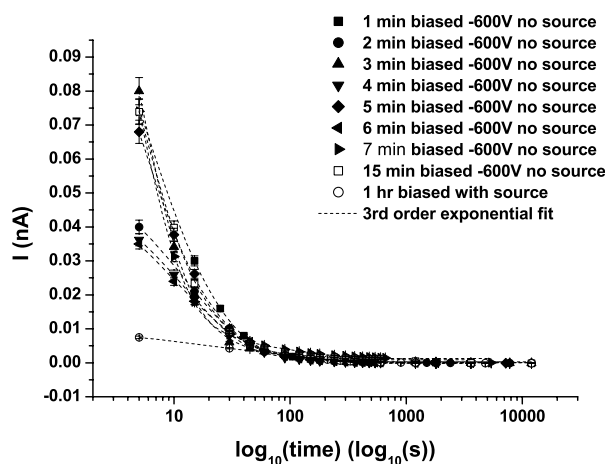


Figure 5.11: Discharge currents measured from diode after biasing for varying lengths of time plotted against  $\log(t)$  from the point of bias turn off.

The reduced  $\chi^2$  goodness of fit test has a value of  $\sim 0.9$  for all nine curves showing that the fitted curve approximates the data well. These very long

lifetimes give a possible explanation for the large low energy tail which is observed in the spectra. These three measured time constants appear to show that there are three separate decay processes taking place within the material. In order to further understand what is happening with the trapped charge it is necessary to find the activation energy of the traps a high activation energy implies that it will take a long time to release trapped charge as is being observed here.

### **Thermally stimulated current**

Thermally stimulated current (TSC) is a method used to observe the change in measured current through a sample as the temperature changes. By cooling the sample to liquid nitrogen temperatures,  $\sim 75$  K, the energy available within the lattice of a crystal is sufficiently low that the number of available free carriers becomes effectively zero. If the sample is allowed to warm up to room temperature, or above, carriers are released. If the material has no traps or defects the curve produced will be a smooth line when plotted on an exponential scale.

However, the introduction of traps into the material has the effect of producing peaks in the curve. The gradients of these peaks may be used to calculate the energy required to ionise a carrier from this trap. Larger trap energies mean that it takes longer for a trapped carrier to be released. Fig 5.12 shows an Arrhenius plot of the TSC data for unirradiated S.I. SiC. The various peaks that can be seen relate to a number of different defects. Table 5.2 has the temperatures, activation energies and possible attribution for each of the observed levels.

The largest of these is caused by the activation of the V (vanadium)

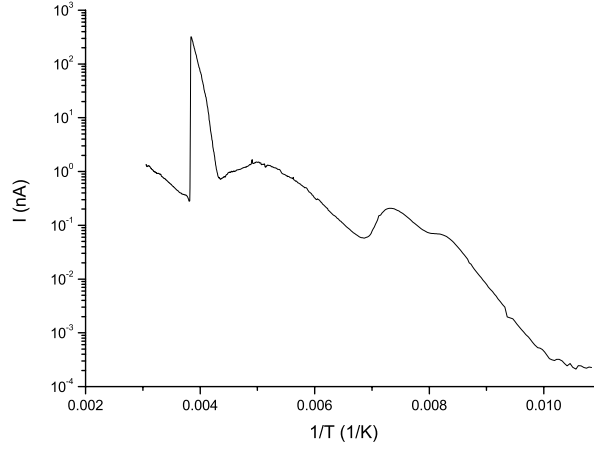


Figure 5.12: Arrhenius plot of TSC measurements taken of SiC diode. The behaviour observed is complex suggesting a number of different defects.

Table 5.2: Temperature, activation energy and possible attribution of peaks in TSC spectra.

Temperature (K)	Ea (eV)	Attribution
118	0.32	Un-compensated boron[54]
135	0.39	or localised dislocation[55]
200	0.63	Carbon vacancy [55], Carbon interstitial-nitrogen or Silicon vacancy [56]
260	0.92	Vanadium activation[57]

dopant. The traps at 0.32 and 0.39 eV are close to the 0.35 eV level for uncompensated boron which is mentioned by Mitchell et al [54]. However another possibility for these is localised lattice dislocations. Bechstedt et al [55] report a defect complex at 0.35- 0.45 eV the so-called  $D_1$  centre. The level observed at 0.63 eV has been attributed to a number of different causes one of which is a hexagonal lattice site carbon vacancy [55] at 0.63 eV. The most likely explanation is reported as the  $Z_{1/2}$  defect by Pintilie et al [56] with activation energy at 0.66 eV. This is comparable to the 0.63 eV defect

observed here. This is attributed primarily to a carbon interstitial-nitrogen defect which is influenced heavily by the concentration of nitrogen and the C/Si ratio in the growth process.

The comparatively large energy of these traps allows them to be potentially related to the lifetimes which were measured earlier using the decay current method. The largest activation energy trap at 0.92 eV could correspond with the decay time of 125 seconds which in the case of the spectra taken is approx half of the This gives a very good explanation for the missing charge when these devices are operated as detectors. Also the long low energy tail can be explained by the large amounts of trapped charge being released slowly for the duration of detection.

### **Simulation of CCE in S.I. SiC diodes**

The maximum measured CCE value for the tested diodes was 60 %. Measurements of traps show a large trap peak associate with the vanadium dopant in the material. As this was the largest of the trap peaks it was assumed to have the biggest effect on the amount of charge collected. The effect of this dopant on the possible CCE and the mobility of charge carriers within the material was simulated by T. Quinn et al. [60]. By varying the concentration of the V dopant in the material and simulating charge transport and CCE it was observed that a dopant density of  $> 10^{17} \text{ cm}^{-3}$  dramatically reduced the electron pulse height and lowered the maximum possible CCE to  $\sim 60$  %. The data is shown in Fig. 5.13.

The changes in the properties of the material, particularly the CCE, mean that the diodes produced on S.I. SiC were functioning as well as possible. In order to improve the CCE a different type of SiC will be required which does

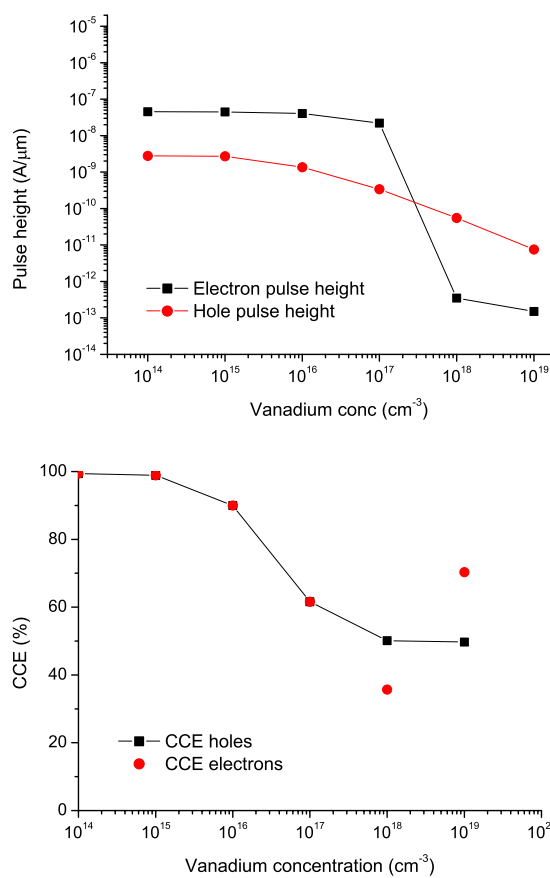


Figure 5.13: *top* The effect of varying the V density on the electron pulse height. *bottom* The effect of varying the V density on the maximum possible CCE.

not have the V dopant.

### 5.4.3 Irradiated SiC diodes

The main reason for investigating SiC is the hope of producing detectors that are more radiation hard than traditional Si detectors. In light of this the effects of radiation on the performance of these detectors is very interesting. A number of diodes similar to those used for the initial tests were sent for

irradiation with 300 MeV/c pions at the Paul Scherrer Institut in Villigen. Samples were irradiated to fluences of  $10^{12}$ ,  $10^{13}$ , and  $5 \times 10^{14} \text{ } \pi\text{cm}^{-2}$ . The maximum fluence was chosen to be equivalent to several years operation in a high radiation environment.  $5 \times 10^{14} \text{ } \pi\text{cm}^{-2}$  being equivalent to approx 10 years LHC operation at CERN.

I-V measurements were taken to allow changes in the leakage current and Schottky barrier height to be observed. Pulse height spectra were also taken. However only spectra for fluences of  $10^{12}$  and  $10^{13} \text{ } \pi\text{cm}^{-2}$  are available. The third diode with  $5 \times 10^{14} \text{ } \pi\text{cm}^{-2}$  fluence was damaged when being bonded so I-V measurements were taken but spectra are not available.

### I-V characterisation

After irradiation with pions current/voltage measurements were taken and compared with the undamaged devices. I-V measurements as already discussed allow calculation of the Schottky barrier height and also indicate the approximate device resistivity. The shape of the curves has changed dramatically compared to zero irradiation, particularly the lower fluence samples. These have a comparatively low break down voltage. The higher fluence sample shows a significant recovery towards the pre-irradiation current levels. A comparison between the currents can be seen in Fig. 5.14. From these measurements the data shown in Table 5.3 was produced. In the the table the barrier height was calculated using Eqn. 4.12,  $\rho$  is the resistivity and  $n$  is the carrier concentration. Resistivity is calculated using  $\rho = (V/I) \times \text{thickness}$ . The carrier concentration was calculated using  $n \cong 1/(q\mu_n\rho)$ , where  $\mu_n = 900 \text{ cm}^2\text{V}^{-1}\text{s}^{-1}$  is the electron mobility.

By comparing the data shown in Table 5.3 with the I-V curves in Fig.

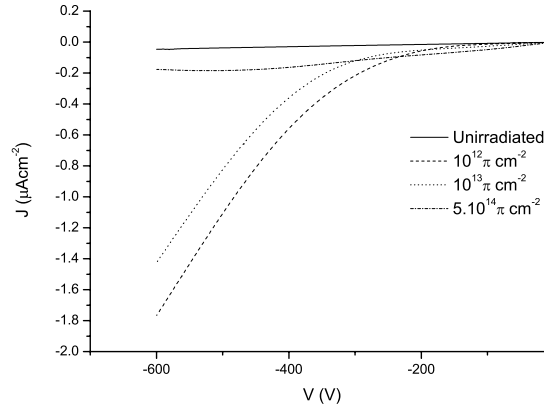


Figure 5.14: Comparison of post irradiation currents with pre-irradiation current.

Table 5.3: Variation in measured barrier height, resistivity, and carrier concentration with increasing fluence.

Fluence ( $\pi\text{cm}^{-2}$ )	Barrier height (eV)	( $\rho$ ) ( $\Omega\text{cm}$ )	n ( $\text{cm}^{-3}$ )
unirrad	1.89	$1.26 \times 10^{10}$	$2.71 \times 10^{11}$
$10^{12}$	1.88	$7.32 \times 10^9$	$8.07 \times 10^{11}$
$10^{13}$	1.87	$1.33 \times 10^{10}$	$2.44 \times 10^{11}$
$5.10^{14}$	1.86	$2.45 \times 10^{10}$	$7.23 \times 10^{10}$

5.14 the effects of certain changes in the material can be observed. The lowest fluence,  $10^{12} \pi\text{cm}^{-2}$ , sample has a very low breakdown voltage,  $\sim 200\text{V}$ , and a very sharp increase in the leakage current value. From the table we can see that this is correlated with a decrease in resistivity, an increase in the carrier concentration, and a slight decrease in the barrier height.

As the fluence increases, the values for these parameters continue to change. At  $10^{13} \pi\text{cm}^{-2}$  the resistivity has increased to a level comparable with the pre-irradiated value, the carrier concentration has decreased, and the barrier height has been lowered further. This correlates with the measured I-V showing, again, a low breakdown but a slower current rise than

before.

The highest fluence has an increased resistivity, decreased carrier concentration and again a lower barrier height. The graph shows that the current is nearer the pre-irradiation level. However, it has a slightly different curve shape. The lowered barrier causes an increase in the intrinsic dark current over the pre-irradiation sample but the higher resistivity means that the current does not increase rapidly like the lower dose samples.

### **Spectra from irradiated diodes.**

As mentioned spectra exist only for the two lower dose samples. The curves of Fig 5.15 were taken using the same setup as the pre-irradiation spectra also using  $\text{Am}^{241}\alpha$  particles.

Maximum CCE measured for these devices spectra were 47% and 50% respectively. For the low dose sample the signals are smooth and well formed but breakdown occurs at around -500 V. The  $10^{13} \text{ cm}^{-2}$  sample has a higher breakdown voltage near to  $\sim -600 \text{ V}$  as with the pre-irradiation sample. However, in this case the signals are not smooth instead rather noisy with jagged peaks. As with the I-V measurements the bias that can be applied improves as the dose increases, with CCE values also improving. If this trend were to continue the higher dose  $10^{14} \text{ cm}^{-2}$  might be expected to return to almost pre-irradiation levels. However no data is available to corroborate this. The change in measured CCE from  $10^{12}$  to  $10^{13} \text{ cm}^{-2}$  reflects the higher applied bias voltage rather than a change in the detection efficiency of the detector. The CCE is still lower than un-irradiated samples at a comparable voltage.

The reduction in CCE after the irradiation is expected. However, the

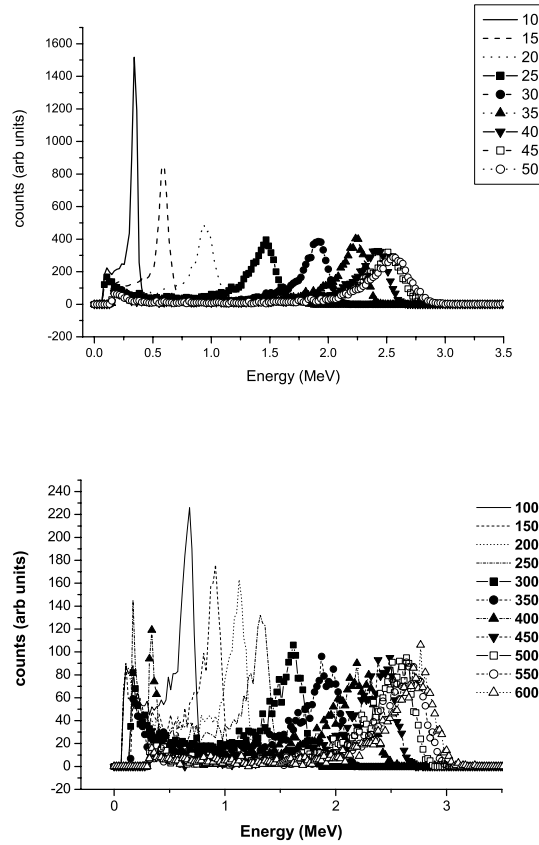


Figure 5.15: Am<sup>241</sup> spectra taken at increasing bias voltages for irradiated diodes. *top*  $10^{12} \text{ cm}^{-2}$  and *bottom*  $10^{13} \text{ cm}^{-2}$

magnitude of the reduction is not high. Published data for GaAs detectors show a drop in CCE of over 50 % [58] while Si has been shown to have a reduction of  $\sim 30$  % [59] with a greatly increased depletion bias after a similar dose of pions whereas the data here shows a reduction of 16 % compared to the pre-irradiation levels. This shows that SiC detectors show a promising degree of radiation hardness.

#### 5.4.4 Summary of SiC data and future work

The bulk SiC materials tested here have good physical and electrical properties for use as a detector material. The low leakage current at very high bias voltages means that the signals have very low noise under operation. Radiation induced damage in the material initially has a detrimental effect on the performance of the devices but they recover slightly with an increase in fluence. The changes are most obvious at the lowest fluence. This is equivalent to only a months operation with a dose of  $10^{13} \text{ } \pi\text{cm}^{-2}$  being equivalent to about 1 year of operational time in LHC. The recovery of the operational characteristics gives rise to an expectation of a long lifetime with relatively replacement free operation.

The relatively good performance of the irradiated detectors bodes well for the operation of these devices in high radiation environments. The data presented here is for bulk SiC detectors. A great deal more work has been carried out on epitaxial layers of SiC [61]-[66]. These use lightly doped n-type layers, no V dopant,  $\sim 30\mu\text{m}$  thick to fabricate on. They have provided 100 % CCE. There is one problem with the use of epitaxial layers bulk material can possibly overcome. The minimal thickness of the epi-layers means that for some high energy particles, or lightly interacting particles only a relatively small amount of energy will be deposited. This can be overcome by increasing the layer thickness. At this point the cost of epitaxial layers becomes the prohibiting factor.

A further area of investigation to increase the CCE is changing the type of material. The SiC material used in these experiments was doped with vanadium to  $\sim 10^{18} \text{ cm}^{-2}$ . As shown in Fig. 5.13 the changes in the material

properties caused by the V dopant mean that 60 % CCE is as good as the detectors can perform. By using material without the dopant the loss of charge may be reduced, giving an increased CCE. To this end new semi-insulating material produced without the V dopant is beginning to be tested to observe the difference in performance.

One final area of investigation would be into ohmic contacts to S.I. SiC. The technologies developed primarily for n-type material are not entirely satisfactory as the I-V curve in Fig. 5.7 shows. Experimentation with surface treatments, thermal processes, and different metals/ combination of metals would produce a good low resistivity ohmic contact which is vital for other applications not investigated here but are equally useful.

# Chapter 6

## Retinal readout system

### 6.1 Introduction

The retina is the part of the eye which is responsible for conversion of incident light into electrical signals which the brain can understand as an image. This process is not well understood and a system designed to study it will be discussed here. There are many reasons why researchers are interested in the retina. The first of these is to understand the function of the retina better. Another reason which maybe just as important, is that the retina is an accessible part of the brain located outside the skull. Also it can be maintained outside the body in saline solution and the stimulus is well known, visible light. This combination means that it is the simplest part of the brain to experiment with.

The retinal readout system is designed to use technology developed for high energy physics applications in concert with semiconductor fabrication techniques to study the retina. The technology is similar to that in microstrip detectors and is used to simultaneously detect signals from hundreds of output cells [11]-[13]. Single electrode studies using platinum wire have been used successfully to detect activity in retinal tissue [67, 68]. However, study-

ing the concerted signalling of neurons is not possible using this method. This can provide data on signal thresholds i.e. the lowest stimulus level possible and allow observations of responses to nearby stimuli. The one thing that single electrode systems cannot do is observe the response from a number of neurons to varying stimuli. The retina manages to combine  $10^8$  photoreceptors into  $10^6$  neurons. From this it is possible to imagine that a large amount of parallel processing is being carried out. The use of microelectrode arrays in retinal studies has expanded in recent years to increase the body of knowledge from that available using single electrode systems [69]-[78].

The knowledge which may be gained from these experiments is important in understanding how a vital part of the body works. However, another reason exists. *Macular degeneration* is a condition which causes degradation of the retina leading to blindness, it is one of the biggest causes of blindness in the west. The condition only damages the retina, the optic nerve is unaffected. If the encoding scheme used by the eye can be understood then the production of artificial retinas or retinal replacement technology is one step closer. Much work has already been carried out in this area with a variety of techniques being investigated [79]-[84].

In this chapter I will give a description of the retina, its component parts and how each functions, sufficient to understand the experiments being carried out. A detailed description of the functioning of the retina is beyond the scope of this work. The main section of the chapter will cover the different types of arrays that have been fabricated. Examples of data taken using the different types of arrays will be shown.

## 6.2 Retinal physiology

The retina itself is a complicated membrane which contains many different types of cells. These all have a purpose in producing a series of signals which can be transferred to the brain via the optic nerve and translated into an understandable image. As well as detecting the light the retina also performs a large amount of reasonably complex processing in its own right. This section will look at the different layers of cells in the retina and discuss the function of each. The discussion will mostly cover vertebrate retina but in the main, the types of cells found in all retina are the same with minor variations in the exact functionality or number of cell types. A much fuller treatment than that given here of the retinal biology and function can be found in ‘The Retina: An approachable part of the brain’ by J. E. Dowling [85].

### 6.2.1 Layers of the retina

The retina is split into three main layers which all have a different function in the operation of the retina as a visual apparatus. Fig. 6.1 is a vertical slice through a human retina from an area just outside the fovea. In the fovea the photoreceptors are smaller and more tightly packed than in the peripheral areas to give a higher resolution image. In the foveal region the inner layers of the retina are pushed aside to allow more of the incident light to impinge directly on the photoreceptors. This accounts for the sideways direction of the photoreceptor terminations.

This image shows all of the layers of the retina from the receptors at the top to the ganglion cells at the bottom. Because this was taken near the fovea

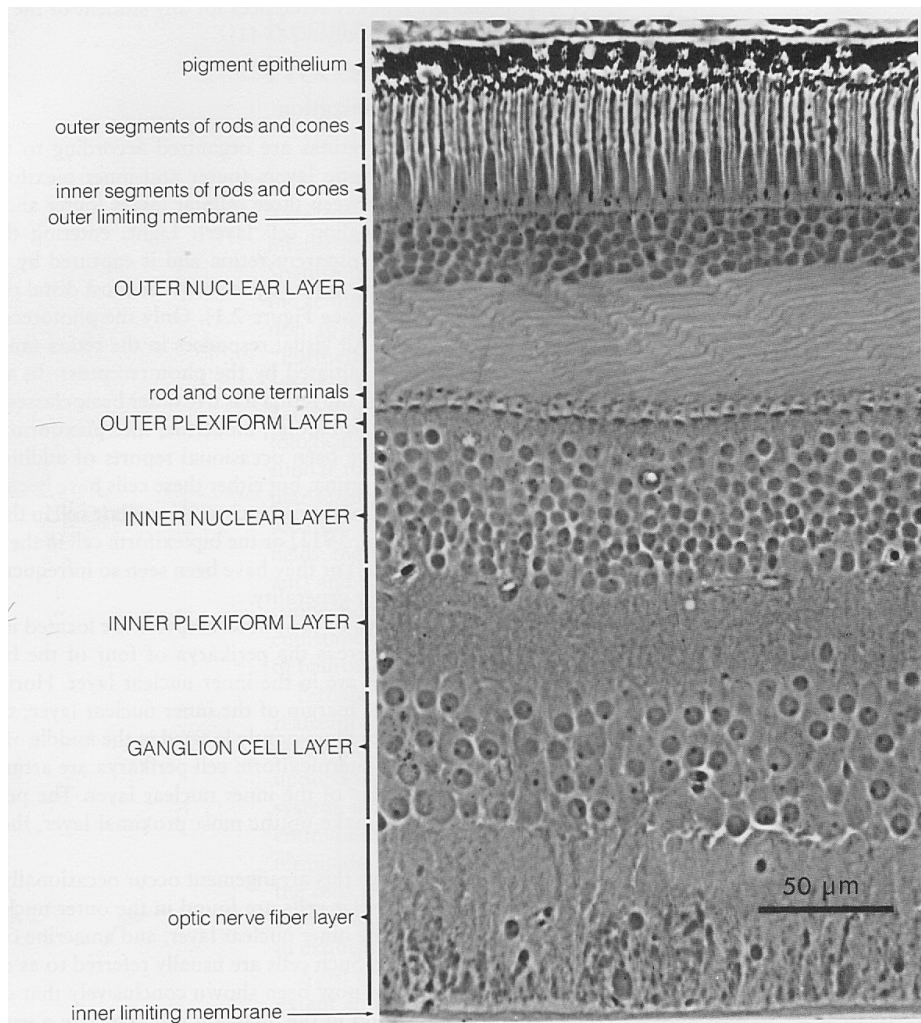


Figure 6.1: Vertical slice through human retina taken near the fovea [85].

the rod and cone terminals are slanted where the inner cell layers have been pushed aside. Fig. 6.2 shows a schematic view highlighting cells important in understanding the function of the retina.

Important sections of this are related to where cell connections occur. The three nuclear layers, the outer and inner nuclear layers and the ganglion layer, consist of cell bodies. The inner and outer plexiform layers are where

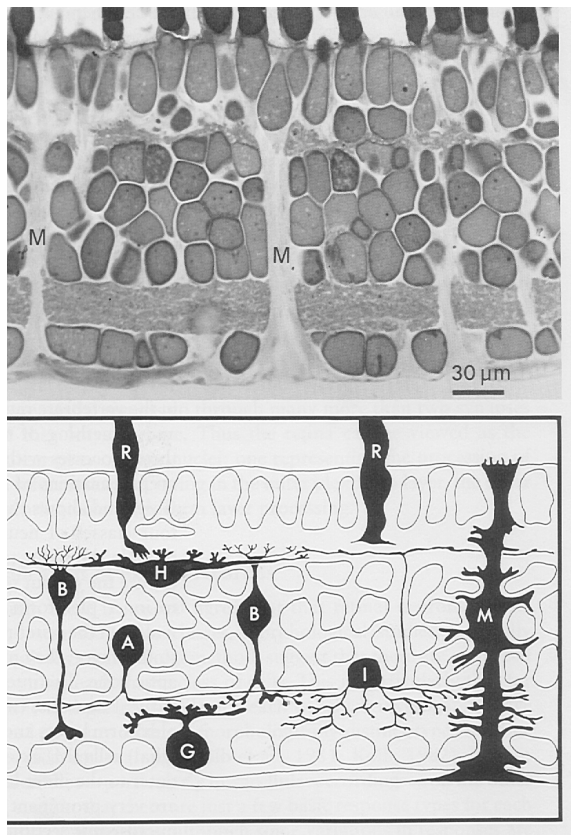


Figure 6.2: Schematic of retinal tissue showing all of the major cell types. *R* are receptors, *H* horizontal cell, *B* bipolar cell, *A* amacrine cell, *G* ganglion cell, *I* interplexiform cell, *M* Müller (glial) cell [85].

the different types of cells are connected and interconnected. The two layers are of different thicknesses due to the different functions performed in each.

The *outer plexiform layer* is where the receptor cells terminate. Connections are made to the *horizontal* and *bipolar* cells. Bipolar cells are responsible for connection to the ganglions. Horizontal cells are responsible for interconnections within groups of receptors and bipolar cells.

The *inner plexiform layer* is where the bipolar cells connect to the ganglions. At this stage they can be connected to a number of different ganglions.

Connections are also made to the amacrine cells. Amacrine cells perform a similar job to the horizontal cells. They provide interconnections between groups of bipolar cells and ganglions.

The *interplexiform* cells are different from the other cell types. They are responsible for transport of information between the inner and outer plexiform layers and may be extensively connected in both.

*Müller* cells are connected from the outer limiting membrane to the inner limiting membrane. They connect with each other on the surface of the retina and connect also to the photoreceptors.

### 6.2.2 Functionality of retina

The horizontal and amacrine cells are responsible for interconnections between multiple receptors and between groups of bipolar cells respectively. These allow a range of processes which can be translated to infer much information about the nature of the visual stimulation. Both types of photoreceptors have the same response to illumination. The potential of the cell increases in a process known as hyperpolarisation. However it is not enough to be able to say that light has hit a single photoreceptor and determine its colour, if applicable. The response of receptors that have not been directly illuminated is determined by the state of neighbouring receptors. The connections between the neighbouring receptors are possible due to the horizontal cells. A single variation of this non-illuminated response is given in Fig. 6.3 below.

This figure shows the main types of cells in the retina and the complex interconnections which occur within the inner and outer plexiform layers. The three ganglion types shown produce signals depending on the excitation



cells involved increases. The combination of ON, OFF, and ON-OFF signals which can be generated over a large area due to the interconnections between receptors and also between ganglions means that a great deal of information is produced. Also, it means that even simple localised stimuli can produce a large number of signals over a reasonably large area. This is where the multi electrode arrays produced for the Retinal Readout Project can prove invaluable.

### **6.3 Fabrication of retinal readout arrays**

In order to produce arrays which can be utilised for observation of signals from retinal tissue a number of factors have to be taken into account. The spacing between electrodes, the size of electrodes, and the number which are to be used all change the fabrication techniques which are suitable for array production. The changing size of arrays, the increasing density of the central electrode region, and the very large increases in electrode numbers means that a complete alteration of the array designs is also required. The development work carried out in Glasgow has a number of common stages. Production of wires uses dry etch techniques, deposition of a  $\text{Si}_3\text{N}_4$  layer, and a final etch to open windows in the  $\text{Si}_3\text{N}_4$  layer. However, while the etch chemistries and parameters used are themselves identical in some cases the fabrication of arrays had a number of distinct phases. The changes which will be discussed here were implemented to take into account different requirements of the changing designs. A detailed discussion of the processes used to produce arrays by dry-etching has been covered in Chapter 4.

### 6.3.1 Development of processes for fabrication: 61 electrode arrays

The first type of array to be produced has a central section with 61 electrodes with a  $60\ \mu\text{m}$  spacing. This is shown in Fig. 6.4.

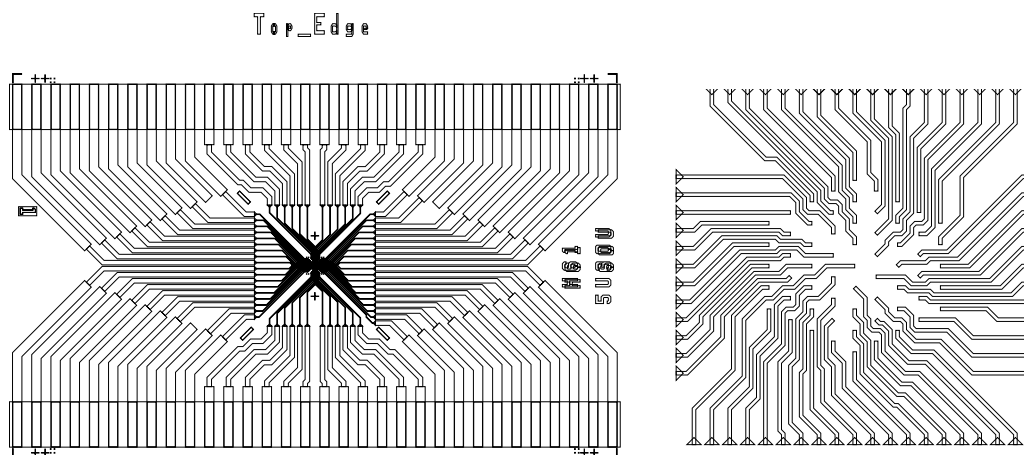


Figure 6.4: *left* Design for 61-electrode array. *right* Close up of central section showing the wire ends, where the electrodes were formed, with  $60\ \mu\text{m}$  spacing.

This array was one of the first multi-electrode arrays that was designed and fabricated. The  $60\ \mu\text{m}$  electrode pitch is approximately the spacing of motion sensitive retinal cells in the peripheral retina away from the fovea. The electrodes are wired out on two sides to specially designed chips each of which can handle 32 channels of data. Data has been recorded from arrays of this type for many years so it was the ideal design to develop and test a range of new fabrication techniques. The original fabrication method for these arrays was to use a wet etch of  $\text{HCl}:\text{H}_2\text{O}$  or  $\text{HF}:\text{H}_2\text{O}$  to produce the wires. However, this became unacceptable when the next generation of arrays was designed with a much denser central section with critical dimensions eventually going down to  $1\ \mu\text{m}$  wires and spaces.

Photolithography was used to define the pattern of the array and a mixture of methane and hydrogen ( $\text{CH}_4/\text{H}_2$ ) was used to etch the ITO.  $\text{CH}_4/\text{H}_2$  is a commonly used gas mixture for processing ITO. However, hydrocarbon gases cause great damage to photoresist with excessive crosslinking, as discussed in Chapter 2, this makes the resist difficult to remove. To get around this without introducing additional steps to the fabrication process a non-standard process was introduced [86]. This utilised a shorter post bake time for the resist layer after pattern development. The post bake promotes a level of crosslinking within the remaining resist. This ensures that the resist will be better able to withstand etch processes. However, because of the nature of the substrate the more aggressive cleaning techniques used for crosslinked or damaged resist were not available. Reduction of the post bake time left the resist softer than usual and subsequently liable to take greater damage during the etch. However, the reduction in post bake time was also sufficient to ensure that the crosslinking effects of the hydrocarbon chemistry were minimised. This allowed a single mask to be used when producing wires for the electrode arrays. Photolithography was also used to define the windows to be opened in the  $\text{Si}_3\text{N}_4$  layer. The parameters and details of the dry etch used are given in Chapter 4.

Fig. 6.5 shows a completed 61-electrode array with a close up of the central section. A number of arrays of this type were completed and tested to allow comparison with arrays produced using other fabrication techniques. Comparisons between impedance and performance in tests using retinal tissue proved favourable, and the next stage of development was begun.

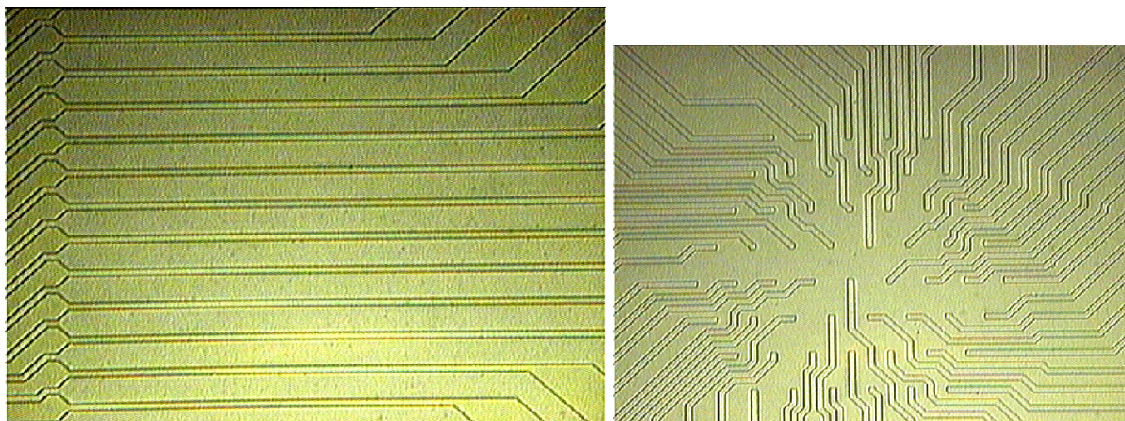


Figure 6.5: Sections of completed 61 electrode array. *left* Middle section of wires showing large wires with small spaces between. *right* shows an etched version of Fig. 6.4 *right*.

### 6.3.2 Development of processes for fabrication: 519 electrode arrays

The reason for a switch away from wet etch processing of arrays was to accommodate the change in scale needed to migrate from 61-electrode arrays to 519-electrode arrays. This requires a reduction in wire width by a factor of 5, from  $10\ \mu\text{m}$  to  $2\ \mu\text{m}$ . This was eventually planned to decrease to  $1\ \mu\text{m}$ . The density of closely packed wires was such that wet etching would be unable to produce the features. The design for a 519-electrode array is shown in Fig. 6.6. This shows the very dense central region of the array.

The first step that was changed was the type of lithography used. The 61 electrode array was produced using photolithography. This was suitable because of the relatively large feature sizes. However, it was not possible to use photolithography for the central area of the new array. The proximity effect, as discussed in Chapter 2, meant that the wires become exposed during the pattern transfer. To get around this a combination of photo- and e-

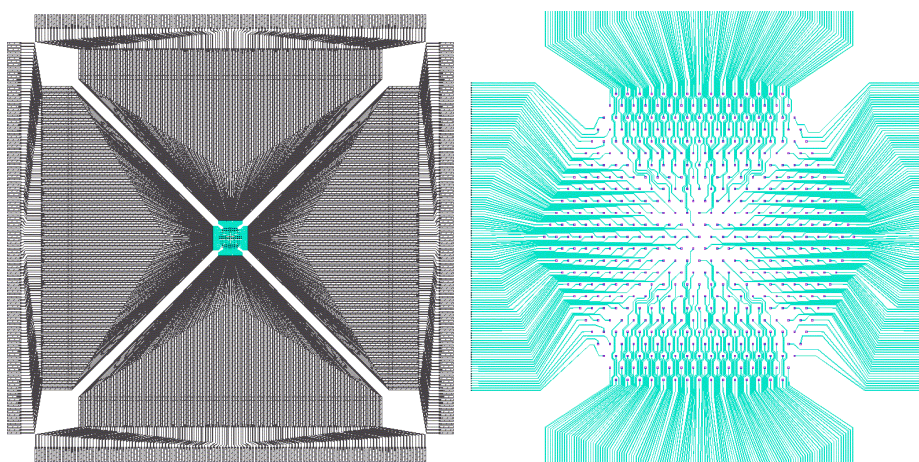


Figure 6.6: Design for 519 electrode array. Close up of central section on right shows square electrodes on wire ends with  $60 \mu\text{m}$  spacing.

beam lithography was investigated. A complete switch to e-beam was not considered viable at this time due to the long write time for each array,  $> 10$  hrs.

A series of photolithography masks was produced with alignment marks and outer wires leading from bond pads to a blank space in the centre. The dense central region would then be added using e-beam lithography. Fig 6.7 shows the modified design for producing 519 electrode arrays. The mask for the outer section leaves a large blank space which is then written over by e-beam to produce the full wire layout. The second layer of lithography to produce openings in the  $\text{Si}_3\text{N}_4$  passivation layer is still a photolithography step. Several test pieces were produced using this technique. However changes in the resist which was used allowed the process to be completely switched to e-beam lithography. The change from the standard e-beam resist PMMA (polymethyl-methacrylate) to UVIII reduced the required dose by an order of magnitude. UVIII is a chemically amplified deep UV resist which

is suitable for patterning by exposure to an electron beam. A more detailed discussion of the resist types was given in Chapter 2.

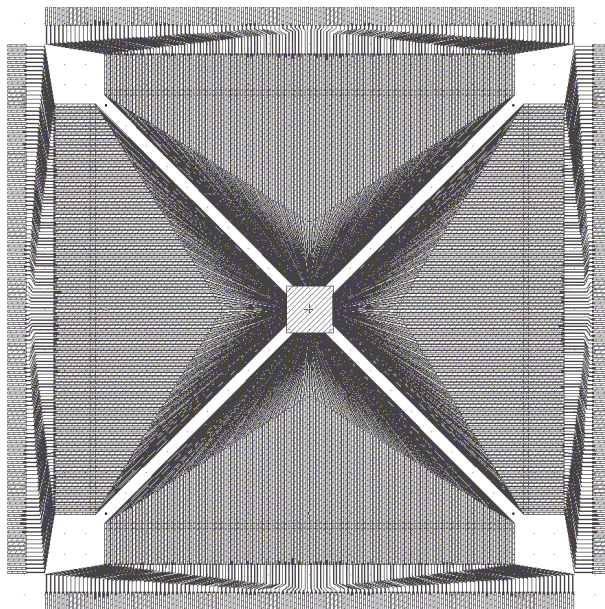


Figure 6.7: Modified design for 519 electrode array for combination photo- and e-beam lithography process with blank central section on the main wires mask.

The reduction in dose brought the direct write time for the whole array down to a more suitable length,  $\sim 4$  hrs. In order to reduce the number of stages in the fabrication process a move to direct write using e-beam was considered desirable. However this required a number of changes to the process already in place.

Computer controlled e-beam lithography systems use pattern recognition to find the required position to write patterns in relation to existing features. Another important piece of equipment is used for height measurement. This uses reflectance from the sample surface to focus the electron beam. This caused a problem for the samples being fabricated as both the ITO and the

glass substrate are optically transparent. Fig. 6.8 shows the problem caused

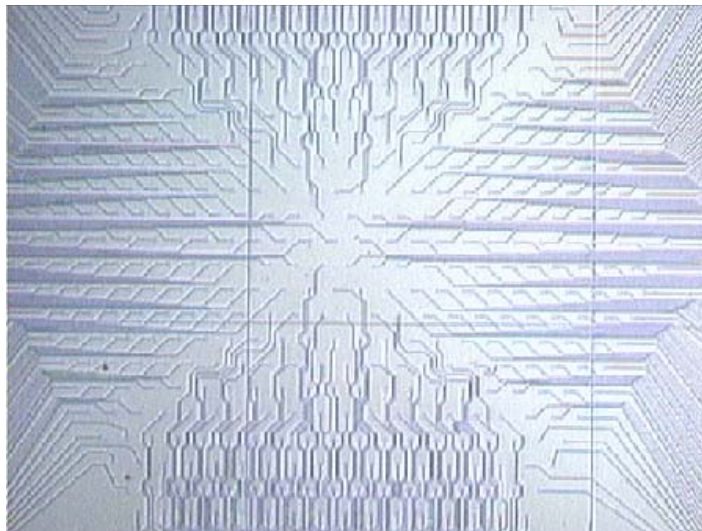


Figure 6.8: 519 array written by electron-beam. The grid like lines visible are where the pattern has been improperly stitched together. This is caused by the height recognition laser interferometer being unable to find the ITO surface.

by the transparency of the material. The transparent nature of the materials used means that the the optical pattern recognition software cannot find the surface at all times. When trying to stitch sections of the pattern together the individual frames do not meet exactly, leaving the grid like structure that can be seen overlaying the pattern.

Other problems arose from the thinness of the resist. E-beam resists are considerably thinner than photo-resists to allow writing of finer features. The development process can be likened to a very precise wet etching procedure. This means that to make patterns smaller and denser the thickness of resist has to be reduced. The implication is then that it is unlikely to survive a dry etch. Both of these problems were overcome by the use of a Ti layer on the surface of the ITO. This provided a reflective coating for the control

system to locate the sample surface and also a good mask for the etching of the wires. As before details of the processes for etching the Ti and ITO layer is given in Chapter 4. Fig. 6.9 shows a 519 electrode array after etching of the wires. Shown is a section of the central area with a close up on one of the more densely packed areas.

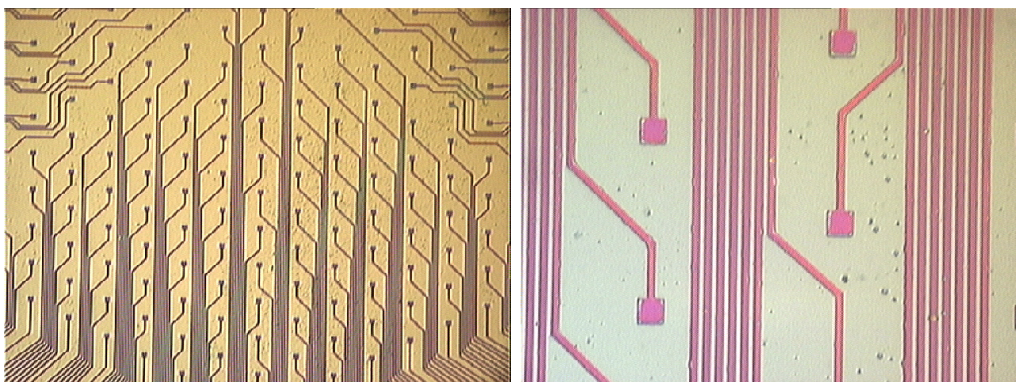


Figure 6.9: Central area of 519 electrode array with the etched wires clearly visible. Also shown is a close up to the densely packed centre of the array.

The design for the central section of the arrays means that some of the wires at the edge of the array pass through large areas of empty space. This can lead to proximity effect problems. The proximity effect as applied to photolithography was discussed in Chapter 2. For electron beam lithography this is caused by the Gaussian shape of the spot and back scattered electrons from the substrate layers. In the case of the etched wires this can result in thinning of the wires and a consequent increase in resistivity of that wire. At its most extreme the proximity effect can lead to wires breaking. Fig 6.10 shows examples of these.

To overcome this problem it is possible to apply a proximity correction to the electron beam job file. This takes into account the beam energy, the

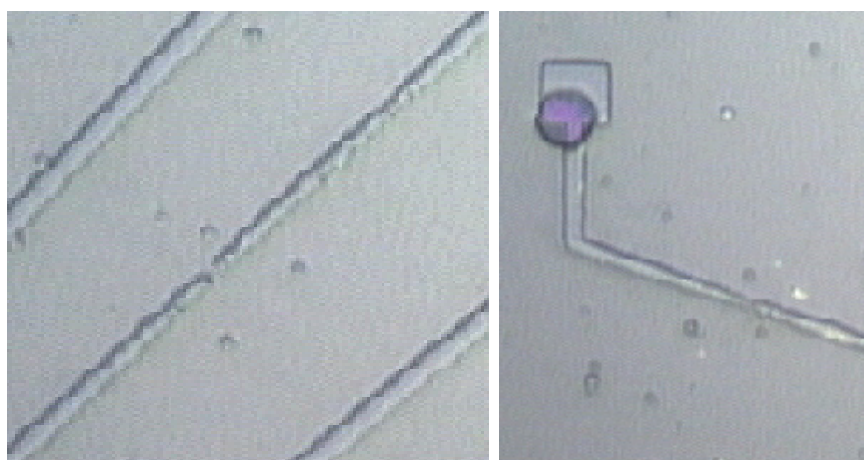


Figure 6.10: Wires which have been overexposed due to the proximity effect. *left* A broken wire. *right* A wire which has been drastically thinned.

thickness of the resist layer and the substrate material of the sample. This modulates the dose by changing the length of time that the spot stays in each location. This ensures that each feature gets the same effective dose. These processes, a two stage etch to pattern the wires followed by a single etch stage to open windows in the  $\text{Si}_3\text{N}_4$  passivation produces half-complete arrays. The next stage before the arrays can be considered ready for testing is to produce electrodes in the windows at the centre of the array.

### 6.3.3 Metallisation of electrodes and contacts

The final stage for the patterned arrays is to have the central electrodes platinised and the bond pads sputtered with aluminium (Al). Platinisation involves electroplating the wire ends with platinum to produce conductive electrodes which can be placed into contact with the excised retinal tissue. The platinisation takes place in a specially designed circuit board which has individual switch controls to each electrode. Completed arrays are connected

to the setup using zebra connectors and a potential of -2V is applied across a 10 M $\Omega$  resistor for 61 electrode arrays.

The zebra connectors are composed of alternating layers of conducting and non-conducting silicon. A pitch of approximately 100  $\mu\text{m}$  ensures good contact with individual electrodes. A solution of 1% platinum chloride, 0.08 % lead acetate and 98.82 % RO water is placed on the electrode area and a platinum wire is used to keep the solution at a positive potential. The voltage is applied for 60 s and the electrodes are kept under observation using a microscope. Platinisation can reduce the resistivity of the electrodes from 100's to 10's of k $\Omega$  depending on the diameter of the electrode [87]. Fig 6.11 shows a platinised electrode array with 60  $\mu\text{m}$  spacing, the distinctive granular structure of the electrode can be seen. This granular structure gives

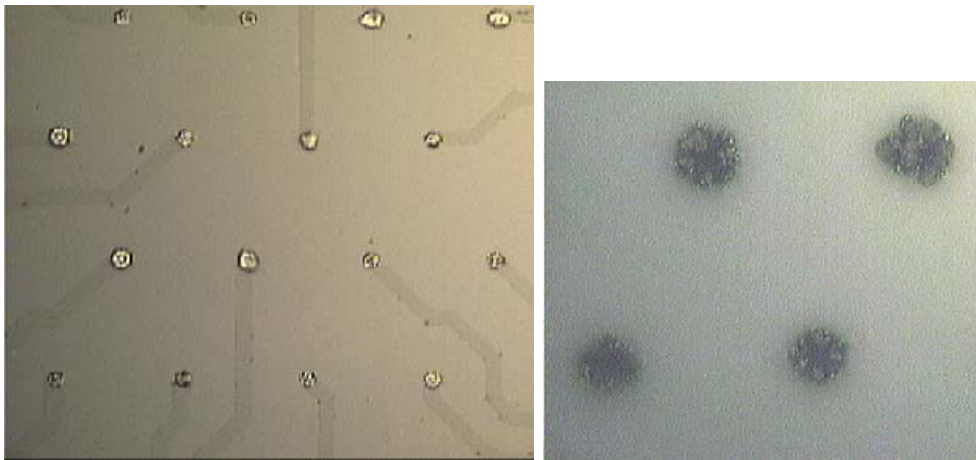


Figure 6.11: Platinised electrodes from an array showing the granular structure of the electrode surface.

a bigger surface area to the electrode and ensures that better contact will be made with the tissue.

The process is similar for platinising the 519 electrode arrays. The main

difference is that here platinisation is done on arrays which have been wire bonded into the readout electronics. A current of  $80\ \mu\text{A}$  per electrode is supplied producing platinum electrodes with the same distinctive granular structure.

As mentioned above the completed 519-electrode arrays are wire-bonded into a test fixture. In order to provide good contact for the bond wires,  $1\ \mu\text{m}$  of Al is sputtered onto the bond pads and patterned using the lift-off technique as discussed in Chapter 2. Sputtering uses an ion beam to physically remove metal from a solid target. By placing the sample in the correct position relative to the target it is possible to have the ejected metal adhere to the sample surface. In this case sputtering is used rather than evaporation for two main reasons. Firstly it is possible to put down significantly thicker layers of metal than with evaporation. The second reason is that sputtered Al adheres better than evaporated material. This ensures that the contact metal does not come off during the life of the array.

### **Complete process description**

The stages involved in the fabrication of micro-electrode arrays have been described above. Fig 6.12 shows the complete process. All of the steps for fabrication of the electrode arrays is included giving some idea of the number of individual processes which go into producing each array.

## **6.4 Details of retinal readout project**

Previously I have discussed the development of the steps necessary to produce an electrode array outlining the differences in process for 61 and 519 electrode arrays. Now I will begin to look at the experimental setup for the retinal

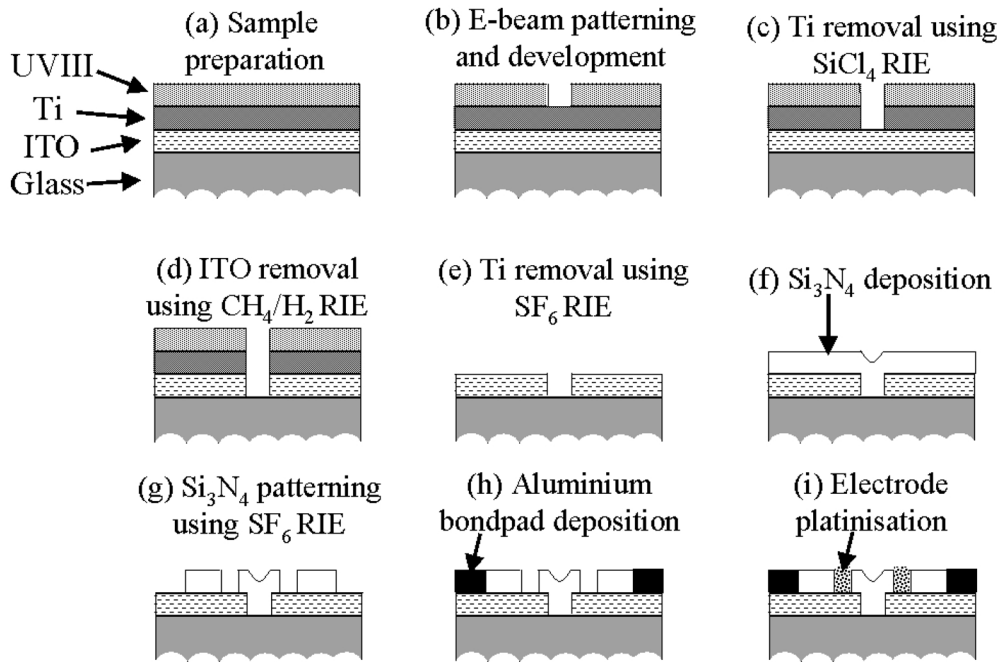


Figure 6.12: Process for production of 519-electrode arrays.

neurophysiology experiments. The description here will briefly outline the setup of the experiments and the type of data taken. This will then go on to show some data taken using arrays fabricated using the processes outlined here.

### 6.4.1 Experimental setup

The completed detectors may be used in biological experiments. The experimental setup is shown in Fig. 6.13. The tissue is maintained in a saline solution at  $37^\circ\text{C}$  to keep the retina alive for up to 8 hours. The ganglion cells make contact with the electrodes of the array. The stimulation comes from above and the whole experiment is imaged from below using a CCD camera coupled to a microscope. The data from the arrays is readout at 20 kHz by analogue electronics. The electronics for this experiment are custom de-

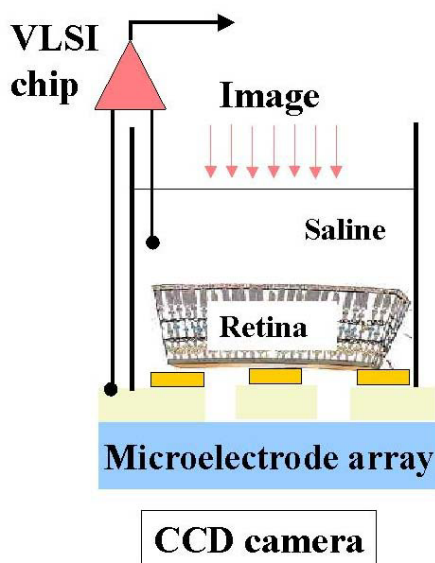


Figure 6.13: Schematics of experimental setup showing the setup for retinal neurophysiology experiments using electrode arrays [87]

signed 64 channel ASIC (application specific integrated circuits) chips known as neurochips. The neurochip was designed at AGH University of Science and Technology in Krakow by the group of Wlodek Dabrowski.

A schematic of the on-chip processing applied to each electrode is shown in Fig. 6.14. Each channel has a differential preamplifier which measures signals relative to the reference signal from the saline solution. Following the amplifier are two band pass filters isolating a range of approximately 50-2000 Hz with a noise typically of  $\leq 5\mu V$  over the passband. The sampling frequency for each channel is 20 kHz with sample and hold (S & H) circuits available on each channel. The signals are then multiplexed at a rate of at least 2.3 MHz. Each chip has 64 channels with a  $100\ \mu m$  pitch between bond pads. For the large scale arrays it is necessary to use several chips running in parallel. The multiplexed signals are stored for later offline analysis. This is essential due to the very large data sets taken during each experiment. The data is analysed for reactions to different types of stimulus. Observa-

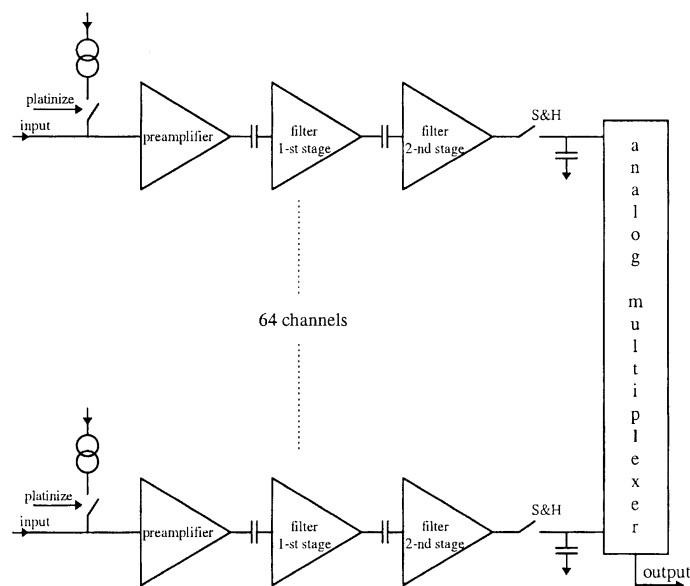


Figure 6.14: Schematics for on chip electronics connected to each electrode in the array [12].

tions of signal interconnects and multiple firings etc. give indications of the processing that is taking place in the tissue.

### 6.4.2 Signal types

The mechanism for the generation of these signals is the release or absorption of potassium and sodium ions ( $K^+$  or  $Na^+$ ). Absorption of ions causes an increase in the net charge in the cell while the release of ions causes the cell to lose charge. The changes are all with reference to a base level called the resting potential. Un-stimulated cells are at the resting potential. The increase in charge is known as hyperpolarisation as the potential of the cell increases above the resting potential. A decrease in charge is called de-polarisation as the release of ions lowers the potential of the cell from the resting potential to near that of the surrounding tissue. The hyperpolarisation/depolarisation is

measured with reference to the saline solution surrounding the tissue when measurements are taken in vitro.

The signal pulses which are produced in the retina for transmission to the brain via the optic nerve are in the form of action potentials. The two main types of signals are the sustained ON or OFF signal and the transient ON-OFF signal. The sustained ON or OFF signal is in the form of a number of electrical pulses with an amplitude of a few hundred  $\mu\text{V}$ . These are repeated quickly for the duration of the illumination. The exact magnitude of the signal is dependent on the intensity of the illumination. A transient signal is produced whenever an edge is detected i.e. one set of receptors is illuminated producing an ON signal and another set adjacent is not illuminated producing an OFF signal. Changes in the illumination state of a given group of receptors will also trigger a transient response. This is in the form of a single pulse of the same magnitude as the sustained pulses and is used to signal the beginning and end of illumination or a change in the position of the illumination. These three signals can provide most of the information needed to produce an image. The colour information for day time vision utilising cones is translated by the combination of red/ green/ and blue receptors which are firing. Again, information about shading etc. comes from the intensity of the responses from the three colour cones. For the present system information about colour is not important.

### **6.4.3 Experimental results**

#### **61 electrode arrays**

As shown a number of 61 electrode arrays have been completed using the techniques outlined here. Some of these completed 61 electrode arrays have

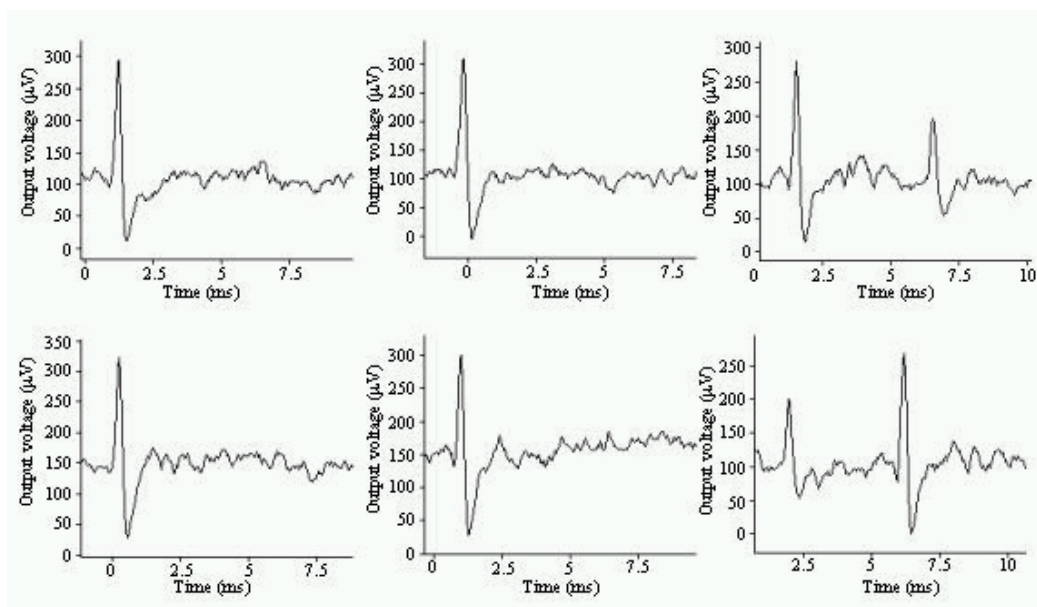


Figure 6.15: Spikes recorded with a 61 electrode array fabricated in Glasgow[88].

been tested and used in experiments. The data recorded from a number of electrodes from one array is shown in Fig. 6.15. The recorded signals show a number of ON signals generated when the receptor is illuminated. The two rightmost spikes are transient signals. The method for generation of these types of signals is shown in Fig. 6.3. The transient signals are generated whenever any of the receptors which that ganglion is connected to changes state. This is the first data taken with arrays fabricated using the dry etching processes which have been discussed earlier in the thesis, Chapter 4. The data taken from this array was as good as that which had been taken previously using arrays fabricate using a wet etching process. This means that the fabrication processes developed are suitable for producing microelectrode arrays for these types of studies.

### 519 electrode arrays

The process to produce the 519 electrode arrays has been discussed and the completed arrays shown. However, because of the change in the experimental setup it was necessary to test the array for faults. For the 519 electrode arrays the platinisation is carried out after the array has been wire bonded in to the experimental setup. Also once it has been inserted it is not possible to remove the array. For this reason only arrays with  $< 5\%$  dead channels are suitable to be considered for experimentation.

The first test for the arrays is a visual inspection. This should discover any broken wires, as shown in Fig. 6.10. In the case of this first array there was only one definite break. However there were several wires which were thinned. The second test is an electrical short test. This measures the resistance between pairs of wires. If the space between the wires has been completely etched over its whole length the resistance will be returned as the maximum value possible for the test setup, in this case  $100\text{ M}\Omega$ . A short between wires i.e. where the ITO etch has been incomplete will have a resistance in the 10's of  $\text{k}\Omega$  range.

The test was carried out using a Keithley 2300 LCR meter under control of Labview software connected to a manual probe station. The software was written to allow measurement of 5 pairs of wires at one time with the data output numbered according to the first electrode in the pair. Fig. 6.16 shows the complete short test measurements for the completed 519-electrode array. This array has 7 pairs of shorted channels, as shown by the low inter-wire resistance. This reduces the number of usable channels from 519 to approximately 510 counting shorts and broken wires. This is an acceptable

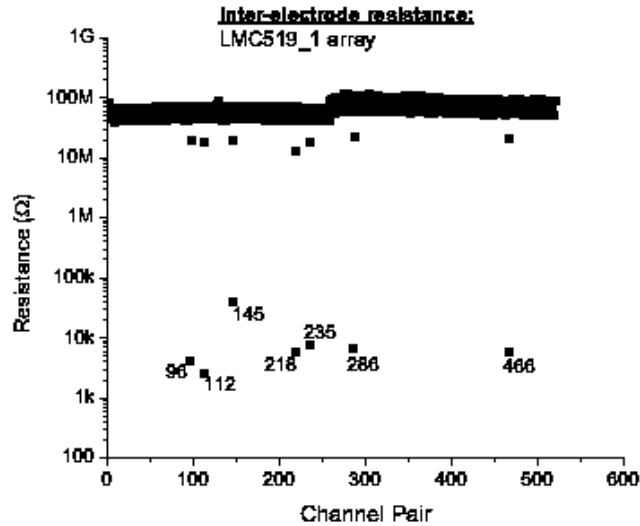


Figure 6.16: Short test measurements for completed 519 electrode array. Shorted channels are numbered.

number, less than 5 % dead channels, to be connected to the test apparatus.

## 6.5 Future work and further developments

519-electrode arrays have been fabricated using the plasma etch/ deposition/ surface treatment processes developed. As yet the completed arrays have not been used experimentally. However, the techniques which have been developed for use in fabricating 61 and 519 electrode arrays can be used to begin to develop the next generation of denser, larger arrays. The dry etching processes are very anisotropic which ensures that the feature sizes are scaleable. Currently the detectors are used to look study MT neurons which are spaced at  $\sim 60 \mu\text{m}$ . However, the current studies indicate that smaller electrode spacing may be desirable to further study these and other

cells. This will provide a new set of challenges in the array fabrication process

The development of arrays with reduced spacing has begun. Initial test runs of 519-electrode arrays with an electrode pitch of 30  $\mu\text{m}$  rather than 60  $\mu\text{m}$  have been carried out. These will observe what problems, if any, arise from reduction in electrode spacing and the subsequent reduction in line width for the connecting wires.

Other planned developments in the array designs are an increase of the number of electrodes to  $\sim 2000$  and then to reduce the electrode spacing further. The electrodes will be of a similar size to those already in production but obviously the challenges inherent in connecting to such a large number will cause problems in the array fabrication. Reducing the electrode spacing for such a large array will add another level of complexity to the fabrication process. The wire sizes will have to be reduced still further with all of the problems that brings i.e. increased resistivity, noise, cross talk. These are all problems which will have to be overcome in the future to develop new experiments to further understand the nature of the retina and the signals that it produces.

# Chapter 7

## Conclusions

Within this work I have investigated a range of plasma processes and discussed two applications of detector manufacture. The two specific cases for using the dry etch and plasma deposition processes are part of ongoing work. They have shown promising results to date but need further work and development as the nature of the projects evolves. The work described here has produced useful, reproducible etch processes and quantified the effect on the material of the irradiation during etching. One of the next steps will be to refine these techniques for application to a range of processes as designs and requirements change.

ICP etching of SiC has been shown to be several times faster than a standard RIE etch. However, the damage induced in the material is not as great, due to the faster removal of the damaged surface layers. This means that by modifying the process described here it will be possible to either increase the etch rate for very deep etching, e.g. through wafer etching, or for low damage etching. These are possible by a variety of methods. Variations in the RF power applied to the ICP discharge and the platen can increase or reduce the etch rate, as shown in Chapter 4. Changes in the etch rate

by other means can also modify the damage induced e.g. varying the O<sub>2</sub> concentration. Further experimentation with changing the ratio of O<sub>2</sub> and the applied powers will enable the designing of application specific processes.

The specific application investigated here for using the plasma processes on SiC were for application as a radiation detector material. Detectors were fabricated on semi-insulating 4H-SiC using processes outlined in Chapter 4 and were tested for their suitability as radiation detectors using Am<sup>241</sup>  $\alpha$  particles, as shown in Chapter 5. The detectors produced pulse height spectra which were calculated to be approximately 60 % of the total charge available. Simulation work has shown that this is the maximum charge collection efficiency (CCE) possible from material of this type with a high concentration of vanadium dopant. Irradiation of a number of devices has shown that the CCE drops and then recovers with increasing fluence of 300 MeV/c pions. A fluence of  $10^{13}$  cm<sup>-2</sup> shows a CCE reduced by 10 % compared to the unirradiated sample. It gives an indication that SiC may be a suitable material for production of detectors for high radiation areas such as those expected in the LHC being implemented at CERN.

Future work in this area would concentrate on producing and testing detectors fabricated on non-vanadium doped S.I. material, which may produce a higher CCE. Complete, 100 %, CCE detectors would then be tested for performance with a range of radiation sources both before and after irradiation. This is to observe the efficiency of the detector for other more difficult to detect radiation i.e. minimum ionising particles (MIPS) and low energy x-rays both of which produce significantly smaller charge pulses.

The processes outlined in Chapter 4 for production of micro-electrode arrays for retinal neurophysiology experiments as part of the Retinal Read-

out Project have been shown to be capable of producing complete arrays suitable for the test apparatus available. 61 electrode arrays based on an existing design have been shown to perform as well as any produced using older fabrication technology. However, the dry etch processes which have been developed are suitable for production of significantly denser arrays with a much smaller feature size and spacing.

Initial tests to produce a 519 electrode array which has a critical dimension of  $\sim 1.5 \mu\text{m}$  have given a number of unforeseen problems. These have been overcome with a reasonable degree of success and complete arrays have been fabricated and undergone provisional testing before being used for experiments with tissue samples. A small number of channels, roughly 10 from 519, have been observed to be non-functional for two main reasons. The first reason is an inter-channel short, caused by two adjacent channels which are not completely etched out. Reasons for incomplete etching are generally related to sample cleanliness. A single grain of dust can short a number of channels. Dust on the sample surface before any of the processes can cause a short when the etching is carried out. The effect of the short is to effectively turn two channels into one as the resistivity between them means that signals from one would be read on the other. Each of these shorts kills one channel in the pair.

The other problem which has resulted in non-working electrodes is a break in the wire. The breaks are caused by the proximity effect. The proximity effect is related to the way that an electron beam lithography system writes a pattern. The initial spot of electrons is reflected from subsequent layers of the sample after passing through the resist. These reflected electrons can cause isolated features to become partially exposed. Partial exposure can cause

narrowing of lines which is particularly problematic for narrower features and where features are surrounded by a large area that has been written. It is possible to correct for the proximity effect and this is being applied for future iterations of the production process. The proximity effect accounted for another 2-3 dead channels.

Once the 519 electrode array process has been finalised with the proximity correction in place a number of arrays will be produced for experimentation. However, the completion of the process and testing the arrays is only one stage. The development of denser arrays is ongoing. The processes developed here are suitable for production of features which are smaller than the existing 1.5  $\mu\text{m}$  critical dimension. This will allow the production of denser arrays with many more electrodes. For example design work is underway on a 2000 electrode array. An array so dense will produce its own unique problems which will have to be overcome as they are encountered.

In this work I have attempted to show the use of several different plasma processes, etch and deposition, in the production of semiconductor detectors for different applications. The versatility of the processes means that there are a number of other possible applications to which it is possible to apply them. The limiting factor is time for experimentation into other specific uses instead of producing a general process which can be used for many different fabrication projects.

# Bibliography

- [1] B. J. Baliga, Power Semiconductor Devices for Variable-Frequency Drives, Proceedings of the IEEE, 82, (1994), 1112
- [2] B. J. Baliga,, Power ICs In The Saddle, IEEE Spectrum, 32, (1995),34
- [3] B. J. Baliga, IEEE Transactions on Electron Devices, 43, (1996), 1717
- [4] G. T. Heydt, B. J. Skromme, Materials Research Society Symposia Proceedings, 483, Materials Research Society, Warrandale, PA, (1998), 3.
- [5] R. J. Trew, J.-B. Yan, P. M. Mock, Proceedings of the IEEE, 79, (1991), 598
- [6] C. E. Weitzel, J. W. Palmour, C. H. Carter Jr., K. Moore, K. J. Nordquist, S. Allen, C. Thero, M. Bhatnagar, IEEE Transactions on Electron Devices, 43, (1996), 1732.
- [7] C. E. Weitzel, K. E. Moore, Materials Research Society Symposia Proceedings, 483, Materials Research Society, Warrandale, PA, (1998), 111.

- [8] M. Bhatnagar, B. J. Baliga, IEEE Transactions on Electron Devices, 40, (1993), 645.
- [9] G. Bellini, M. Di Corato, P. F. Manfredi and G. Vegni, Nuclear Instruments and Methods, 107, (1973), 85
- [10] J. Kemmer, Nuclear Instruments and Methods, 169, (1980), 499
- [11] A. Litke, M. Meister. Nucl. Instr. and Meth. A, 310, (1991), 389
- [12] A. M. Litke, Nucl. Inst. and Meth. A, 418, (1998), 203
- [13] A. M. Litke, Nucl. Inst. and Meth. A, 435, (1999), 242
- [14] S.M. Sze, 'Semiconductor Devices, Physics and Technology', Wiley, New York, 1985
- [15] S.A. Campbell, 'The science and technology of microelectronic fabrication', Oxford University Press, New York, 2001
- [16] Course notes for 'Micro- and nano-electronics fabrication' by Prof. C. D. W. Wilkinson, Dept. of Electrical and Electronic Engineering, University of Glasgow, 2000
- [17] L . Tonks, I. Langmuir, Phys. Rev., **33**, (1929), 195
- [18] D. F. Richards, M. O. Bloomfield, S. Soukane, T. S. Cale, Vacuum, 59, (2000) 168
- [19] K. Nishikawa ,H. Ootera, S. Tomohisa, T. Oomori, Thin Solid Films, 374 (2000) 190
- [20] B. R. Rogers, T. S. Cale, Vacuum, 65, (2002), 267

- [21] J. Hopwood, *Plasma sources Sci. Technol.*, 1, (1992) 109
- [22] 'Industrial plasma engineering vol. 1: Principles', J. Reece Roth, IOP Publishing, Bristol, 1995
- [23] 'Industrial plasma engineering vol. 2: Applications to nonthermal plasma processing', J. Reece Roth, IOP Publishing, Bristol, 2001
- [24] F. W. Aston, *Proc. R. Soc. London, A* **84**, (1911), 526
- [25] N. Camara, K. Zekentes, *Solid-State Electronics*, 46, (2002), 1959
- [26] P. H. Yih, V. Saxena, A. J. Steckl, *phys. stat. sol. (b)*, 202, (1997), 605
- [27] P. Leerungnawarat, K. P. Lee, S. J. Pearton, F. Ren, S. N. G. Chu, *J. Electron. Mater.*, 30, (2001), 202
- [28] F. A. Khan, I. Adesida, *Appl. Phys. Lett.*, 75, (1999) 2268
- [29] P. Chabert, N. Proust, J. Perrin, R. W. Boswell, *Appl. Phys. Lett.*, 76, (2000), 2310
- [30] F. A. Khan, B. Roof, L. Zhou, I. Adesida, *J. Electron. Mater.*, 30, (2001), 212
- [31] V. Khemka, T. P. Chow, R. J. Gutmann, *J. Electron. Mater.*, 30, (2001), 1128
- [32] E. Danielsson, S.-K. Lee, C.-M. Zetterling, M. Ostling, *J. Electron. Mater.*, 30, (2001), 247

- [33] H. Cho, P. Leerungnawarat, D. C. Hays, S. J. Pearton, S. N. G. Chu, R. M. Strong, C.-M. Zetterling, M. Ostling, F. Ren, Appl. Phys. Lett., 76, (2000), 739
- [34] D. J. Morrison, A. J. Pidduck, V. Moore, P. J. Wilding, K. P. Hilton, M. J. Uren, C. M. Johnson, N. G. Wright, A. G. O'Neill, Semicond. Sci. Technol., 15, (2000), 1107
- [35] Physics of semiconductor devices, 2<sup>nd</sup> edition', S. M. Sze, John Wiley and sons, New York, 1981
- [36] 'Metal-semiconductor contacts, 2<sup>nd</sup> edition', E. H. Rhoderick, E.H. Williams, Oxford University Press, Oxford, 1988
- [37] Z.C.V.R.V. Kumar, A. Mansingh, J. Appl. Phys., 65, (1989), 1270.
- [38] S. Ishibashi, Y. Higuchi, Y. Ota, K. Nakamura, J. Vac. Sci. Technol. A ,8, (1990), 1399.
- [39] A.H. Shih, A. Demos, R.D. Beer, Solid State Technol., 39, (1996), 71
- [40] "Study of Indium Tin Oxide (ITO) for Novel Optoelectronic Devices" Ph.D. thesis by Shabbir A Bashar (1998)
- [41] J. Y. Park, H. S. Kim, D. H. Lee, K. H. Kwon, G. Y. Yeom, Surface and Coatings Technology, 131, (2000), 247
- [42] Y. Kuo, Vacuum, 51, (1998), 777
- [43] Y. J. Lee, J. W. Bae, H. R. Han, J. S. Kim, G. Y. Yeom, Thin Solid Films, 383, (2001), 281

- [44] I. Adesida, D. G. Balleger, J. W. Seo, A. Ketterson, H. Chang, K. Y. Cheng, T. Gessert, *J. Vac. Sci. Technol. B*, **9**, (1991), 3551
- [45] L. J. van der Pauw, *Philips Res. Repts.* **13**, (1958), 1.
- [46] 'Radiation detection and measurement 3rd edition', G. F. Knoll, John Wiley and sons, New York, 2000
- [47] M. S. Livingston, H. A. Bethe, *Rev. Mod. Phys.* **9**, (1937), 245
- [48] J.F. Zeigler, J.P. Biersack, IBM-Research, Yorktown Heights, New York, USA, 1996.
- [49] M. Rogalla, K. Runge, A. Söldner-Rembold, *Nucl. Phys. B (Proc. Suppl.)* **78**, (1999), 516
- [50] E. J. Connolly, G.M. O'Halloran, H. T. M. Pham, P.M. Sarro, P. J. French, *Sens. Actuators A* **99**, (2002), 25
- [51] K. Rnatjan, A. Bhardwaj, Namrata, S. Chatterji, A. K. Srivastava, R. K. Shivpuri, *Nucl. Instr. and Meth. A* **495**, (2000), 191
- [52] P. G. Neudeck, W. Huang, M. Dudley, *IEEE Trans. Electron Devices* **46** **3**, (1999), 478
- [53] P. G. Neudeck, J. A. Powell, *IEEE Electron Device Lett.* **15** (2), (1994), 63
- [54] W. C. Mitchell, R. Perrin, J. Goldstein, M. Roth, M. Ahoujja, S. R. Smith, A. O. Evwaraye, J. S. Solomon, G. Landis, J. Jenny, H. M<sup>c</sup>D. Hobgood, G. Augustine, V. Balakrishna, *Mat'ls. Sci. Forum* **264-268**, (1998), 545

- [55] F Bechstedt, A Fissel, J Furthmüller, U Grossner and A Zywiets,  
J. Phys.: Condens. Matter **13**, (2001), 9027
- [56] I. Pitilie, L. Pintilie, K. Irmischer, B. Thomas, Appl. Phys. Lett.  
**81**, (2002), 4841
- [57] S.A. Reshanov, V.P. Rastegaev, Diam. Relat. Mater. **10**, (2001),  
2035
- [58] K. M. Smith, Nucl. Inst. and Meth. A 368, (1995), 220
- [59] L. Beattie, T. J. Brodbeck, A. Chilingarov, G. Hughes, P. Ratoff,  
T. Sloan, Nucl. Inst. and Meth. A, 412, (1998),238
- [60] T. Quinn, R Bates, M, Bruzzi, W. Cunningham, K. Mathieson,  
M. Moll, T. Nelson, H. E. Nilsson, I. Pinitllie, L. Reynolds, S.  
Sciortino, P. Sellin, H. Strachan, B. G. Svensson, J. Vaitkus, M.  
Rahman, to be presented at IEEE (2003)
- [61] F. Nava, P.Vanni, G. Verzelezi, A. Cavallini, L.Polenta, R. Nipoti,  
C. Donolato, Mat'ls. Sci. Forum **353-356**, (2001), 757
- [62] M. Bruzzi, F. Nava, S. Russo, S. Sciortino, P. Vanni, Diam. Relat.  
Mater. **10**, (2001), 657
- [63] C. Manfreodotti, F. Fizzotti, A. Lo Giudice, C. Paolini, E. Vittone,  
F. Nava, Appl. Surf. Sci. 184, (2001), 448
- [64] G. Verzelezi, P. Vanni, F. Nava, C. Canali, Nucl. Inst. and Meth.  
A 476, (2002), 717

- [65] F. Nava, E. Vittone, P. Vanni, G. Verzellezi, P. G. Fuochi, C. Lanzieri, M. Glaser, Nucl. Inst. and Meth. A 505, (2003), 645
- [66] F. Ruddy, A. R. Dulloo, J. H. Seidel, J. W. Palmour, R. Singh, Nucl. Inst. and Meth. A 505, (2003), 159
- [67] M. Sandison, A.S.G. Curtis and C.D.W. Wilkinson. J. Neurosci. Methods 114 (2002), p. 63.
- [68] M. Jenkner and P. Fromherz. Phys. Rev. Lett. 71 (1993), 4079.
- [69] M. Meister, R. O. L. Wong, D. A. Baylor, C. J. Shatz, Science, 252, (1991), 939
- [70] M. Meister, L. Lagnado, D. A. Baylor, Science, 270, (1995), 1207
- [71] M. J. Berry, D. K. Warland, M. Meister, Proc. Natl. Acad. Sci. USA, 94, (1997), 5411
- [72] S. Nirenberg, M. Meister, Neuron, 16, (1997), 637
- [73] M. J. Berry, M. Meister, J. Neurosci., 18, (1998), 2200
- [74] M. R. DeWeese, M. Meister, Network: Comput. Neural Syst, (1999), 325
- [75] T. E. Holy, C. Dulac, M. Meister, Science, 289, (2000), 1569
- [76] J. Keat, P. Reinagel, R. C. Reid, M. Meister, Neuron, 30, (2001), 803
- [77] D. Chander, E. J. Chichilnisky, J. Neursci., 21, (2001), 9904
- [78] E. J. Chichilnisky, R. S. Kalmar, J. Neursci., 22, (2002), 2737

- [79] T. W. Berger, M. Baudry, R. D. Brinton, J.-S. Liaw, V. Z. Marmarelis, A. Y. Park, B. J. Sheu, A. R. Tanguay, *Proc. IEEE*, 89, (2001), 993-1012
- [80] W. Liu, K. Vichienchom, M. Clements, S. C. DeMarco, C. Hughes, E. McGucken, M. S. Humayun, E. de Juan, J. D. Weiland, R. Greenburg, *IEEE J. Solid-State Circuits*, 35, (2000), 1487
- [81] W. Liu, E. McGucken, M. Clements, C. DeMarco, K. Vichienchom, C. Hughes, M. Humayun, J. Weiland, R. Greenburg, E. de Juan,
- [82] A. Hung, D. Zhou, R. Greenberg, J. W. Judy,
- [83] E. Zrenner, A. Stett, S. Wiess, R. B. Aramant, E. Guenther, K. Kohler, K.-D. Miliczek, M. J. Seiler, H. Haemmerle, *Vision Research*, 39, (1999). 2555
- [84] E. Margalit, M. Maia, J. D. Weiland, R. J. Greenburg, G. Y. Fujii, G. Torres, D. V. Piyathaisere, T. M. O'Hearn, W. Liu, G. Lazzi, G. Dagnelie, D. A. Scribner, E. de Juan, M. S. Humayun, *Surv. Ophthalmol.*, 47, (2002), 335
- [85] J. E. Dowling, 'The Retina, An approachable part of the brain', Bellknap, Cambridge M.A., 1987
- [86] W. Cunningham, K. Mathieson, M. Horn, J. Melone, F.A. McEwan, A. Blue, V. O'Shea, K.M. Smith, A. Litke, E. J. Chichilnisky, M. Rahman, *Nucl. Inst. and Meths. A*, 509, (2003), 235-239

- [87] K. Mathieson, W. Cunningham, J. Marchal, J. Melone, M. Horn, V. O'Shea, K. M. Smith, A. Litke, E. J. Chichilnisky and M. Rahman, *Microelectron. Eng.*, 67-68, (2003), 520
  
- [88] K. Mathieson, W. Cunningham, J. Marchal, J. Melone, M. Horn, D. Gunning, R. Tang, C. Wilkinson, V. O'Shea, K. M. Smith, A. Litke, E. J. Chichilnisky and M. Rahman, *Nucl. Inst. and Meths. A*, Uncorrected Proof available online (2003).